Electronic Theses and Dissertations   Fogler Library

2010

Multiscale Investigation of Random Heterogenous Media in Materials and Earth Sciences

Andrew J. Goupee

Follow this and additional works at: http://digitalcommons.library.umaine.edu/etd

Part of the Mechanical Engineering Commons

MULTISCALE INVESTIGATION OF RANDOM HETEROGENEOUS MEDIA IN MATERIALS AND EARTH SCIENCES

By

Andrew J. Goupee

B.S. University of Maine, 2003

M.S. University of Maine, 2005

A DISSERTATION

Submitted in Partial Fulfillment of the

Requirements for the Degree of

Doctor of Philosophy

(in Mechanical Engineering)

The Graduate School

The University of Maine

May, 2010

Advisory Committee:

    Senthil S. Vel, Ph.D., Associate Professor of Mechanical Engineering, Advisor

    Zhihe Jin, Ph.D., Assistant Professor of Mechanical Engineering

    Alireza S. Sarvestani, Ph.D., Assistant Professor of Mechanical Engineering

    Scott E. Johnson, Ph.D., Professor of Tectonics and Structural Geology

    Paul R. Heyliger, Ph.D., Professor of Structural Engineering and Solid Mechanics,

        Colorado State University

LIBRARY RIGHTS STATEMENT

MULTISCALE INVESTIGATION OF RANDOM HETEROGENEOUS MEDIA IN MATERIALS AND EARTH SCIENCES

By Andrew J. Goupee

Dissertation Advisor: Dr. Senthil S. Vel

An Abstract of the Dissertation Presented
in Partial Fulfillment of the Requirements for the
Degree of Doctor of Philosophy
(in Mechanical Engineering)
May, 2010

This dissertation is concerned with three major areas pertaining to the characterization and analysis of heterogeneous materials. The first is focused on the modeling of heterogeneous materials with random microstructure and understanding their thermomechanical properties as well as developing a methodology for the multiscale thermoelastic analysis of random heterogeneous materials. Realistic random microstructures are generated for computational analyses using random morphology description functions. The simulated microstructures closely resemble actual micrographs of random heterogeneous materials. The simulated random microstructures are characterized using statistical techniques and their homogenized material properties computed using the asymptotic expansion homogenization method. The failure response of random media is investigated via a direct micromechanical failure analysis which utilizes stresses at the microstructural level coupled with appropriate phase material failure models to generate initial failure envelopes. The homogenized material properties and failure envelopes are employed to perform accurate coupled macroscale and microscale analyses of random heterogeneous material components.

The second area addressed in this dissertation involves the transient multiscale analysis of two-phase functionally graded materials within the framework of linearized thermoelasticity. The two-phase material microstructures, which are created using a morphology description function, have smoothly varying microstructure morphologies that depend on the volume fractions of the constituent phases. The multiscale problem is analyzed using asymptotic expansion homogenization coupled with the finite element method. Model problems are studied to illustrate the versatility of the multiscale analysis procedure which incorporates a direct micromechanical failure analysis to accurately compute the factors of safety for functionally graded components.

The last area of this dissertation is concerned with determining the role of heterogeneous rock fabric features in quartz/muscovite rich rocks on seismic wave speed anisotropy. The bulk elastic properties and corresponding wave velocities are calculated for synthetic heterogeneous rock microstructures with varying material and geometric features to investigate their influence on seismic wave speed anisotropy. The asymptotic expansion homogenization method is employed to calculate precise bulk stiffness tensors for representative rock volumes and the wave speed velocities are obtained from the Christoffel equation. The obtained results are also used to assess the performance of analytic homogenization schemes currently used in the geophysics community.

DISSERTATION

ACCEPTANCE STATEMENT

On behalf of the Graduate Committee for _____,
I affirm that this manuscript is the final accepted dissertation. Signatures of all
commitee members are on file with the Graduate School at the University of Maine,
5755 Stodder Hall, Orono, Maine 04469.

DEDICATION

For my wife Kate...

ACKNOWLEDGEMENTS

TABLE OF CONTENTS

LIST OF TABLES

LIST OF FIGURES

CHAPTER 1

INTRODUCTION

A overview of the relevant scientific literature pertaining to the areas of interest in this dissertation is presented in this first chapter. These areas, each involving the study of heterogeneous materials, include random heterogeneous materials, functionally graded materials and seismic wave speed anisotropy. After the background and literature review is concluded, an overview of the dissertation is presented including research objectives, research contributions and an outline of the dissertation layout.

1.1 Background and Literature Review

1.1.1 Random Heterogeneous Materials

It is important to understand the response of random heterogeneous materials since they are widely encountered in engineering applications. Much progress has been made in recent years in characterizing the properties of random heterogeneous materials (Torquato, 2002). Prior work on this subject can be broadly classified into three categories, namely effective medium theories, theoretical bounding methods and computational simulations. The effective medium theories include the Mori-Tanaka method, self-consistent scheme and other mean-field models (Mori and Tanaka, 1973; Benveniste, 1987; Hill, 1965). The theoretical bounding methods consist of the Hashin-Shtrikman lower and upper bounds as well as other higher-order bounds (Hashin and Rosen, 1964; Hill, 1964; Hashin, 1965; Rosen and Hashin, 1970; Hashin, 1979). Computational models typically utilize finite element or boundary element methods to investigate the response of a representative volume element of the heterogeneous material. The present work, which belongs to the later class of methods, utilizes asymptotic expansion homogenization (AEH) in conjunction with the finite element method to determine the homogenized material properties of random heterogeneous materials

(Bensoussan *et al.*, 1978; Sanchez-Palencia, 1981/1983; Guedes and Kikuchi, 1990; Terada *et al.*, 2000).

Computational analyses of random heterogenous materials rely on simulated random microstructures or digital images of actual microstructures (Langer *et al.*, 2001). Several researchers have investigated the response of random heterogeneous materials (*e.g.* see (Terada *et al.*, 2000; van der Sluis *et al.*, 2000)). A majority of the studies consider particles of regular geometric shape and size, often spheres, cylinders or ellipses that are randomly distributed in a matrix phase. Torquato and Stell characterized the statistical properties of microstructures consisting of ensembles of impenetrable (Torquato and Stell, 1982) and penetrable (Torquato and Stell, 1983) spheres using the n-point probability functions. Segurado and Llorca (2002) analyzed the elastic properties of materials comprised of a matrix embedded with non-overlapping spheres. Gusev *et al.* (2000) employed a Monte Carlo procedure to generate periodic models of transversely random fiber packed composites and subsequently analyzed there elastic response and compared the result with experimental values. Grujicic and Zhang (1998) studied slightly more complex geometries with the Voronoi cell finite element method including randomly sized and oriented elliptical inclusions embedded in a matrix and also a material comprised of intertwined clusters of irregular polygons. Leggoe *et al.* (1998) analyzed the deformation of random metal matrix composites using two- and three-dimensional regular grids of finite elements. Cho and Ha (2001) and Mishnaevsky (2005) each analyzed graded microstructures using regular grids of rectangular and voxel shaped finite elements, respectively. Using these regular grid morphologies the gross features of a microstructure can be captured quite well, however the finer microstructure details are not represented accurately. While the microstructures studied provide useful results for certain types of composite materials, micrographs of heterogeneous materials fabricated through manufacturing processes such as plasma spraying and powder metallurgy reveal that

the particles usually have random shapes and sizes (*e.g.* see (Kawasaki and Watanabe, 1997; Takagi *et al.*, 2003; Jin *et al.*, 2005)). In addition, the morphology of the microstructure usually depends on the volume fractions of the constituent material phases. For certain volume fractions, the random heterogeneous material may not have clearly defined matrix and particulate phases. Instead, the two phases may form a completely interconnected network. Such materials, which are commonly referred to as interpenetrating phase composites (IPCs), have important technological applications (Leßle *et al.*, 1999; Wegner and Gibson, 2000/2001; Aldrich and Fan, 2001; Feng *et al.*, 2004).

A means of synthetically creating realistic microstructures that mimic the aforementioned trends is to employ a technique which defines the interface of the two material phases via a level cut of a random field (Cahn, 1965). Roberts and Teubner (1995) used Gaussian random fields to create and characterize the transport properties of random microstructures. Subsequently, Roberts and Knackstedt (1996) investigated the conductivity, diffusivity and elastic moduli of Gaussian random field microstructures through rigorous bounding techniques. To date, however, the thermoelastic material properties and failure under thermomechanical loads of random heterogeneous materials of the type used in (Roberts and Teubner, 1995; Roberts and Knackstedt, 1996) has not been investigated.

1.1.2 Functionally Graded Materials

In order to create the increasingly more complex components and systems that society demands, engineers and designers require ever improving advanced materials. In an effort to meet the ever increasing demands placed on advanced materials, a class of composite materials known as functionally graded materials (FGMs) (Miyamoto *et al.*, 1999) have been proposed for certain applications. FGMs are advanced heterogeneous materials that possess continuously varying material properties which are

tailored to maximize component performance. The smooth variation in material properties is achieved by carefully altering the volume fraction and microstructural morphology of the constituent materials, which are chosen based on functional performance requirements, from point to point within the body. The smooth variation in material properties eliminates the presence of interfaces between discrete materials often found in typical laminate composites which alleviates plastic deformation and cracking, especially in high temperature applications (Finot and Suresh, 1996).

In recent years, much research has been performed on the analysis and optimization of FGMs. Analytic solutions have been presented for a large array of geometries, loadings, material combinations and grading architectures (Loy *et al.*, 1999; Cheng and Batra, 2000; Ueda and Gasik, 2000; Vel and Batra, 2002/2003; Elishakoff and Guédé, 2004). These and several prior studies of functionally graded components have clearly demonstrated the advantages of functionally graded materials over typical discretely laminated composite structures, such as, reduced peak stresses within the component under thermal and mechanical loads. Other studies have focused on optimizing the volume fraction distribution of the heterogeneous material in one or more dimensions in an effort to maximize the performance of the functionally graded component under prescribed loading conditions (Cho and Ha, 2002; Lipton, 2002; Qian and Ching, 2004, Goupee and Vel, 2006/2007; Vel and Pelletier, 2007). Most of the aforementioned analytical, numerical and optimization studies utilize simple mean-field homogenization techniques to determine the effective material properties of the heterogeneous material as a function of volume fraction. Examples of such homogenization methods include the rule of mixtures (Voigt, 1889), modified rule of mixtures (Tamura *et al.*, 1973), Mori-Tanaka method (Mori and Tanaka, 1973; Benveniste, 1987) and self-consistent scheme (Hill, 1965). While these types of homogenization schemes allow the determination of the effective properties of the composite with knowledge of just the volume fraction and respective constituent properties, they are unable to account

for variations in microstructural morphology which can greatly influence the homogenized material properties even at a fixed volume fraction. To ensure an accurate solution or optimization routine, specific information regarding the microstructure morphology cannot be neglected during the homogenization process. An effective means of performing this task is by utilizing the AEH method.

The AEH method provides a number of advantages over conventional homogenization techniques usually employed in FGM analysis. The AEH method introduces two length scales in the analysis procedure, one associated with the macroscopic functionally graded part and the other associated with heterogeneous material microstructure, *i.e.* a macroscale and a microscale. By introducing two length scales, one can effectively analyze sophisticated functionally graded components with complex microstructures, usually with the aid of numerical solution techniques like the finite element method. The multiscale approach also allows the computation of the stress state at the microscale, a process which cannot be performed using the effective medium homogenization methods mentioned previously. With knowledge of the microstresses, one can apply material phase specific failure criteria to better assess failure of the heterogeneous material of which the functionally graded component is comprised. In this work, this process is termed direct micromechanical failure analysis. Prior FGM works, like those of Cho and Choi (2004) and Goupee and Vel (2007), have at best attempted to incorporate the failure estimate of FGM materials via simplified analytic estimates such as the linear rule of mixtures (Bishop and Hill, 1951) or the Hashin-Shtrikman lower estimate (Casteñeda and deBotton, 1992). These methods, which only work for FGMs comprised of two ductile phases, do not account for microstructural morphology when homogenizing the strength of the resulting FGM material. And since microstructure features greatly influence FGM material failure, as will be demonstrated in the results of this work, a more sophisticated and robust methodology like direct micromechanical failure analysis is required.

While the AEH method has been applied very sparingly in FGM research, there have been several studies that make use of the AEH method to analyze heterogeneous material components. For example, Fish and Wagiman (1992) and Ghosh *et al.* (1995) each analyzed a boron/aluminum heterogeneous plate with a centrally located hole under in-plane tensile forces using two distinct microstructure morphologies. Fish and Wagiman generated the necessary field approximations with finite elements while Ghosh *et al.* used a coupled finite element/Voronoi cell finite element method. Ghosh *et al.* (1996) developed a multiscale Voronoi cell finite element model for the elastic-plastic analysis of porous and composite materials. Takano *et al.* (2000) presented a multiscale computational method for the stress analysis of composite material structures at both the macroscopic and microscopic length scales. Terada and Kikuchi (2001) developed a class of algorithms for the multiscale analyses of heterogeneous media and demonstrated their approach on two multiscale problems, a hydrostatically loaded dam and a beam in flexure. Only recently have multiscale methods been utilized for functionally graded materials where the volume fraction and microstructure morphology change from point to point within the macroscopic body. Yin *et al.* (2005) created a multiscale framework for analyzing the elastic deformation of functionally graded composites. Analyzing bamboo as a functionally graded material, Silva *et al.* (2006) used a multiscale approach to model sections of bamboo under various loading conditions.

1.1.3 Seismic Wave Speed Anisotropy

Most individual components that comprise Earth materials possess some level of material anisotropy, and when they are structured in orderly patterns termed rock fabrics, the resulting bulk rock can exhibit a wide range of possible effective anisotropic elastic stiffnesses. In many cases, the elastic anisotropy of rock fabrics gives rise to a variation in the primary (P) and secondary (S) seismic wave speeds as the propagation direction is altered. This phenomena, called seismic anisotropy, can be utilized

6

by geophysicists to gain information on the mineralogy and structure of deeper parts of the earth by conducting seismic experiments and relating the obtained seismic anisotropy measures to particular rock fabric formations. This is extremely useful since rock fabric formations reflect the overall deformation of the Earth material and can be used not only to gain information on the mineralogy and structure of deeper parts of the Earth, but also to better understand the tectonic processes that have operated during geologic history.

To date, a number of detailed seismic studies have provided valuable information on the distribution of wave propagation velocities at deeper levels of the earth (Christensen, 1985; Christensen and Mooney, 1995; Mooney, 2007). Measurements of S-wave splitting, an important seismic anisotropy measure, are usually attributed to anisotropy in the mantle. For example, the alignment of the elastically anisotropic mineral olivine into a crystal lattice preferred orientation is directly linked to the kinematics of plastic flow in the mantle and to seismic anisotropy (Mainprice and Nicolas, 1989; Savage, 1999). In the crust, material anisotropy is also able to affect the S-wave splitting values caused by mantle structures. In order to do so, the degree of crustal anisotropy must be significant and appropriately oriented (Okaya *et al.*, 1995; Godfrey *et al.*, 2000). An example is the Alpine Fault in the South Island of New Zealand. The schist terranes in this location, schist being a particular type of rock fabric, are of large extent and thickness (approximately 10 to 20 km) and are steeply dipping, contributing to potentially 45% of the observed S-wave splitting (Godfrey *et al.*, 2000). While other causes for crustal material anisotropy include the presence of aligned fractures or cracks in the upper crust and the layering of isotropic material exist, it is the effect of anisotropic elastic properties of single crystals coupled with the rock fabric morphologies they create which are the focus of the work here.

With regard to experimental work in this area, there exist a number of laboratory velocity measurements for rock types that are believed to be important constituents of

Earth's crust and upper mantle (*e.g.* see (Birch, 1960/1961; Christensen, 1965/1966; Simmons, 1964)). These petrophysical data are determined by directing high frequency waves at an oriented rock sample. This sample is oriented based on the foliation defined by phyllosilicates in the rock, so fabric elements such as a lattice preferred orientation in the matrix crystals are not accounted for. By using five independent P and S-wave velocities measurements and assuming that the bulk material possesses hexagonal symmetry, the elastic stiffnesses can be calculated (Cristescu, 1989; Okaya and McEvilly, 2003). For this calculation, the measurements diagonal to the foliation direction are crucial, but difficult to perform. Therefore, these measurements are often inferred from the measurements obtained from experiments conducted parallel and perpendicular to the foliation plane. Okaya and Christensen (2002) have shown that this diagonal measurement profoundly influences S-wave speed behavior.

For materials with symmetries more complicated than the hexagonal variety, even more measurements are required to characterize their wave speed versus propagation direction response and thus, are used rarely for seismic anisotropy studies. More recently the use of electron backscatter diffraction data to calculate bulk properties of polycrystallographic rocks has gained in popularity. Based on the crystallographic orientations and constituent volume fractions derived by this method, a bulk stiffness tensor for the rock can be calculated and used to compute the anticipated seismic response of the sample. A common method used by the geophysical community to calculate the homogenized stiffness tensor is via a program written by Mainprice (1990). This program uses the elastic constants, density and volume fraction of each mineral to homogenize the elastic properties using the Voigt (1928) upper bound or arithmetic mean (Hill, 1952), which in turn can be used to compute the seismic wave speed behavior. Other commonly used homogenization techniques employed for these purpose include the Reuss (1929) lower bound and the geometric mean (Matthies and Humbert, 1993). The downside of using these analytical bounds

and estimates is that they do not consider grain shapes or the elastic interactions of these grains. The end result is that it is difficult to assess if the particular choice of homogenization is performing well or not, since for a given set of phase volume fractions and orientations, alterations in the grain sizes, geometries and distribution can greatly alter the true bulk stiffness. Therefore, even though computationally intensive homogenization schemes have been deemed tedious and impractical for most in the geophysical community (*e.g.* see(Ji, 2004)), accurately studying the effect of rock fabric characteristics on seismic anisotropy requires a rigorous homogenization method like AEH.

1.2 Overview of Thesis

1.2.1 Research Objectives

The first objective of the present dissertation is to develop a methodology for creating morphologically realistic heterogeneous two-phase random microstructures over the entire volume fraction range, and subsequently, analyze their statistical and homogenized thermoelastic material properties in an effort to extract valuable insight into the behavior of realistic random materials. To that end, the AEH method is used in conjunction with multiscale analysis to obtain the temperature and stresses at the microscopic and macroscopic levels. In addition, failure envelopes are presented for metal/ceramic and metal/metal heterogeneous materials through direct micromechanical failure analysis. It should be noted that the present methodology is applicable to heterogeneous bodies with spatially varying material composition. Functionally graded materials are a good example of heterogeneous materials that have spatially varying volume fractions and microstructure. As alluded to previously, FGMs are appealing in certain applications since they permit tailoring of material composition so as to derive maximum benefits from their inhomogeneity (Miyamoto *et al.*, 1999; Cho and Ha, 2002; Pelletier and Vel, 2006; Goupee and Vel, 2006/2007).

9

To address the first objective of the dissertation, a methodology for the simulation of morphologically realistic heterogeneous microstructures using random morphology description functions (RMDFs) is presented. In this approach, the interface between two material phases is defined through a level cut of a random field (Cahn, 1965). Roberts and Teubner (1995) used level cuts of Gaussian random fields to generate realistic random microstructures of this type and analyzed their effective conductivity for a variety of volume fractions. Roberts and Knackstedt (1996) investigated the conductivity, diffusivity and elastic moduli of Gaussian random field microstructures by deriving the microstructure statistical correlation functions and using them to evaluate rigorous bounds on each of the desired properties. To date, as was mentioned previously, the thermoelastic material properties and multiscale analysis of random heterogeneous materials of the type used in (Roberts and Teubner, 1995; Roberts and Knackstedt, 1996) has not been investigated. Accordingly, the homogenized thermomechanical properties of the two-phase RMDF created random microstructures are investigated in the present work. The simulated random microstructures visually compare very well with actual micrographs created via common two-phase material manufacturing techniques including plasma spraying (*e.g.* see (Kawasaki and Watanabe, 1997)) and powder processing (*e.g.* see (Aldrich *et al.*, 2000; Takagi *et al.*, 2003; Jin *et al.*, 2005)). More specifically, when the volume fraction of one phase is much smaller than the other, the resulting microstructure consists of particles of random shape and size scattered in a matrix phase. When the volume fractions are comparable, the resulting microstructure resembles an IPC with interconnected morphology. The characteristic size of the microstructural features can be controlled by varying the number of Gaussian source functions used to generate the morphology description function. The simulated RMDF microstructures are characterized using two-point probability functions and their effective thermomechanical material properties are determined using the AEH method (Torquato, 2002; Guedes and Kikuchi,

10

1990). The homogenized material properties for different material combinations and volume fractions are compared with the self-consistent estimate, Hashin-Shtrikman bounds and experimental results.

In addition to characterizing the thermoelastic material properties of random heterogeneous materials, this dissertation aims to address the fundamental problem of determining the local heat flux, strains, stresses and failure at the microstructural level for heterogeneous solid bodies that are subjected to applied thermal and mechanical loads. To that end, a multiscale analysis of random heterogeneous materials within the context of linear thermoelasticity is performed. The macroscopic heat conduction and thermoelastic analyses are performed using the finite element method. The corresponding heat flux and stresses at the microscale are evaluated using the interscale transfer operators. The coupled micro-macro analysis technique makes it possible to analyze the failure of random heterogeneous materials. For a prescribed macroscopic stress state, a direct micromechanical failure analysis is performed which entails determining the corresponding microstresses for the applied macroscopic stress state and then using appropriate material failure criteria at the microscale in order to determine the factor of safety of the material. Using direct micromechanical failure analysis, initial failure envelopes in the macroscopic principle stress domain are generated by varying the stress states at the macroscopic level and averaging the results over a sufficiently large ensemble of distinct random microstructures. The initial failure envelopes thus generated are useful in assessing the strength of heterogeneous components when precise information regarding the microstructure is lacking, which is often the case in practical applications. In addition, once the initial failure envelopes have been created for a particular random heterogeneous material combination, the envelopes can be used for analyzing components comprised of the same material without the need of a computationally expensive and time-consuming multiscale analysis for each new problem.

The multiscale analysis framework is illustrated through two model problems. The random heterogeneous components considered in both model problems are assumed to be functionally graded to demonstrate the applicability of the method to heterogeneous bodies with spatially varying material composition. In the first model problem, a simply supported aluminum/alumina (Al/Al_2O_3) functionally graded beam is investigated. The beam, which is graded in the thickness direction, is subjected to a distributed load on its top surface. The homogenized material properties at each location, which are necessary for the macroscopic analysis, are obtained using the AEH method. The factor of safety is determined from the macroscopic stresses in conjunction with the failure envelopes for Al/Al_2O_3 random heterogeneous materials. A detailed investigation of failure at the microstructural level is also performed for representative random microstructures at the critical location. In the second model problem, a tungsten/copper (W/Cu) functionally graded component is subjected to an intense heat flux on a portion of its boundary. A multiscale heat conduction and thermoelastic analysis is performed and the temperature, stresses and factor of safety are obtained at the macroscopic and microscopic levels.

The second object of this dissertation is to study the transient thermoelastic response of functionally graded materials using a multiscale approach. More specifically, two-phase functionally graded materials with varying microstructure morphologies will be analyzed using the AEH and finite element methods. The accuracy of the proposed multiscale approach is verified using two validation problems, these being the multiscale problem studied in (Fish and Wagiman, 1992; Ghosh *et al.*, 1995) and an exact transient solution for a functionally graded plate (Vel and Batra, 2003). Subsequently, results are presented for two model problems to demonstrate the potential of the multiscale approach as applied to functionally graded materials. The microstructure morphologies for the model problems are created for the entire range of volume fractions using a morphology description function (MDF) (Cahn, 1965;

de Ruiter and van Keulen, 2004; Cao and Liu, 2006), a concept very similar to the RMDF mentioned previously. The two model problems, the first being a copper/tungsten (W/Cu) specimen subject to a time-varying heat flux and the second a thermally loaded titanium/zirconium (Ti/ZrO_2) turbine blade, use the results from the multiscale analysis to perform a direct micromechanical failure analysis of the components. The results will demonstrate that a multiscale approach is necessary if one wishes to accurately analyze a functionally graded component with the intent of properly assessing component failure.

The final objective of this dissertation is to better characterize the influence of key rock fabric features on seismic anisotropy. These microscale characteristics include the phase volume fractions, the crystallographic shape and orientations as well as the spatial arrangements of the constituent crystals. To ascertain the influence of these key features, a systematic study of parametrized synthetic rock fabric microstructures consisting of quartz and muscovite grains will be analyzed using the AEH method and the resulting wave speed velocities as a function of propagation direction determined via the solution of the Christoffel equation (1877). The synthetic microstructures will feature variable muscovite volume fraction, muscovite inclusion orientation and quartz grain material orientation. An analysis of the generated wave speed data will be performed by computing and comparing key seismic wave speed anisotropy parameters. These will include the spread in the magnitudes of the P and S-wave speeds as propagation direction is altered, the relationship of the P-wave speed with a propagation direction diagonal to the foliation plane relative to the velocities perpendicular and parallel to the foliation plane as well as the spread in the two S-wave speed velocities as propagation direction is varied.

1.2.2 Research Contributions

The significance of this dissertation is in the use of rigorous multiscale methods to explore and better understand heterogeneous materials, such as advanced composite materials and polycrystalline rocks. The proposed research activities will first focus on the characterization and multiscale analysis of random heterogeneous engineering materials under combined thermal and mechanical loads. An additional, and related, area of research includes the utilization of multiscale methods for accurate failure analysis during the transient of thermally loaded functionally graded materials. The final area of research aims to identify the influence of key heterogeneous rock fabric morphological features on seismic wave speed anisotropy. The specific contributions of this thesis are as follows:

1. The homogenized thermoelastic material properties of two-phase random heterogeneous materials are characterized by creating synthetic microstructures via the RMDF method and analyzing the microstructures with the AEH method. The RMDF microstructures closely resemble micrographs of actual random heterogeneous materials and exhibit the desired morphological changes over the entire range of volume fractions. More specifically, the created microstructures resemble particles embedded in a matrix phase when the phase volume fractions are disparate and resemble an IPC when the phase volume fractions are similar. Using the combined RMDF and AEH methodology, the accuracy of commonly used analytic homogenization schemes for estimating the effective properties of random heterogeneous materials is assessed.

2. Using the RMDF microstructures and direct micromechanical failure analysis afforded by the AEH method, the failure response of random heterogeneous materials to both mechanical and thermal loads is characterized. More specifically, initial failure envelopes are created which not only give insight into the

14

dependence of random material strength on varying combined stress states and temperature increases, but also facilitate more an efficient failure analysis of heterogeneous material components. With the initial failure envelopes created, a novel, streamlined multiscale approach which employs the information provided by the failure envelopes is demonstrated on two model problems.

3. A multiscale methodology is presented for the accurate transient thermoelastic analysis of FGM components which accounts for the spatial variation of microstructural morphology. The factors of safety are computed at each time step using the direct micromechanical failure analysis approach, which entails utilizing microscale stress quantities in conjunction with phase specific failure criteria. The methodology is demonstrated on two model problems and insight is garnered with regard to the influence of the macroscopic field variables and microstructural morphology on the factor of safety of a transient thermally loaded FGM component.

4. The role of rock fabric characteristics on seismic wave speed anisotropy is investigated using parametrized synthetic quartz/muscovite microstructures coupled with the AEH and finite element method. In addition, the wave speeds obtained from the AEH stiffnesses are compared with those determined from common analytic estimates employed by the geophysical community to demonstrate the necessity of using an accurate homogenization scheme, such as AEH. A thorough parametric study of the synthetic rock fabric microstructures is conducted to ascertain the effect of grain volume fractions and orientations on seismic wave speed anisotropy.

1.2.3 Dissertation Outline

The dissertation is organized as follows. Chapter 2 presents the multiscale AEH formulation and the finite element method used for the computation of microscale and

macroscale fields. Chapter 2 also discusses the direct micromechanical failure analysis procedure employed in the random heterogeneous material and FGM portions of the work. Chapter 3 focuses on the characterization of the statistical and homogenized thermoelastic material properties of random heterogeneous materials. The direct micromechanical failure analysis and multiscale simulations of random heterogeneous materials is reserved for Chapter 4. In Chapter 5, the transient multiscale thermoelastic analysis of FGMs with the coupled AEH and finite element methods is explored. Chapter 6 discusses the characterization of seismic wave speed anisotropy in heterogeneous rock fabrics. Finally, Chapter 7 presents a summary of the conclusions drawn from the various studies performed in this work.

CHAPTER 2

MULTISCALE ANALYSIS USING THE ASYMPTOTIC EXPANSION HOMOGENIZATION METHOD

In this chapter, the multiscale formulation of the transient heat conduction and thermoelasticity problems using the AEH method is presented. Subsequently, the finite element solution of the microscale and macroscale problems is discussed. The final portion of this chapter details the direct micromechanical failure analysis procedure. Note that in the following derivations, indicial and direct notation is used interchangeably.

2.1 Heat Conduction Problem

Figure 2.1 depicts a two-phase functionally graded body with spatially varying microstructure. The response of the material at the microstructural level is analyzed using representative material elements (RMEs) of size ℓ, where ℓ is much smaller than the characteristic length L of the of the macroscopic body. Note that the ratio of the length scales is $\varepsilon = \ell/L$, where $\varepsilon << 1$. In addition, the coordinates used for analysis of the macroscopic problem $\mathbf{x}$ are related to the microscopic coordinates $\mathbf{y}$ as $\mathbf{y} = \mathbf{x}/\varepsilon$. Let $\mathbf{y} \in Y$ where $Y =]0, Y_1[\times]0, Y_2[\times]0, Y_3[$ is the RME domain and $]a, b[$ defines the open set. All field variables are assumed to depend on both the macroscopic and microscopic coordinates and time t, $i.e.$, $\Phi^\varepsilon = \Phi(\mathbf{x}, \mathbf{y}, t) = \Phi(\mathbf{x}, \mathbf{x}/\varepsilon, t)$, where the superscript ε is used to denote dependence of the variables on each of the length scales.

The transient temperature field is governed by conservation of thermal energy and Fourier's law of heat conduction ($e.g.$ see (Nowacki, 1975; Nowinski, 1978)),

$$-\frac{\partial q_i^\varepsilon}{\partial x_i} = \rho^\varepsilon C_v^\varepsilon \dot{\theta}^\varepsilon, \quad q_i^\varepsilon = -\kappa_{ij}^\varepsilon \frac{\partial \theta^\varepsilon}{\partial x_j}, \tag{1}$$

17
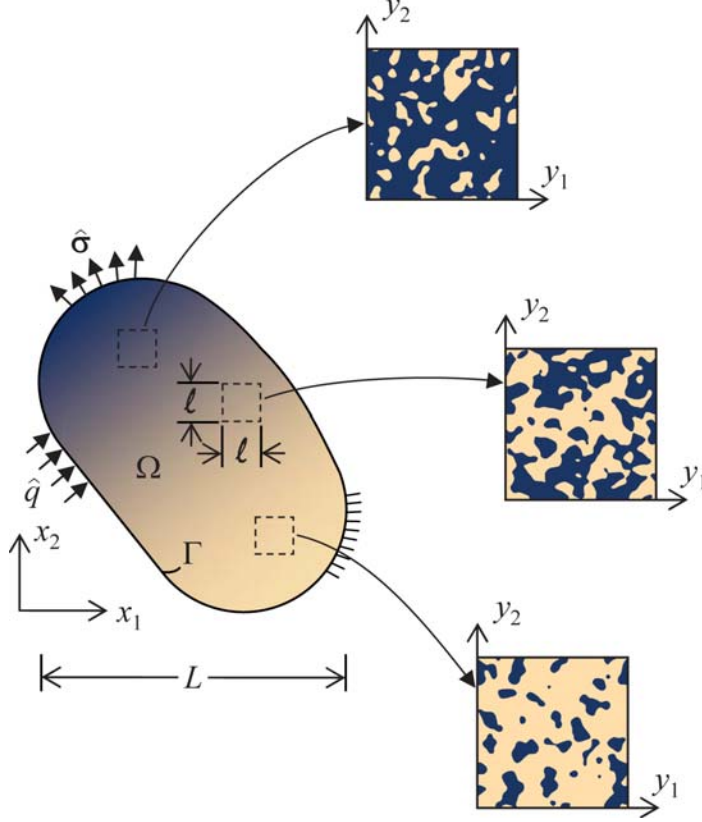
Figure 2.1. Schematic of two-phase functionally graded body with spatially varying microstructure.

where q_i^ε are the components of the heat flux vector, θ^ε is the change in temperature from the reference state, ρ^ε is the density and C_v^ε and κ_{ij}^ε are the specific heat capacity and thermal conductivity tensor, respectively. The corresponding thermal boundary conditions are

$$\theta^\varepsilon = \hat{\theta} \ \ \text{on} \ \ \Gamma_\theta,$$
$$-q_i^\varepsilon n_i = \hat{q} \ \ \text{on} \ \ \Gamma_q, \tag{2}$$
$$-q_i^\varepsilon n_i + h_c \left(\theta^\varepsilon - \theta_\infty \right) = 0 \ \ \text{on} \ \ \Gamma_c,$$

where $\hat{\theta}$ is the prescribed temperature on the boundary Γ_θ, $\hat{q}$ is the heat flux prescribed normal to the boundary Γ_q, n_i are the components of the vector outward normal to the boundary and h_c and θ_∞ are the convection coefficient and temperature of the surrounding media on the boundary Γ_c. The union of Γ_θ, Γ_q and Γ_c comprise the entire boundary Γ. The weak form of the heat conduction problem is obtained by

18

multiplying $(1)_1$ by a test function w, integrating over the domain Ω and utilizing $(1)_2$. The resulting weak form is

$$\int_\Omega \kappa_{ij}^\varepsilon \frac{\partial \theta^\varepsilon}{\partial x_j} \frac{\partial w}{\partial x_i} d\Omega = \int_\Omega \rho^\varepsilon C_v^\varepsilon \dot\theta^\varepsilon w d\Omega + \int_{\Gamma_q} \hat q w d\Gamma - \int_{\Gamma_c} h_c \left(\theta^\varepsilon - \theta_\infty\right) w d\Gamma \ \forall \ w(\mathbf{x}, \mathbf{y}). \quad (3)$$

To proceed with the multiscale formulation of the heat conduction problem, a two-scale asymptotic expansion is assumed for the temperature field (Bensoussan *et al.*, 1978; Sanchez-Palencia, 1983),

$$\theta^\varepsilon(\mathbf{x}, t) = \theta^0(\mathbf{x}, \mathbf{y}, t) + \varepsilon \theta^1(\mathbf{x}, \mathbf{y}, t) + \varepsilon^2 \theta^2(\mathbf{x}, \mathbf{y}, t) + \dots . \quad (4)$$

In further derivations, it will be useful to note that by using the chain rule and the definition of $\mathbf{y}$ that

$$\frac{d\eta^\varepsilon(\mathbf{x}, t)}{dx_i} = \frac{\partial \eta^\varepsilon(\mathbf{x}, \mathbf{y}, t)}{\partial x_i} + \frac{1}{\varepsilon} \frac{\partial \eta^\varepsilon(\mathbf{x}, \mathbf{y}, t)}{\partial y_i}, \quad (5)$$

and in addition, for a periodic function $\Psi(\mathbf{y})$, as $\varepsilon \to 0^+$, that

$$\int_\Omega \Psi(\frac{\mathbf{x}}{\varepsilon}) d\Omega = \frac{1}{|Y|} \int_\Omega \int_Y \Psi(\mathbf{y}) dY d\Omega. \quad (6)$$

Substitution of $\theta^\varepsilon(\mathbf{x}, t)$ from (4) into the first term of (3) and making use of the relation (5) results in

$$\int_\Omega \kappa_{ij}^\varepsilon \left\{ \varepsilon^{-2} \frac{\partial \theta^0}{\partial y_j} \frac{\partial w}{\partial y_i} + \varepsilon^{-1} \left[\frac{\partial \theta^0}{\partial y_j} \frac{\partial w}{\partial x_i} + \left(\frac{\partial \theta^0}{\partial x_j} + \frac{\partial \theta^1}{\partial y_j} \right) \frac{\partial w}{\partial y_i} \right] + \right.$$
$$\left. \left[\left(\frac{\partial \theta^0}{\partial x_j} + \frac{\partial \theta^1}{\partial y_j} \right) \frac{\partial w}{\partial x_i} + \left(\frac{\partial \theta^1}{\partial x_j} + \frac{\partial \theta^2}{\partial y_j} \right) \frac{\partial w}{\partial y_i} \right] + \varepsilon(\dots) \right\} d\Omega \quad (7)$$
$$= \int_\Omega \rho^\varepsilon C_v^\varepsilon \dot\theta^\varepsilon w d\Omega + \int_{\Gamma_q} \hat q w d\Gamma - \int_{\Gamma_c} h_c \left(\theta^\varepsilon - \theta_\infty\right) w d\Gamma.$$

It can be demonstrated that $\theta^0(\mathbf{x}, \mathbf{y}, t) = \theta^0(\mathbf{x}, t)$ by multiplying (7) by ε^2, choosing the test function $w = \theta^0$, taking the limit as $\varepsilon \to 0^+$ and noting that κ_{ij} is positive definite.

19

A key component of the multiscale formulation is to assume a decomposition for $\theta^1(\mathbf{x}, \mathbf{y}, t)$ in terms of $\theta^0(\mathbf{x}, t)$ in the form (Bensoussan *et al.*, 1978; Sanchez-Palencia, 1983)

$$\theta^1(\mathbf{x}, \mathbf{y}, t) = -\phi^k(\mathbf{x}, \mathbf{y}, t)\frac{\partial\theta^0(\mathbf{x}, t)}{\partial x_k}, \tag{8}$$

where $\phi^k(\mathbf{x}, \mathbf{y}, t)$ are auxiliary microstructural fields that relate the first order terms to the zeroth order terms in the asymptotic expansion for the temperature field. To obtain an equation for the solution of $\phi^k(\mathbf{x}, \mathbf{y}, t)$, the decomposition (8) is inserted into (7) and the resulting expression is multiplied by ε. Subsequently, the limit is taken as $\varepsilon \to 0^+$ with the test function choice $w = w(\mathbf{y})$. Noting that Ω and $\partial\theta^0/\partial x_k$ are arbitrary, one obtains the weak form for $\phi^k(\mathbf{x}, \mathbf{y}, t)$,

$$\int_Y \kappa_{ij}^\varepsilon \frac{\partial\phi^k}{\partial y_j}\frac{\partial w(\mathbf{y})}{\partial y_i}dY = \int_Y \kappa_{ik}^\varepsilon \frac{\partial w(\mathbf{y})}{\partial y_i}dY \ \forall \ w(\mathbf{y}). \tag{9}$$

The auxiliary fields $\phi^k(\mathbf{x}, \mathbf{y}, t)$ for $k = 1, 2, 3$ are subject to periodic boundary conditions over the RME domain Y. It should be noted that the thermal conductivities κ_{ij}^ε can vary as a function of time, for example when considering temperature dependent material properties.

Equating terms of ε^0 in (7), choosing the test function $w = w(\mathbf{x})$ and taking the limit as $\varepsilon \to 0^+$ yields the weak form of the macroscopic equation for θ^0, which is

$$\int_\Omega \kappa_{ij}^H \frac{\partial\phi^k}{\partial x_j}\frac{\partial w(\mathbf{x})}{\partial x_i}dY$$
$$= \int_\Omega \rho^H C_v^H \dot{\theta}^0 w(\mathbf{x})d\Omega + \int_{\Gamma_q} \hat{q}w(\mathbf{x})d\Gamma - \int_{\Gamma_c} h_c\left(\theta^0 - \theta_\infty\right)w(\mathbf{x})d\Gamma \ \forall \ w(\mathbf{x}), \tag{10}$$

where κ_{ij}^H is the homogenized thermal conductivity, ρ^H is the homogenized density and C_v^H is the homogenized specific heat capacity. The homogenized quantities are

$$\kappa_{ik}^H(\mathbf{x}, t) = \frac{1}{|Y|}\int_Y \left(\kappa_{ik}^\varepsilon - \kappa_{ij}^\varepsilon\frac{\partial\phi^k}{\partial y_j}\right)dY, \quad \rho^H(\mathbf{x}, t) = \frac{1}{|Y|}\int_Y \rho^\varepsilon dY,$$

$$C_v^H(\mathbf{x}, t) = \frac{1}{|Y|}\int_Y C_v^\varepsilon dY. \tag{11}$$

20

Note that the homogenized thermal conductivity requires the solution for $\phi^k(\mathbf{x}, \mathbf{y}, t)$.

Once the macroscopic temperature field $\theta^0(\mathbf{x}, t)$ is found via the solution of (10), one can begin the process of determining the microflux components. Using the expansion (4) and Fourier's law $(1)_2$, the following expansion for the heat flux q_i^ε is obtained

$$q_i^\varepsilon(\mathbf{x}, t) = q_i^0(\mathbf{x}, \mathbf{y}, t) + \varepsilon q_i^1(\mathbf{x}, \mathbf{y}, t) + \varepsilon^2 q_i^2(\mathbf{x}, \mathbf{y}, t) + \dots. \tag{12}$$

Since ε is small, the term $q_i^0(\mathbf{x}, \mathbf{y}, t)$ represents the microscopic heat flux components. The microscopic heat flux components can be related to the macroscopic temperature gradients via an *interscale transfer operator* of the form

$$q_i^0(\mathbf{x}, \mathbf{y}, t) = \kappa_{ij}^\varepsilon \left(\delta_{jk} - \frac{\partial \phi^k(\mathbf{x}, \mathbf{y}, t)}{\partial y_j} \right) \frac{\partial \theta^0(\mathbf{x}, t)}{\partial x_k}. \tag{13}$$

Lastly, it is noted that average macroscopic flux components $\bar{q}_i(\mathbf{x}, t)$ are determined by simply integrating the corresponding microscopic quantities $q_i^0(\mathbf{x}, \mathbf{y}, t)$ over the RME domain Y and dividing by the RME volume $|Y|$.

2.2 Thermoelasticity Problem

For the thermoelasticity problem, the equations of motion and constitutive relationship are (*e.g.* see (Nowacki, 1975; Nowinski, 1978))

$$\frac{\partial \sigma_{ij}^\varepsilon}{\partial x_j} = \rho^\varepsilon \ddot{u}_i^\varepsilon, \quad \sigma_{ij}^\varepsilon = C_{ijkl}^\varepsilon e_{kl}^\varepsilon - \beta_{ij}^\varepsilon \theta^\varepsilon, \tag{14}$$

where σ_{ij}^ε are the components of the Cauchy stress tensor, u_i^ε are the displacement components, C_{ijkl} are the elastic constants, β_{ij}^ε are the stress-temperature moduli and e_{kl}^ε are the components of the infinitesimal strain tensor. Note that the strains e_{kl}^ε are related to the displacement via the relation

$$e_{kl}^\varepsilon = \frac{1}{2} \left(\frac{\partial u_k^\varepsilon}{\partial x_l} + \frac{\partial u_l^\varepsilon}{\partial x_k} \right). \tag{15}$$

The mechanical boundary conditions for $(14)_1$ are

$$\begin{aligned} u_i^\varepsilon &= \hat{u}_i \quad \text{on} \quad \Gamma_u, \\ \sigma_{ij}^\varepsilon n_j &= \hat{\sigma}_i \quad \text{on} \quad \Gamma_\sigma, \end{aligned} \tag{16}$$

where $\hat{u}_i$ are the prescribed displacements on the boundary Γ_u and $\hat{\sigma}_i$ are the prescribed tractions on the boundary Γ_σ. Note that the union of Γ_u and Γ_σ comprise the entire boundary Γ. The weak form of the equations of motion are obtained by multiplying $(14)_1$ by a test vector v_i, utilizing the constitutive relation $(14)_2$, integrating over the domain Ω and making use of the divergence theorem. The resulting weak-form of the thermoelasticity problem is

$$\int_\Omega C^\varepsilon_{ijkl} \frac{\partial u^\varepsilon_k}{\partial x_l} \frac{\partial v_i}{\partial x_j} d\Omega - \int_\Omega \beta^\varepsilon_{ij} \theta^\varepsilon \frac{\partial v_i}{\partial x_j} d\Omega = \int_\Omega \rho^\varepsilon \ddot{u}^\varepsilon_i v_i d\Omega + \int_{\Gamma_\sigma} \hat{\sigma}_i v_i d\Gamma \ \forall \ v_i(\mathbf{x}, \mathbf{y}). \qquad (17)$$

Similar to the temperature field in the heat conduction problem, a two scale asymptotic expansion is assumed for the displacements in the form (Francort, 1983; Brahim-Otsmane *et al.*, 1998)

$$u^\varepsilon_i(\mathbf{x}, t) = u^0_i(\mathbf{x}, \mathbf{y}, t) + \varepsilon u^1_i(\mathbf{x}, \mathbf{y}, t) + \varepsilon^2 u^2_i(\mathbf{x}, \mathbf{y}, t) \dots . \qquad (18)$$

Substitution of the expansions (4) and (18) into the first two terms of the weak form (17) yields

$$\int_\Omega C^\varepsilon_{ijkl} \left\{ \varepsilon^{-2} \frac{\partial u^0_k}{\partial y_l} \frac{\partial v_i}{\partial y_j} + \varepsilon^{-1} \left[\left(\frac{\partial u^0_k}{\partial x_l} + \frac{\partial u^1_k}{\partial y_l} \right) \frac{\partial v_i}{\partial y_j} + \frac{\partial u^0_k}{\partial y_l} \frac{\partial v_i}{\partial x_j} \right] + \right.$$

$$\left. \left[\left(\frac{\partial u^0_k}{\partial x_l} + \frac{\partial u^1_k}{\partial y_l} \right) \frac{\partial v_i}{\partial x_j} + \left(\frac{\partial u^1_k}{\partial x_l} + \frac{\partial u^2_k}{\partial y_l} \right) \frac{\partial v_i}{\partial y_j} + \varepsilon \left(\dots \right) \right] \right\} d\Omega -$$

$$\int_\Omega \beta^\varepsilon_{ij} \left[\varepsilon^{-1} \theta^0 \frac{\partial v_i}{\partial y_j} + \left(\theta^0 \frac{\partial v_i}{\partial x_j} + \theta^1 \frac{\partial v_i}{\partial y_j} \right) + \varepsilon \left(\dots \right) \right] d\Omega$$

$$= \int_\Omega \rho^\varepsilon \ddot{u}^\varepsilon_i v_i d\Omega + \int_{\Gamma_\sigma} \hat{\sigma}_i v_i d\Gamma.$$

(19)

Multiplication of (19) by ε^2, choosing $v_i = u^0_i$, taking the limit as $\varepsilon \to 0^+$ and noting that C^ε_{ijkl} is positive-definite requires that the first order term in the displacement expansion not be a function of $\mathbf{y}$, *i.e.*, $u^0_k(\mathbf{x}, \mathbf{y}, t) = u^0_k(\mathbf{x}, t)$.

To proceed with the multiscale formulation, the following decomposition is used for $u^1_k(\mathbf{x}, \mathbf{y}, t)$ (Bensoussan *et al.*, 1978; Francort, 1983; Brahim-Otsmane *et al.*, 1998)

$$u^1_k(\mathbf{x}, \mathbf{y}, t) = -\chi^{pq}_k(\mathbf{x}, \mathbf{y}, t) \frac{\partial u^0_p(\mathbf{x}, t)}{\partial x_q} + \psi_k(\mathbf{x}, \mathbf{y}, t) \theta^0(\mathbf{x}, t), \qquad (20)$$

22

where $\chi_k^{pq}(\mathbf{x}, \mathbf{y}, t)$ and $\psi_k(\mathbf{x}, \mathbf{y}, t)$ are auxiliary functions that relate the first order term in the asymptotic expansion for the displacement to the zeroth order terms for the displacement and temperature, respectively. To obtain equations for $\chi_k^{pq}(\mathbf{x}, \mathbf{y}, t)$ and $\psi_k(\mathbf{x}, \mathbf{y}, t)$, the decomposition is first inserted into (19). Choosing the test function $v_i = v_i(\mathbf{y})$, multiplying (19) by ε, taking the limit as $\varepsilon \to 0^+$ and noting that Ω, $\partial u_p^0 / \partial x_q$ and θ^0 are arbitrary yields the following result,

$$
\begin{aligned}
\int_Y C_{ijkl}^\varepsilon \frac{\partial \chi_k^{pq}}{\partial y_l} \frac{\partial v_i(\mathbf{y})}{\partial y_j} dY &= \int_Y C_{ijpq}^\varepsilon \frac{\partial v_i(\mathbf{y})}{\partial y_j} dY \ \forall \ v_i(\mathbf{y}), \\
\int_Y C_{ijkl}^\varepsilon \frac{\partial \psi_k}{\partial y_l} \frac{\partial v_i(\mathbf{y})}{\partial y_j} dY &= \int_Y \beta_{ij}^\varepsilon \frac{\partial v_i(\mathbf{y})}{\partial y_j} dY \ \forall \ v_i(\mathbf{y}).
\end{aligned}
\tag{21}
$$

As was the case for $\phi^k(\mathbf{x}, \mathbf{y}, t)$ in the heat conduction problem, both $\chi_k^{pq}(\mathbf{x}, \mathbf{y}, t)$ and $\psi_k(\mathbf{x}, \mathbf{y}, t)$ are subject to periodic boundary conditions over the RME domain Y. The weak form of the equations of motion for the macroscopic displacements $u_k^0(\mathbf{x}, t)$ is obtained by equating terms of ε^0 in equation (19). Next, the test function choice $v_i = v_i(\mathbf{x})$ is selected and the limit is taken as $\varepsilon \to 0^+$, to obtain the macroscopic governing equation

$$
\int_\Omega C_{ijkl}^H \frac{\partial u_k^0}{\partial x_l} \frac{\partial v_i}{\partial x_j} d\Omega = \int_\Omega \rho^H \ddot{u}_i^0 v_i d\Omega + \int_\Omega \beta_{ij}^H \theta^0 \frac{\partial v_i}{\partial x_j} d\Omega + \int_{\Gamma_\sigma} \hat{\sigma}_i v_i d\Gamma \ \forall \ v_i(\mathbf{x}),
\tag{22}
$$

where C_{ijkl}^H, β_{ij}^H and ρ^H are the respective homogenized elastic stiffnesses, stress-temperature moduli and density. The aforementioned homogenized properties are computed through the expressions

$$
\begin{aligned}
C_{ijkl}^H(\mathbf{x}, t) &= \frac{1}{|Y|} \int_Y \left(C_{ijkl}^\varepsilon - C_{ijpq}^\varepsilon \frac{\partial \chi_p^{kl}}{\partial y_q} \right) dY, \\
\beta_{ij}^H(\mathbf{x}, t) &= \frac{1}{|Y|} \int_Y \left(\beta_{ij}^\varepsilon - C_{ijkl}^\varepsilon \frac{\partial \psi_k}{\partial y_l} \right) dY, \\
\rho^H(\mathbf{x}, t) &= \frac{1}{|Y|} \int_Y \rho^\varepsilon dY,
\end{aligned}
\tag{23}
$$

23

where the tensors C_{ijkl}^H and β_{ij}^H require knowledge of $\chi_k^{pq}(\mathbf{x}, \mathbf{y}, t)$ and $\psi_k(\mathbf{x}, \mathbf{y}, t)$, respectively.

Once the macroscopic displacements $u_k^0(\mathbf{x}, t)$ in (22) and macroscopic temperature $\theta^0(\mathbf{x}, t)$ are known, the microscopic stress components can be computed. It is first noted that an asymptotic expansion for the stresses σ_{ij}^ε can be created utilizing expansions (4) and (20) in the constitutive relationship $(14)_2$ yielding

$$\sigma_{ij}^\varepsilon(\mathbf{x}, t) = \sigma_{ij}^0(\mathbf{x}, \mathbf{y}, t) + \varepsilon \sigma_{ij}^1(\mathbf{x}, \mathbf{y}, t) + \varepsilon^2 \sigma_{ij}^2(\mathbf{x}, \mathbf{y}, t) + \dots. \tag{24}$$

With ε being a small quantity, the microstresses are essentially the first order term in (24), $\sigma_{ij}^0(\mathbf{x}, \mathbf{y}, t)$. The microstresses are related to the macroscopic strains $e_{kl}^0(\mathbf{x}, t) = \left(\partial u_k^0(\mathbf{x}, t)/\partial x_l + \partial u_l^0(\mathbf{x}, t)/\partial x_k\right)/2$ and macroscopic temperature $\theta^0(\mathbf{x}, t)$ via the *interscale transfer operator*

$$
\begin{aligned}
\sigma_{ij}^0(\mathbf{x}, \mathbf{y}, t) = {}& C_{ijkl}^\varepsilon \left(\delta_{kp} \delta_{lq} - \frac{\partial \chi_k^{pq}(\mathbf{x}, \mathbf{y}, t)}{\partial y_l} \right) \frac{\partial u_p^0(\mathbf{x}, t)}{\partial x_q} \\
& - \left(\beta_{ij}^\varepsilon - C_{ijkl}^\varepsilon \frac{\partial \psi_k(\mathbf{x}, \mathbf{y}, t)}{\partial y_l} \right) \theta^0(\mathbf{x}, t).
\end{aligned}
\tag{25}
$$

To determine the average macroscopic stress tensor $\bar{\sigma}_{ij}(\mathbf{x}, t)$, one simply integrates the corresponding microscopic components over the RME domain Y and divides by the RME volume $|Y|$.

2.3 Finite Element Formulation

In this section, the details of the finite element method for computing the field variables of interest at the microscopic and macroscopic length scales is presented. First, the solutions for the microscale fields $\phi^k(\mathbf{x}, \mathbf{y}, t)$, $\chi_k^{pq}(\mathbf{x}, \mathbf{y}, t)$ and $\psi_k(\mathbf{x}, \mathbf{y}, t)$, which are required for the computation of the homogenized material properties, microfluxes and microstresses, are discussed. Subsequently, the finite element solutions for the transient macroscopic field quantities $\theta^0(\mathbf{x}, t)$ and $u_k^0(\mathbf{x}, t)$ are presented.

2.3.1 Microscale Problems

To obtain a finite element solution for the microscale heat conduction problem, the field $\phi^k(\mathbf{x}, \mathbf{y}, t)$ and test function $w(\mathbf{y})$ are discretized in the RME domain Y as

$$\phi^k = \tilde{N}_b(\mathbf{y})\tilde{d}_b^k, \quad w = \tilde{N}_a(\mathbf{y})\tilde{c}_a, \quad k = 1, 2, 3, \quad a, b = 1, 2, \ldots, N_d^\mu, \tag{26}$$

where N_d^μ is the number of nodes in the domain, $\tilde{N}_b(\mathbf{y})$ is the finite element shape function associated with node b, $\tilde{c}_a$ are the nodal constants associated with the test function and $\tilde{d}_b^k$ are nodal constants to be solved for. Substitution of ϕ^k and w from (26) into (9) and noting that the result must hold for all test function nodal constants $\tilde{c}_a$ yields the set of algebraic equations for nodal constants $\tilde{d}_Q^k$

$$\tilde{K}_{PQ}\tilde{d}_Q^k = \tilde{F}_P^k, \tag{27}$$

where the node numbers a,b are related to the equations numbers P,Q via the mapping ID as $P = ID(a)$, $Q = ID(b)$, $\tilde{K}_{PQ}$ is the thermal stiffness matrix and $\tilde{F}_p^k$ the load vector. The stiffness matrix and load vector are computed as

$$\tilde{K}_{PQ} = \left(\sum_{r=1}^{N_e^\mu} \tilde{\mathbf{k}}^r\right)_{PQ}, \quad \tilde{F}_P^k = \left(\sum_{r=1}^{N_e^\mu} \tilde{\mathbf{k}}^r \tilde{\mathbf{d}}_o^{rk}\right)_P, \quad \tilde{\mathbf{k}}^r = \int_{Y^r} \tilde{\mathbf{B}}_a^T \boldsymbol{\kappa}^\varepsilon \tilde{\mathbf{B}}_b dY, \tag{28}$$

where $\tilde{\mathbf{k}}^r$ is the element stiffness matrix, N_e^μ is the number of elements, Y^r is the volume associated with element r, $\tilde{\mathbf{B}}_a = \boldsymbol{\nabla}\tilde{N}_a$ and $\tilde{\mathbf{d}}_o^{rk}$ are the nodal temperatures corresponding to a linear temperature variation in the y_k-direction of unit slope for element r. It should be noted that while the preceding expressions are valid for a three dimensional microstructures, the geometries of concern in this paper are all two-dimensional. Therefore, only the test cases corresponding to $k = 1, 2$ need to be performed, and hence, a two-dimensional finite element mesh is sufficient.

For the microscale thermomechanical problem, a solution for the vector field $\chi_i^{kl}(\mathbf{x}, \mathbf{y}, t)$ is sought first. The desired vector field and test vector $v_i(\mathbf{y})$ are both discretized in terms of finite element shape functions $\tilde{N}_b(\mathbf{y})$ and nodal constants as

$$\chi_i^{kl} = \tilde{N}_b(\mathbf{y})\hat{d}_{bi}^{kl}, \quad v_i = \tilde{N}_a(\mathbf{y})\hat{c}_{ai}, \quad k,l = 1,2,3, \tag{29}$$

where $\hat{c}_{ai}$ are nodal constants associated with the test vector and $\hat{d}_{bi}^{kl}$ are nodal constants to be determined. Insertion of (29) into the weak form $(21)_1$ and noting that the result must hold for all $\hat{c}_{ai}$ produces the solution for the nodal constants $\hat{d}_{bi}^{kl}$

$$\hat{K}_{PQ}\hat{d}_Q^{kl} = \hat{F}_P^{kl}, \tag{30}$$

where $\hat{K}_{PQ}$ is the stiffness matrix and $\hat{F}_P^{kl}$ the load vector for the test case denoted by the indices k and l. The equation numbers P,Q in (30) are related to the nodal numbers and vector indices through the mapping ID as $P = ID(a,i)$, $Q = ID(b,j)$. The stiffness matrix and load vector in equation (30) are computed as

$$\hat{K}_{PQ} = \left(\sum_{r=1}^{N_e^\mu} \hat{\mathbf{k}}^r\right)_{PQ}, \quad \hat{F}_P^{kl} = \left(\sum_{r=1}^{N_e^\mu} \hat{\mathbf{k}}^r \hat{\mathbf{d}}_o^{rkl}\right)_P,$$

$$\hat{\mathbf{k}}^r = \mathbf{e}_i^T \left(\int_{Y^r} \hat{\mathbf{B}}_a^T \mathbf{D}^\varepsilon \hat{\mathbf{B}}_b dY\right) \mathbf{e}_j, \tag{31}$$

$\hat{\mathbf{d}}_o^{rkl}$ being displacements for element r associated with the unit strain e_{kl}^o, $\mathbf{e}_i$ the unit vector along the y_i coordinate, $\mathbf{D}^\varepsilon$ the 6×6 contraction of C_{ijkl}^ε and $\hat{\mathbf{B}}_a$ a matrix of shape function spatial derivatives,

$$\hat{\mathbf{B}}_a^T = \begin{bmatrix} \dfrac{\partial \tilde{N}_a}{\partial y_1} & 0 & 0 & 0 & \dfrac{\partial \tilde{N}_a}{\partial y_3} & \dfrac{\partial \tilde{N}_a}{\partial y_2} \\[3mm] 0 & \dfrac{\partial \tilde{N}_a}{\partial y_2} & 0 & \dfrac{\partial \tilde{N}_a}{\partial y_3} & 0 & \dfrac{\partial \tilde{N}_a}{\partial y_1} \\[3mm] 0 & 0 & \dfrac{\partial \tilde{N}_a}{\partial y_3} & \dfrac{\partial \tilde{N}_a}{\partial y_2} & \dfrac{\partial \tilde{N}_a}{\partial y_1} & 0 \end{bmatrix}. \tag{32}$$

To obtain a solution for $\psi_k(\mathbf{x},\mathbf{y},t)$, a similar discretization using finite element shape functions is employed and is of the form

$$\psi_k = \tilde{N}_b(\mathbf{y})\hat{g}_{bk}, \tag{33}$$

where $\hat{g}_{bk}$ are the desired nodal constants. Inserting (33) and the discretized form of the test functions $(29)_2$ into $(21)_2$ and requiring that the result must hold for all $\hat{c}_{ai}$ yields the algebraic equations

26

$$\hat{K}_{PQ}\hat{g}_{bk} = \hat{H}_P, \tag{34}$$

where $\hat{H}_P$ is the load vector and $\hat{K}_{PQ}$ is the same as in $(31)_1$. The load vector $\hat{H}_P$ is computed as

$$\hat{H}_P = \left(\sum_{r=1}^{N_e^\mu} \hat{\mathbf{k}}^r \hat{\mathbf{g}}_o^r\right)_P, \tag{35}$$

where $\hat{\mathbf{g}}_o^r$ are the nodal displacements for element r associated with the free thermal expansion corresponding to a unit temperature change, $e_{kl}^\alpha = \alpha_{kl}^\varepsilon$, α_{kl}^ε being the thermal expansion coefficients. The presented approximate solutions for $\chi_k^{pq}(\mathbf{x}, \mathbf{y}, t)$ and $\psi_k(\mathbf{x}, \mathbf{y}, t)$ are applicable to three-dimensional microstructures, however, as previously mentioned only two-dimensional geometries are of interest here. By retaining all three components of the desired solutions, albeit, restricting them to vary only in the $y_1 - y_2$ plane, all of the nonzero components of the tensors C_{ijkl}^H and β_{ij}^H and microstresses $\sigma_{ij}^0(\mathbf{x}, \mathbf{y}, t)$ can be computed using a two-dimensional finite element formulation. If plane stress conditions prevail at the macroscale, one need only perform a plane stress reduction of the obtained thermoelastic constants.

2.3.2 Macroscale Problems

To solve the macroscopic heat conduction problem (10), the macroscopic temperature $\theta^0(\mathbf{x}, t)$ and test functions $w(\mathbf{x})$ are discretized as

$$\theta^0 = \hat{N}_b(\mathbf{x})\tilde{s}_b, \quad w = \hat{N}_a(\mathbf{x})\tilde{q}_a, \quad a, b = 1, 2, \ldots, N_d, \tag{36}$$

where $\hat{N}_b(\mathbf{x})$ is the finite element shape function associated with node b, $\tilde{q}_a$ are test function nodal constants, $\tilde{s}_b$ are time-varying nodal temperature constants and N_d is the number of finite element nodes. Insertion of the discretized temperature and test function from (36) into the weak form (10) and noting that the result must hold for all constants $\tilde{q}_a$ yields a system of first-order ordinary differential equations in time for $\tilde{s}_b$,

$$\tilde{M}_{PQ}\dot{\tilde{s}}_Q + \tilde{L}_{PQ}\tilde{s}_Q = \tilde{G}_P, \tag{37}$$

where nodal numbers a, b are mapped into the equation numbers P, Q by the relations $P = ID(a)$, $Q = ID(b)$, $\tilde{M}_{PQ}$ and $\tilde{L}_{PQ}$ are the respective thermal mass and stiffnessmatrices and $\tilde{G}_P$ is the thermal load vector. The matrices and vector of (37) are computed as

$$\tilde{M}_{PQ} = \int_{\Omega} \rho^H C_v^H \hat{N}_a \hat{N}_b d\Omega,$$

$$\tilde{L}_{PQ} = \int_{\Omega} \boldsymbol{\nabla} \hat{N}_a^T \boldsymbol{\kappa}^H \boldsymbol{\nabla} \hat{N}_b d\Omega + \int_{\Gamma_c} h_c \hat{N}_a \hat{N}_b d\Gamma, \qquad (38)$$

$$\tilde{G}_P = \int_{\Gamma_q} \hat{q} \hat{N}_a d\Gamma + \int_{\Gamma_c} h_c \theta_\infty \hat{N}_a d\Gamma.$$

The discrete heat conduction equations (37) are integrated in time using the Galerkin scheme from the α-family of implicit time integration methods (*e.g.* see (Reddy, 1993)). If steady state conditions prevail, (37) becomes a set of simultaneous coupled algebraic equations and is solved using standard techniques.

To obtain a solution for the macroscopic thermoelasticity problem (22), the macroscopic displacements $u_j^0(\mathbf{x}, t)$ and test functions $v_i(\mathbf{x})$ are discretized in a similar fashion to the heat conduction problem, yielding

$$u_j^0 = \hat{N}_b(\mathbf{x})\hat{s}_{bj}, \quad v_i = \hat{N}_a(\mathbf{x})\hat{q}_{ai}, \qquad (39)$$

$\hat{q}_{ai}$ being nodal constants associated with the test vector and $\hat{s}_{bj}$ the time-varying nodal constants to be determined. Utilizing the discretization (39) in the weak form of the macroscopic equations of motion (22) results in a system of second-order ordinary differential equations for $\hat{s}_{bj}$,

$$\hat{M}_{PQ}\ddot{\hat{s}}_Q + \hat{L}_{PQ}\hat{s}_Q = \hat{G}_P, \qquad (40)$$

where the nodal values are related to the global equations numbers through the mapping $P = ID(a, i)$, $Q = ID(b, j)$, $\hat{M}_{PQ}$ is the mass matrix, $\hat{L}_{PQ}$ is the stiffness

matrix and $\hat{G}_P$ is the load vector. The matrices $\hat{M}_{PQ}$, $\hat{L}_{PQ}$ and vector $\hat{G}_P$ have the definitions

$$\hat{M}_{PQ} = \mathbf{e}_i^T \left(\int_{\Omega} \rho^H \hat{N}_a \hat{N}_b d\Omega \right) \mathbf{e}_j,$$

$$\hat{L}_{PQ} = \mathbf{e}_i^T \left(\int_{\Omega} \mathbf{B}_a^T \mathbf{D}^H \mathbf{B}_b d\Omega \right) \mathbf{e}_j, \tag{41}$$

$$\hat{G}_P = \mathbf{e}_i^T \left(\int_{\Omega} \theta^0 \mathbf{B}_a^T \boldsymbol{\beta}^H d\Omega \right) - \mathbf{e}_i^T \left(\int_{\Gamma_u} \theta^0 \hat{N}_a \beta_{ij}^H n_j d\Gamma \right) + \mathbf{e}_i^T \left(\int_{\Omega} \hat{N}_a \hat{\sigma}_i d\Gamma \right),$$

where $\mathbf{D}^H$ is the 6×6 contraction of C_{ijkl}^H, $\mathbf{B}_a$ is a matrix of shape function derivatives similar to (32), albeit with $\tilde{N}_a$ replaced with $\hat{N}_a$ and y replaced with x, and $\boldsymbol{\beta}^H$ is the 6×1 vector form of the homogenized stress-temperature moduli β_{ij}^H. The second-order ordinary differential equations for $\hat{s}_Q$ are solved using the Galerkin scheme from the Newmark family of implicit time integration schemes (*e.g.* see (Reddy, 1993)). Similar to the heat conduction problem, if steady state conditions prevail, (40) becomes a set of simultaneous coupled algebraic equations and is solved using standard techniques.

2.4 Direct Micromechanical Failure Analysis

A major reason for performing a multiscale analysis is to accurately compute the stress fields at the microscale, which in turn, allows for a more accurate evaluation of material failure via application of phase specific failure criteria. The ability to perform a direct micromechanical failure analysis is one of the main advantages of the multiscale approach.

To begin the direct micromechanical failure analysis process, the microstresses are determined via the interscale transfer operators at key locations throughout the macroscopic body, for example, at the quadrature points or nodes from the macroscopic analysis. At each of these locations, the microstresses are entered into phase specific failure criteria and a factor of safety is computed over the entire RME domain Y. If

29

the material phase in question is ductile, the von Mises failure criterion is used (*e.g.* see (Dowling, 2006)). The factor of safety for ductile materials is computed as

$$F_s^{ductile}(\mathbf{x}, \mathbf{y}, t) = \frac{S_y}{\sigma'(\mathbf{x}, \mathbf{y}, t)},$$

$$\sigma'(\mathbf{x}, \mathbf{y}, t) = \sqrt{\sigma_1^2 + \sigma_2^2 + \sigma_3^2 - \sigma_1\sigma_2 - \sigma_2\sigma_3 - \sigma_1\sigma_3}, \tag{42}$$

where S_y is the yield strength and $\sigma_i(\mathbf{x}, \mathbf{y}, t)$ are the principal stresses obtained from the microstresses $\sigma_{ij}^0(\mathbf{x}, \mathbf{y}, t)$. In the case of brittle materials, a modified-Mohr criterion is utilized. The factor of safety using this theory is given as (*e.g.* see (Dowling, 2006))

$$F_s^{brittle}(\mathbf{x}, \mathbf{y}, t) = \frac{S_{ut}}{\tilde{\sigma}(\mathbf{x}, \mathbf{y}, t)}, \quad \tilde{\sigma}(\mathbf{x}, \mathbf{y}, t) = \max\left(C_1, C_2, C_3, \sigma_1, \sigma_2, \sigma_3\right), \tag{43}$$

where C_i are the Dowling coefficients (Dowling, 2006),

$$C_1(\mathbf{x}, \mathbf{y}, t) = \frac{1}{2}\left[|\sigma_1 - \sigma_2| + \frac{|S_{uc}| - 2S_{ut}}{|S_{uc}|}(\sigma_1 + \sigma_2)\right],$$

$$C_2(\mathbf{x}, \mathbf{y}, t) = \frac{1}{2}\left[|\sigma_2 - \sigma_3| + \frac{|S_{uc}| - 2S_{ut}}{|S_{uc}|}(\sigma_2 + \sigma_3)\right], \tag{44}$$

$$C_3(\mathbf{x}, \mathbf{y}, t) = \frac{1}{2}\left[|\sigma_3 - \sigma_1| + \frac{|S_{uc}| - 2S_{ut}}{|S_{uc}|}(\sigma_3 + \sigma_1)\right],$$

and S_{ut} and S_{uc} are the ultimate tensile and compressive strengths of the brittle material, respectively. It should be noted that while the strengths S_y, S_{ut} and S_{uc} may depend on the characteristic length of the microstructural features, the properties used in this work are the bulk material strengths. That said, the microscopic factor of safety over the microstructure $F_s^{micro}(\mathbf{x}, \mathbf{y}, t)$ is defined as

$$F_s^{micro}(\mathbf{x}, \mathbf{y}, t) = \begin{cases} F_s^{ductile}(\mathbf{x}, \mathbf{y}, t) & \text{if } \mathbf{y} \in Y_{ductile} \\ F_s^{brittle}(\mathbf{x}, \mathbf{y}, t) & \text{if } \mathbf{y} \in Y_{brittle} \end{cases}, \tag{45}$$

where $Y_{ductile}$ and $Y_{brittle}$ denote the regions of the microstructure which are composed of ductile or brittle phases, respectively. The macroscopic factor of safety $F_s^{macro}(\mathbf{x}, t)$ is defined as the minimum factor of safety occurring over the RME domain Y, which can be written as

$$F_s^{macro}(\mathbf{x}, t) = \min_{\mathbf{y} \in Y} F_s^{micro}(\mathbf{x}, \mathbf{y}, t). \tag{46}$$

The factor of safety of the entire macroscopic body $F_s(t)$ is simply the minimum of $F_s^{macro}(\mathbf{x}, t)$ occurring in Ω, or in other words,

$$F_s(t) = \min_{\mathbf{x} \in \Omega} F_s^{macro}(\mathbf{x}, t). \tag{47}$$

Lastly, it should be emphasized that the preceding procedures for computing the various factors of safety are conservative. Not only are the bulk strengths used even in cases where the microstructural morphology length scales may be small enough to warrant the use of strength parameters exceeding the bulk values, but morphological intricacies could also give rise to very localized regions of high stress in the RME, and hence, low factors of safety as per the definitions given in (46) and (47). Thus, even at a macroscopic factor of safety $F_s^{macro}(\mathbf{x}, t)$ of 1, it is likely that a majority of the microstructure material is experiencing a stress state which is far from causing failure. Therefore, it is probable that at loads exceeding those which give rise to $F_s^{macro}(\mathbf{x}, t) = 1$, the microstructure would only experience very localized yielding/brittle damage and that the heterogeneous material would continue to carry significantly higher loads. To track the behavior of heterogeneous materials into the nonlinear regime a more complex analysis, for example an elastoplastic multiscale analysis, would have to be undertaken (*e.g.* see (Ghosh *et al.*, 1996; Fish and Yu, 2001; Kamiński and Figiel, 2001; González *et al.*, 2004; Taliercio, 2005)). An analysis of this type, however, is beyond the focus of the present work.

CHAPTER 3

MICROSTRUCTURE CHARACTERIZATION AND HOMOGENIZATION OF MATERIAL PROPERTIES FOR RANDOM HETEROGENEOUS MATERIALS

Figure 2.1 depicts a heterogeneous body that is comprised of two distinct material phases with random microstructure. In this chapter, the response of the material at the microstructural level and the corresponding homogenized properties of the random heterogeneous material are analyzed using representative material elements. The RMEs are of size ℓ, where ℓ is much smaller than the characteristic length L of the heterogeneous body. It is necessary to develop a method to create sample random microstructures for the computational analysis of heterogeneous media. The method presented here is simple to implement and yields realistic morphologies.

3.1 Simulation of Random Heterogeneous Microstructures

The concept of random morphology description functions is used in the present work to help create realistic computational models of random microstructures. In this approach, the morphology of a random two-phase material at the microstructural level is defined through a level-cut of a random field. It is similar to the Gaussian random field method originally proposed by Roberts and Teubner (1995). The approach has been employed by Cao and Liu (2006) for tailoring porous microstructures to obtain prescribed properties.

Consider a representative material element which occupies the domain $Y = [0, \ell] \times [0, \ell]$. A RMDF is any arbitrary function $f(\mathbf{y})$ which is defined over the region Y. The RMDF function in conjunction with a cutoff value f_o is used to define the two-phase microstructure. All locations $\mathbf{y} \in Y$ where $f(\mathbf{y})$ is greater than the cutoff value f_o are assumed to be occupied by material phase 1. Similarly, all regions where $f(\mathbf{y})$ is less than the cutoff value f_o are assumed to be occupied by material phase 2. Thus,

the RMDF $f(\mathbf{y})$ and cutoff value f_o define the microstructural morphology and the $f(\mathbf{y}) = f_o$ isocontour constitutes the interface between the two material phases.

The following RMDF, which is a sum of two-dimensional Gaussian functions, is used to create two-phase random microstructures,

$$f(\mathbf{y}) = \sum_{i=1}^{N} c_i e^{-\left[\frac{\left(y_1 - y_1^{(i)}\right)^2 + \left(y_2 - y_2^{(i)}\right)^2}{w_i^2}\right]}. \tag{48}$$

Here N is the total number of Gaussian functions that are used to define the RMDF. The magnitudes $c_i \in [-1, 1]$ and centers $(y_1^{(i)}, y_2^{(i)}) \in Y$ of the Gaussian functions are randomly chosen. The spatial widths of the individual Gaussian functions, denoted by w_i, are chosen to depend on the number of Gaussian functions in a very specific manner in order to create increasingly complex morphological features as more and more Gaussian functions are included in the RMDF,

$$w_i = \frac{\ell}{\sqrt{N}}. \tag{49}$$

For convenience, the RMDF $f(\mathbf{y})$ and cutoff value f_o are normalized to lie in the range $[0, 1]$ as follows,

$$\bar{f}(\mathbf{y}) = \frac{f(\mathbf{y}) - f_{\min}}{f_{\max} - f_{\min}}, \tag{50}$$

where $f_{\min}$ and $f_{\max}$ are the minimum and maximum values of $f(\mathbf{y})$, respectively, in the RME region Y. As stated previously, the material property $C(\mathbf{y})$ at a location within the base cell is defined as

$$C(\mathbf{y}) = \begin{cases} C^{(1)} & \text{if} \quad \bar{f}(\mathbf{y}) > \bar{f}_o \\ C^{(2)} & \text{if} \quad \bar{f}(\mathbf{y}) < \bar{f}_o \end{cases}, \tag{51}$$

where $C^{(i)}$ denotes the material property of phase i and $\bar{f}_o$ is the normalized cutoff value. The volume fraction V_1 of the first material phase is computed from the formula

$$V_1 = \frac{1}{|Y|} \int_Y \mathcal{H}\left(\bar{f}(\mathbf{y}) - \bar{f}_o\right) \, dY, \tag{52}$$

where $\mathcal{H}(\cdot)$ is the Heaviside step function. Choosing $\bar{f}_o = 0$ yields a volume fraction $V_1 = 1$ and conversely choosing $\bar{f}_o = 1$ gives $V_1 = 0$. Note that the sum of the phase volume fractions has to equal 1, $i.e.$, $V_1 + V_2 = 1$, since there are no voids present in the microstructure.

As previously noted, the complexity of the morphological features increases as the number of Gaussian functions N is increased. It is recommended that N be at least as large as 50 to obtain sufficiently complex random microstructures. Since the AEH method presented in the next section is based on the assumption of locally periodic media, the Gaussian functions are 'tiled' about the cell domain Y to create a locally periodic microstructure with continuous material interfaces across cell boundaries. This is implemented by introducing Gaussian sources of equal magnitude c_i at locations $(y_1^{(i)} + k_1\ell, y_2^{(i)} + k_2\ell)$ where k_1 and k_2 are integers that can take on values of either $-1,0$ or 1. This results in a spatially periodic RMDF in the neighborhood of the base cell Y. The corresponding minimum and maximum values $f_{\min}$ and $f_{\max}$ are evaluated over the cell domain Y and random microstructures of varying phase volume fractions are generated by varying the cutoff value $\bar{f}_o$. The microstructures thus created are periodic with no discontinuities in the the material interfaces across cell boundaries when they are 'tiled'. It is important to note, however, that phase boundaries that closely coincide with the RME boundary do occasionally occur thus creating a microstructure which at a glance may not appear to be periodic. Upon closer inspection, though, all microstructures created via this method are easily verified as being periodic.

A sample realization of a RMDF over the domain Y is depicted in Figure 3.1 for a specific choice of random parameters c_i, $y_1^{(i)}$ and $y_2^{(i)}$ for $N = 800$. The volume fraction V_1, which is obtained using equation (52), is shown in Figure 3.2 as a function of the cutoff value $\bar{f}_o$ for the RMDF depicted in Figure 3.1. It is observed that the volume fraction has a nonlinear dependence on the cutoff value and the shape
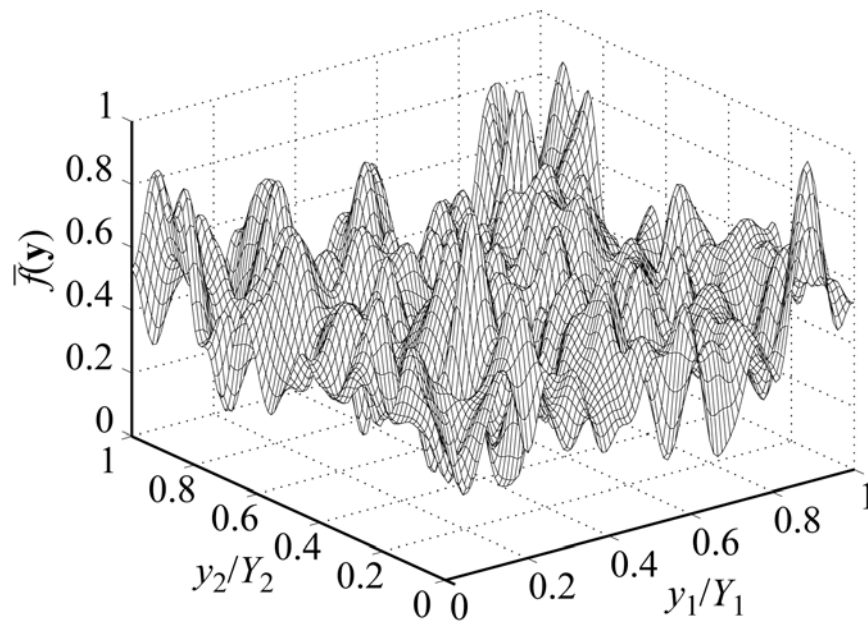
Figure 3.1. Sample RMDF with $N = 800$.
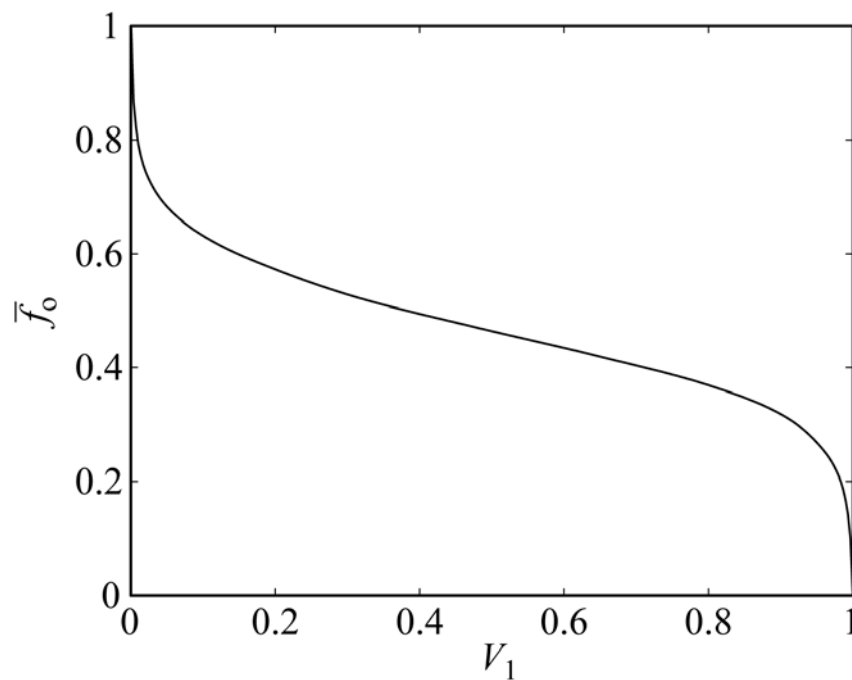
Figure 3.2. Volume fraction vs. cutoff value for sample RMDF with $N = 800$.
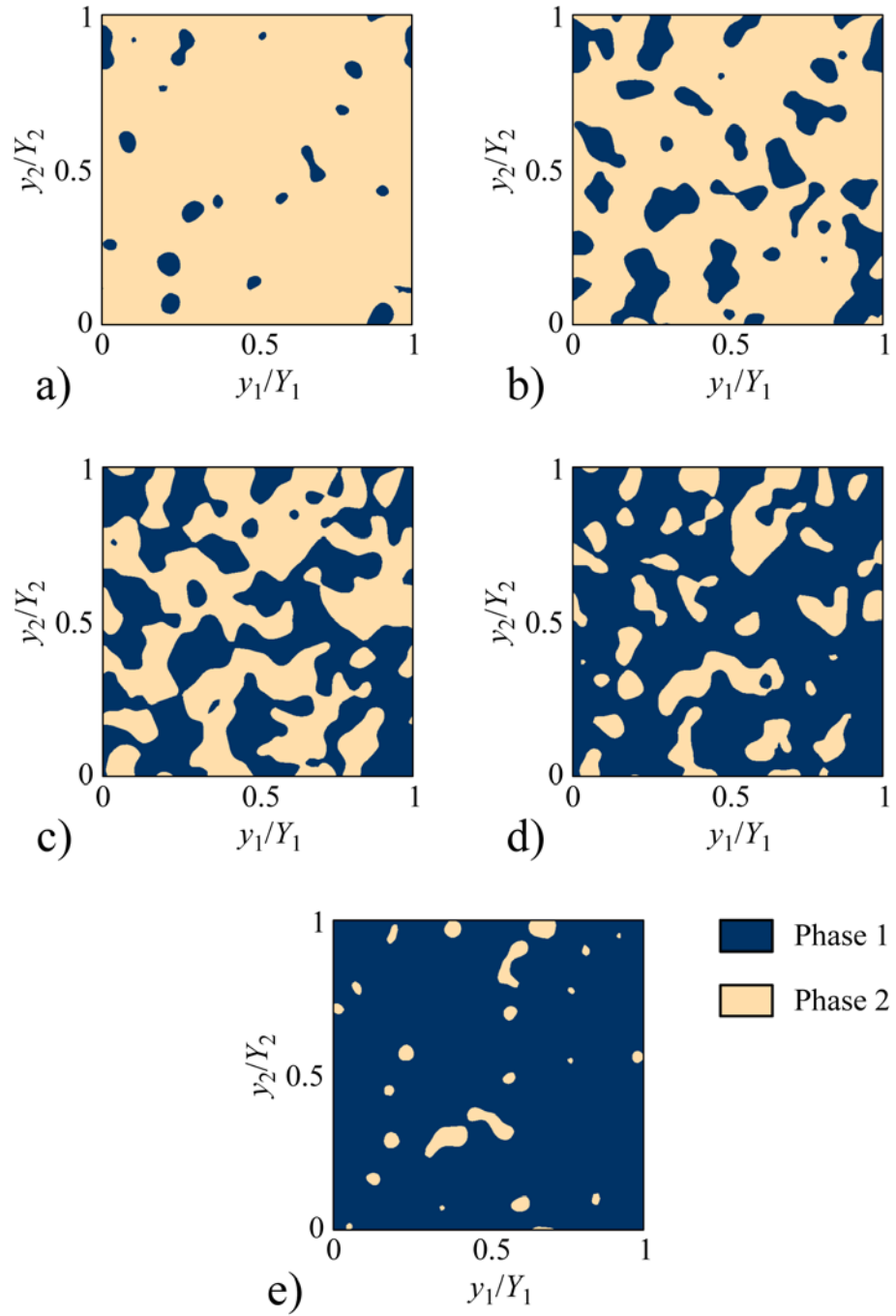
Figure 3.3. Sample RMDF microstructures with $N = 800$. Volume fractions shown are a) $V_1 = 0.05$, b) 0.25, c) 0.5, d) 0.75 and e) 0.95.

of the curve depends on the choice of RMDF. Nevertheless, it is possible to create a random microstructure with a desired volume fraction by choosing an appropriate value for the cutoff value $\bar{f}_o$. Microstructural morphologies corresponding to the RMDF in Figure 3.1 are shown in Figure 3.3 for several different volume fractions. When the volume fraction of one material phase is much smaller than the other, the resulting microstructure is one in which irregularly shaped particles of the phase are embedded in a matrix of the other material phase (Figures 3.3(a),(b),(d), and (e)). In comparison, when the volume fractions of the constituent phases are nearly equal, an interpenetrating/skeletal microstructure with no clearly defined matrix and particulate phases is obtained (Figure 3.3(c)) (Wegner and Gibson, 2000/2001).

Actual micrographs of Al/Al_2O_3 and W/Cu random composite materials fabricated using typical manufacturing techniques are shown next to sample RMDF microstructures in Figure 3.4 (Cheng *et al.*, 2006; del Rio *et al.*, 2007). The number of Gaussian functions, N, are chosen such that the resulting RMDF microstructures have the same characteristic length scale as the micrographs (see Section 3.2.1). It can be seen that the morphological features of the computer generated RMDF microstructures compare well with the actual micrographs of random composite materials. It should be noted that the intent here is not to reconstruct the actual microstructures but to create microstructures that are qualitatively similar to actual micrographs.

3.2 Microstructural Characterization of Random Microstructures

The proposed RMDF methodology is capable of generating a broad range of microstructures that compare well with actual micrographs. In this section, common statistical techniques such as the n-point probability functions and cluster functions are utilized to characterize the simulated microstructures. For purposes of the statistical analysis, we define an ensemble as the collection of all possible realizations of random microstructures generated by the RMDF method. It should be noted that

37
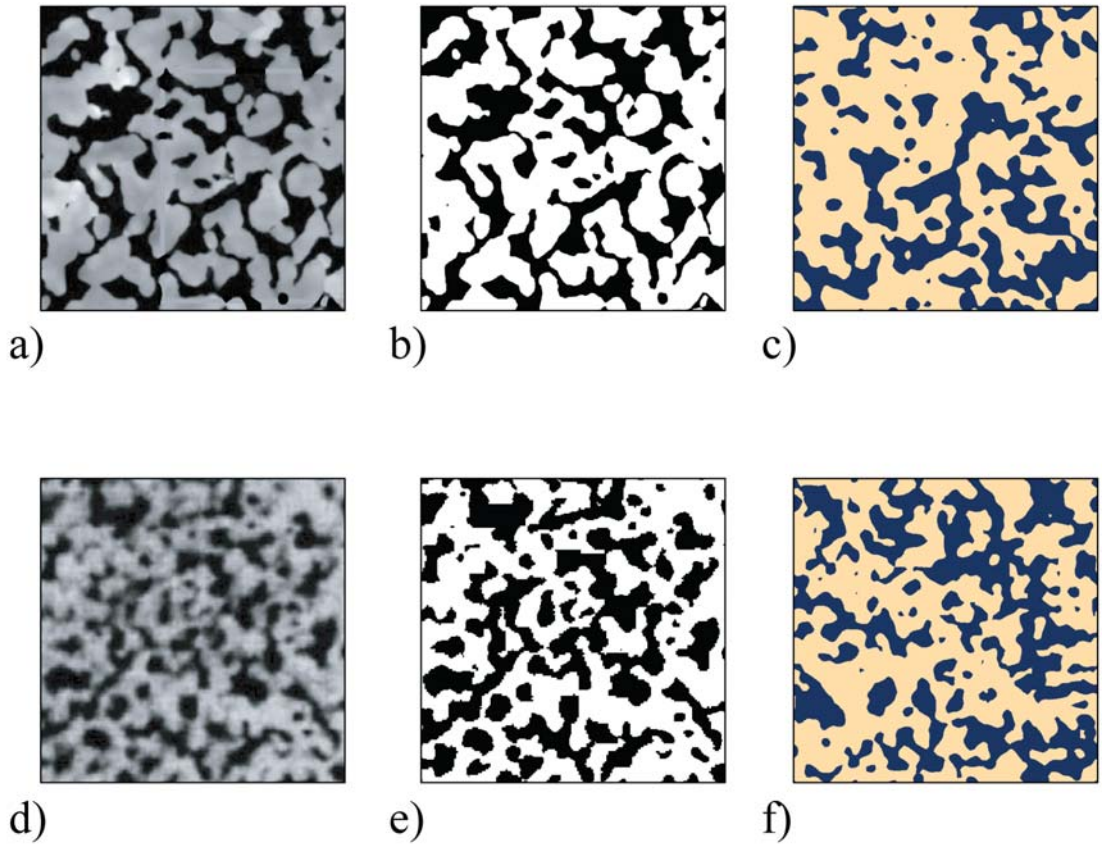
Figure 3.4. Comparison of actual micrographs and simulated RMDF microstructures. Shown are a) actual Al/Al_2O_3 micrograph (del Rio *et al.*, 2007), b) black and white image of actual Al/Al_2O_3 micrograph with c) sample $N = 1,832$ simulated RMDF microstructure and e) actual W/Cu micrograph (Cheng *et al.*, 2006), e) black and white image of W/Cu micrograph with f) sample $N = 2,605$ microstructure

microstructures obtained by simply translating an RMDF in the $y_1 - y_2$ plane are also considered to be distinct realizations.

3.2.1 n-Point Probability Functions

We begin by defining an indicator function $\mathcal{I}^{(i)}(\mathbf{y})$ which is either 1 or 0 depending on whether $\mathbf{y}$ is a location of phase i material or not, respectively. With the indicator function defined and noting that $\mathcal{P}\{\cdot\}$ is the probability of the argument being true, it is possible to define an n-point probability function (Torquato and Stell, 1982)

$$S_n^{(i)}(\mathbf{y}_1, \mathbf{y}_2, \ldots, \mathbf{y}_n) = \mathcal{P}\left\{\mathcal{I}^{(i)}(\mathbf{y}_1) = 1, \mathcal{I}^{(i)}(\mathbf{y}_2) = 1, \ldots, \mathcal{I}^{(i)}(\mathbf{y}_n) = 1\right\}. \qquad (53)$$

That is, $S_n^{(i)}$ is the probability that n points at positions $\mathbf{y}_1, \mathbf{y}_2, \ldots, \mathbf{y}_n$ are located in phase i. It should be noted that the one-point probability function $S_1^{(i)}$, which is simply the volume fraction for phase i, provides only limited insight into the nature of the microstructure. Instead, we choose to focus on the two-point probability $S_2^{(i)}$ since it provides ample information about the microstructure.

The microstructures generated using the RMDF method are found to be statistically homogeneous. That is, there is no preferred origin in the system and the n-point probability functions depends on the relative positions, not on absolute positions, of points $\mathbf{y}_1, \mathbf{y}_2, \ldots, \mathbf{y}_n$. For statistically homogeneous media, the two-point probability functions can be written as

$$S_2^{(i)}(\mathbf{y}_1, \mathbf{y}_2) = S_2^{(i)}(\mathbf{p}) = \mathcal{P}\left\{\mathcal{I}^{(i)}(\mathbf{p}) = 1\right\}, \qquad (54)$$

where $\mathbf{p} = \mathbf{y}_2 - \mathbf{y}_1$. For computational purposes, the two-point probability function is typically expressed as a function of the radial distance and orientation of the relative position vector as $S_2^{(i)}(\mathbf{p}) = S_2^{(i)}(r, \theta)$, where $r = |\mathbf{p}|$ and $\theta = \tan^{-1}(p_2/p_1)$. A technique that was originally proposed by Smith and Torquato (1988) is used to calculate the two-point probability function. For each realization, a sampling template with a random origin is laid down on the random media. The circular template, which is constructed to have many divisions in r and θ, contains many line segments of different lengths and orientations which enable the calculation of the two-point probability function. The phase information is recorded at each sampling point on the template. The process is repeated many times for a particular microstructure realization, each time the template having a new random origin. In addition, the procedure is repeated over a large number of realizations of the random media with the same volume fractions and the results averaged to obtain the trends of $S_2^{(i)}$ as a

function of both r and θ. Numerical results indicate that the two-point probability function $S_2^{(i)}(r, \theta)$ are independent of the orientation θ, which implies that the RMDF microstructures are statistically isotropic. This behavior can be attributed to the nature of the Gaussian functions in the RMDF, which are functions of only r, not θ.

The two-point probability function $S_2^{(1)}(r)$ is shown in Figure 3.5(a) as a function of the normalized radial coordinate r/ℓ for RMDF microstructures with $N = 800$. The results are generated using $1,000$ realizations, each realization having $10,000$ randomly located sampling grids with the data averaged over all angles. It is also worth noting that when $r = 0$, $\mathbf{y}_1$ and $\mathbf{y}_2$ coincide and the two-point probability function is equal to the one-point probability function, which in turn is equal to the volume fraction V_1. As r increases, $S_2^{(1)}(r)$ asymptotically approach V_1^2. For the microstructures created using the RMDF method, the number of Gaussian functions N has a significant effect on the rate of decrease of the two-point probability function curves as shown in Figure 3.5(b). As the number of Gaussian sources in the RMDF is increased, the $S_2^{(1)}(r)$ curve approaches the asymptotic value of V_1^2 more rapidly. A variety of length scales can be associated with a random microstructure (Torquato, 2002). In this work we use the following definition that was originally proposed by Prager (1961) to define a characteristic length scale ℓ_S for the quantitative comparison of microstructural features,

$$\ell_S = \left\{ \int\limits_0^\infty r \left[S_2^{(1)}(r) - V_1^2 \right] \, dr \right\}^{1/2}. \tag{55}$$

The characteristic lengths obtained numerically are 0.0306ℓ, 0.0153ℓ and 0.00765ℓ for $N = 200$, 800 and $3,200$, respectively, for RMDF microstructures with $V_1 = 0.5$. The numerical results indicate that a quadrupling of the number of the sources in the RMDF results in the characteristic length being halved. In addition, the characteristic length also depends on the volume fraction of the constituent phases. Accordingly, the characteristic length ℓ_S can be approximated by the nondimensional equation
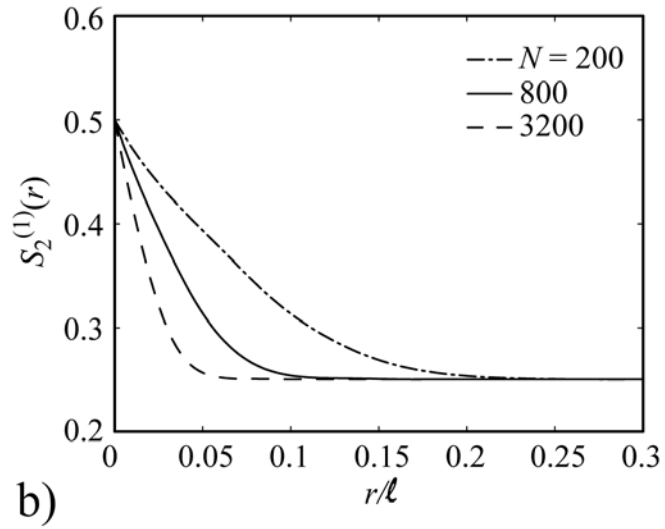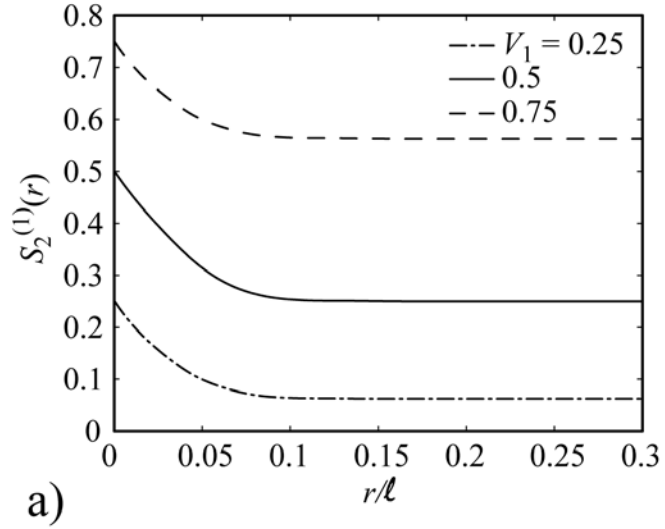
Figure 3.5.   The two-point probability function $S_2^{(1)}(r)$ for RMDF Microstructures as a function of r. Displayed are plots for a) different volume fractions V_1 with the number of Gaussian sources $N = 800$ and b) different numbers of Gaussian sources with volume fraction $V_1 = 0.5$
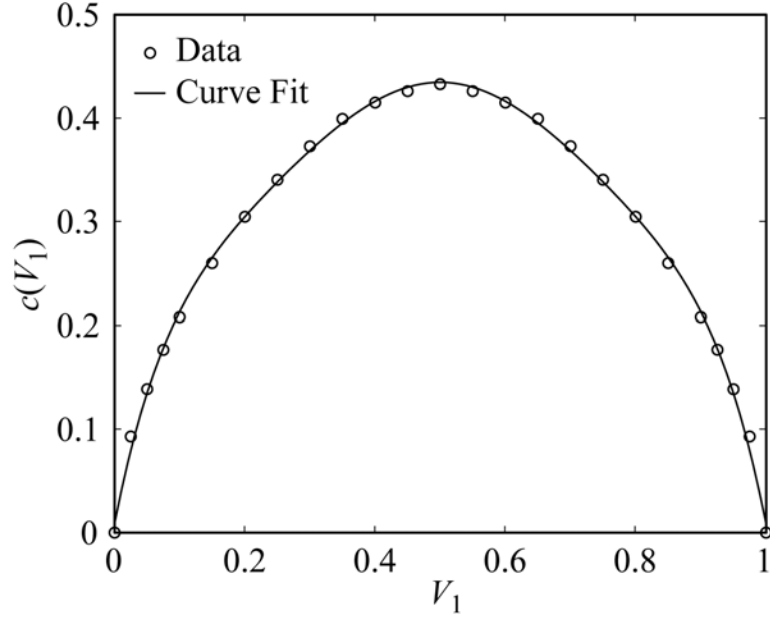
Figure 3.6. Normalized coefficient $c(V_1)$ for the determination of the characteristic length as a function V_1 for RMDF microstructures with $N = 800$.

$$\frac{\ell_S}{\ell} = \frac{c(V_1)}{\sqrt{N}}, \tag{56}$$

where the numerically obtained values for the coefficient $c(V_1)$ are plotted as a function of the volume fraction in Figure 3.6. A polynomial curve fit for $c(V_1)$ yields the following expression,

$$c(V_1) = 0.435 - 1.914 \left(V_1 - \frac{1}{2}\right)^2 + 7.694 \left(V_1 - \frac{1}{2}\right)^4 - 27.395 \left(V_1 - \frac{1}{2}\right)^6. \tag{57}$$

RMDF microstructures are shown in Figure 3.7(a) for three different choices of N, namely 200, 800 and 3,200. It is evident from the figure that as the number of Gaussian sources is increased, the complexity of the morphology increases and the characteristic feature size decreases, which is consistent with equation (56). Figure 3.7(b) demonstrates that as the size of the RME is enlarged in proportion to $\sqrt{N}$, the characteristic length remains visibly unchanged. In other words, increasing the number of Gaussian sources is equivalent to considering a larger volume of a random material with fixed characteristic length.
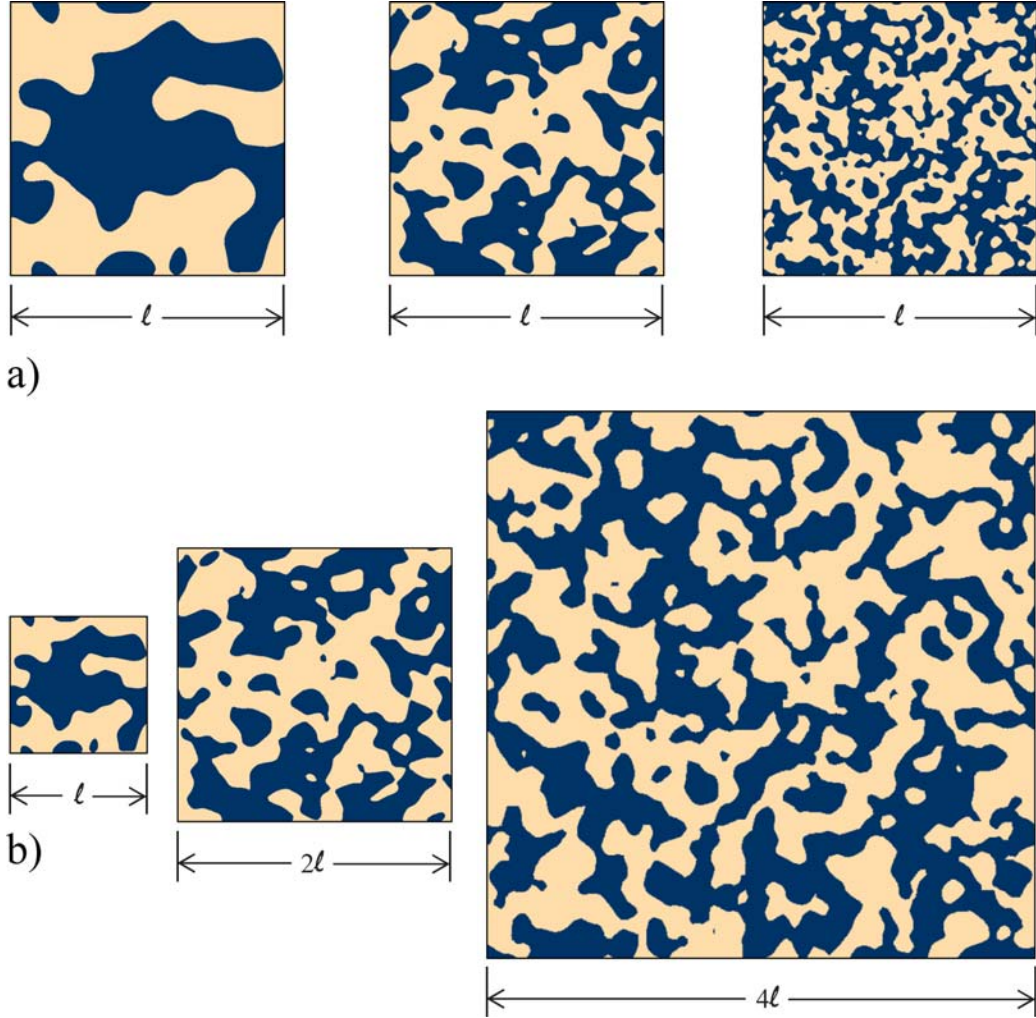
Figure 3.7. Sample RMDF microstructures for $V_1 = 0.5$ and $N = 200$, 800 and $3,200$. Shown are a) microstructures with ℓ fixed and b) the same microstructures with RME sizes increasing in proportion to $\sqrt{N}$.

It should be noted that the number of Gaussian functions N chosen to create the simulated microstructures shown earlier in Figures 3.4(c) and 3.4(f) are determined using the methods described in this section. First, the $S_2^{(1)}(r)$ curves and the corresponding characteristic length ℓ_S of the actual micrographs were created using the template method of Smith and Torquato (1988) and (55). The volume fractions of the constituent phases are determined from the black and white images of the micrographs in Figures 3.4(b) and 3.4(e). Subsequently, the curve fit (57) and (56) are used to

43
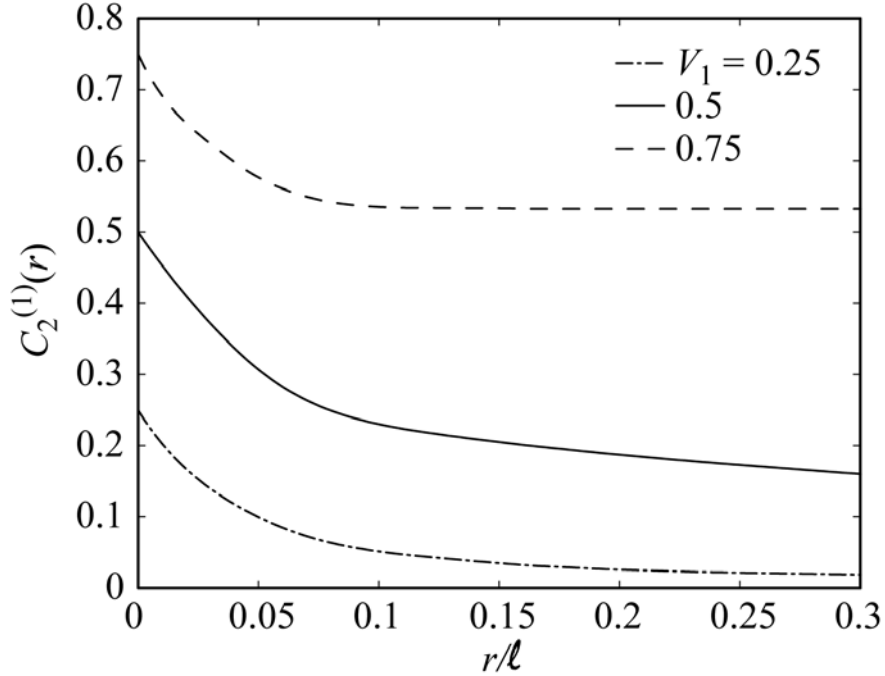
Figure 3.8. The two-point cluster function $C_2^{(1)}(r)$ as a function of r for RMDF microstructures for three different volume fractions.

determine the appropriate number of Gaussian sources N to match the characteristic length of the actual and RMDF micrographs.

3.2.2 Cluster-Type Functions

The phase connectivity of the random microstructure can be characterized using the n-point cluster function, $C_n^{(i)}(\mathbf{y}_1, \mathbf{y}_2, \ldots, \mathbf{y}_n)$ (Lee and Torquato, 1989). The n-point cluster function is similar to the n-point probability function with the exception that it measures the probability of the locations $\mathbf{y}_1, \mathbf{y}_2, \ldots, \mathbf{y}_n$ not only belonging to the same phase i, but also belonging to the same cluster. As for its computation, the procedure is nearly identical to that for computing $S_n^{(i)}$ with the only difference being that one must ensure that the points in question lie within the same cluster. Similar to the case for the n-point probability function, we focus solely on the two-point cluster function $C_2^{(i)}(r)$. The two-point cluster function for phase 1 which is denoted by $C_2^{(1)}(r) = C_2^{(1)}(\mathbf{y}_1, \mathbf{y}_2)$ is plotted as a function of $r = |\mathbf{y}_2 - \mathbf{y}_1|$ in Figure 3.8

44

for three different volume fractions. As was the case for the two-point probability function $S_2(r)$, the two-point cluster function $C_2(r)$ is also equal to V_1 when $r = 0$, as expected. However, unlike S_2, the two-point cluster function does not asymptotically approach the square of the volume fraction for large r. As shown in Figure 3.8, the function C_2 continues to decrease and asymptotically approach zero for large values of r when $V_1 \leq 0.5$. In the case of microstructures with volume fraction $V_1 > 0.5$, the two-point cluster function curve approaches a non-zero asymptotic value. This behavior can be explained as follows using the concept of percolation.

When the volume fraction V_1 is small, the topology of the microstructure corresponds to particles of material phase 1 embedded in a matrix of material phase 2. As the volume fraction V_1 increases, the size of the particles also increase until at some critical point the particles become interconnected and material phase 1 becomes the matrix phase. This point where the particulate phase transitions from a particulate to matrix role, or in other words when the average cluster size of a certain phase becomes infinite, is the point of percolation. The normalized cluster size S^* for a specific realization is defined as S/ℓ^2 where S is the cluster size. A common method for determining percolation is by plotting the ensemble average $\langle 1/S^* \rangle$ versus the volume fraction V_1 as shown in Figure 3.9. The average cluster size reported here is obtained by averaging over $1,000$ microstructural realizations with fixed volume fraction. As can be seen in the figure, $\langle 1/S^* \rangle$ approaches zero at $V_1 = 0.5$. Thus, the average cluster size approaches infinity when the phase volume fractions are equal. That is, percolation occurs at $V_1 = 0.5$ on average. It should be noted that, for a specific RMDF microstructure, percolation need not occur exactly at $V_1 = 0.5$ since the volume fraction at which percolation occurs would depend on the morphology of the selected microstructure.
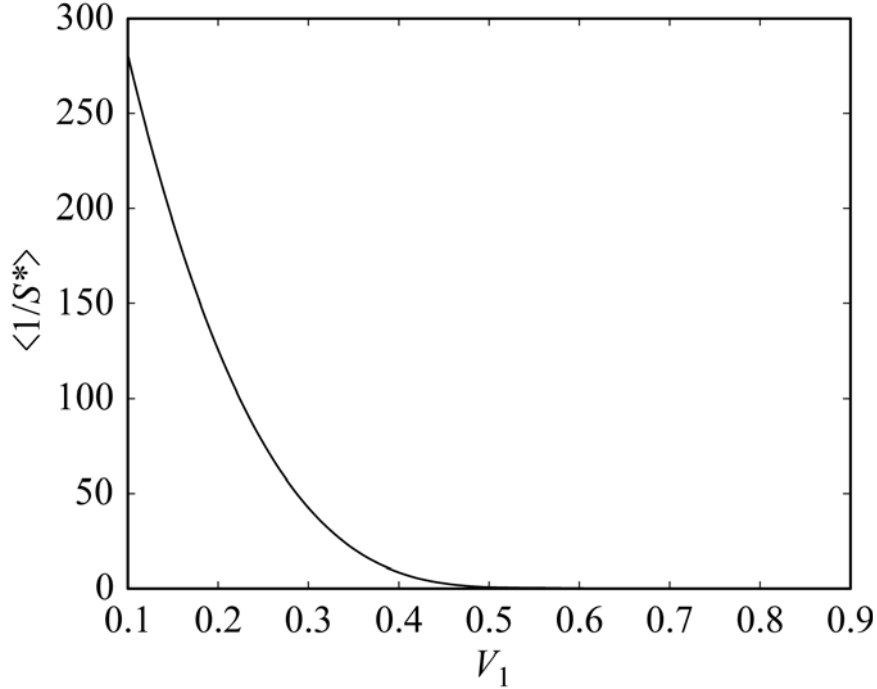
Figure 3.9. Average of the reciprocal cluster size as a function of the volume fraction V_1 for RMDF microstructures with $N = 800$.

3.3 Results for the Homogenized Material Properties of Random Heterogeneous Materials

In this section, the homogenized material properties are presented for random heterogeneous materials and the results compared with the Hashin-Shtrikman bounds and self-consistent estimates. In addition, the homogenized material properties are compared with experimental data reported in the literature for three different random heterogeneous materials including one high-contrast material combination with a large disparity in constituent properties.

Prior to providing numerical results for the homogenized material properties, it is necessary to establish the convergence characteristics of the finite element solution. Of particular interest here is the accuracy of the homogenized material properties. The convergence of the homogenized material properties is investigated for aluminum/alumina (Al/Al$_2$O$_3$) random heterogeneous materials with microstructures

46

Material Property	Al	Al$_2$O$_3$	W	Cu	Mullite	Mo	Ni	SS	Resin
κ (W/m°C)	233	30.0	172.1	377.7	5.2	139	–	–	–
E (GPa)	70.0	393.0	397.8	128.2	–	–	207	193.8	1.31
ν	0.3	0.22	0.297	0.338	–	–	0.31	0.29	0.4
α (10^{-6}/°C)	23.4	7.6	3.94	15.74	–	–	–	–	–

Table 3.1. Properties of selected materials considered in the present chapter.

similar to that shown in Figure 3.4(a)-(c) (del Rio *et al.*, 2007). The material properties of Al and Al$_2$O$_3$ are listed in Table 3.1. This particular material combination is chosen since it exhibits a moderately high contrast ratio of 7.8 for the thermal conductivity, 5.6 for the Young's modulus and 3.2 for the thermal expansion coefficient. The sample microstructure shown in Figure 3.10(a) is chosen for the convergence study. This particular RMDF microstructure was generated using $N = 800$ terms and it has an aluminum volume fraction of $V_{\text{Al}} = 0.5$. The finite element mesh, which consists of six-noded triangular elements, is designed to conform to the true microstructural topology as is evident from the representative mesh shown in Figure 3.10(b). The convergence of the finite element results is investigated by varying the number of elements. The convergence of the homogenized thermal conductivity κ_1^H, Young's modulus E_1^H, shear modulus μ_{12}^H and thermal expansion coefficient α_1^H are shown in Figure 3.11 as the number of elements N_e is increased. It is found that all the homogenized material properties are within 2.2% of the converged material properties when $\sqrt{N_e/N} = 2.0$. In other words, it is sufficient to use $N_e = 3,200$ elements for RMDF microstructures generated using $N = 800$ Gaussian functions. Beyond this level of mesh refinement, there is very little change in the computed homogenized properties. To ensure good accuracy, the homogenized results presented below are computed using a finite element mesh of no less than $3,200$ elements, with the actual number being somewhat higher depending on the intricacy of the microstructure.

RME

a)

b)
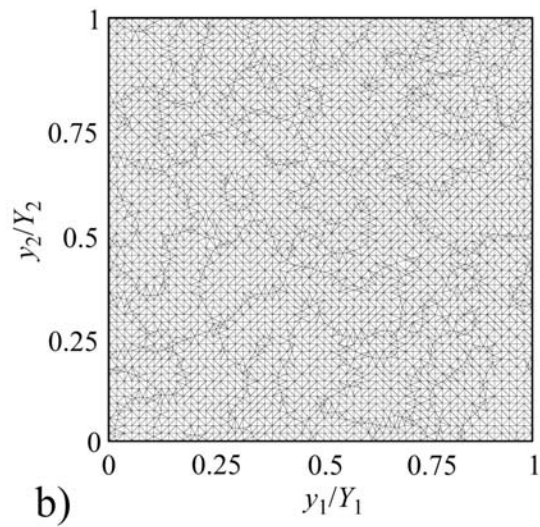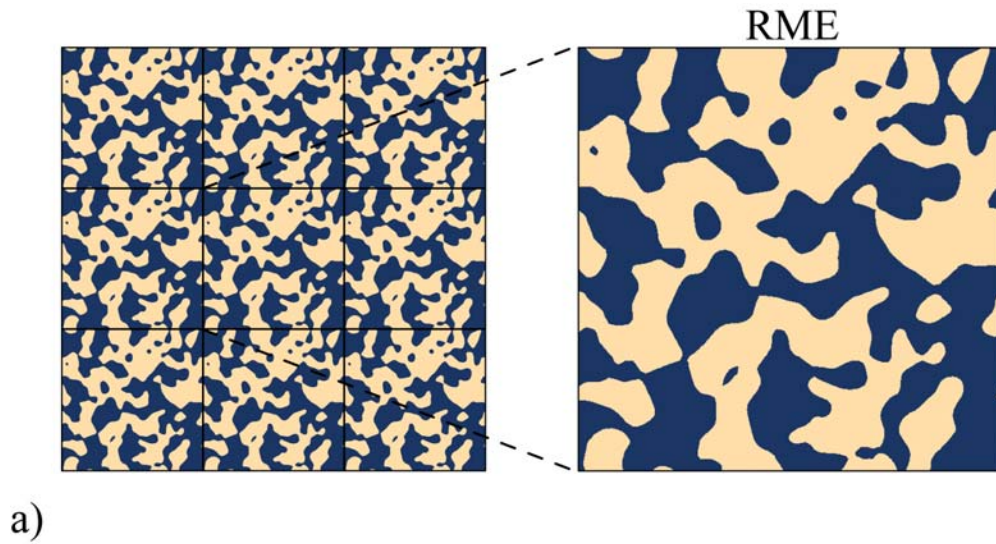
Figure 3.10. Tiled representative material element (RME) for a $N = 800$, $V_1 = 0.5$ microstructure. Shown are a) tiled RME and b) sample finite element mesh.
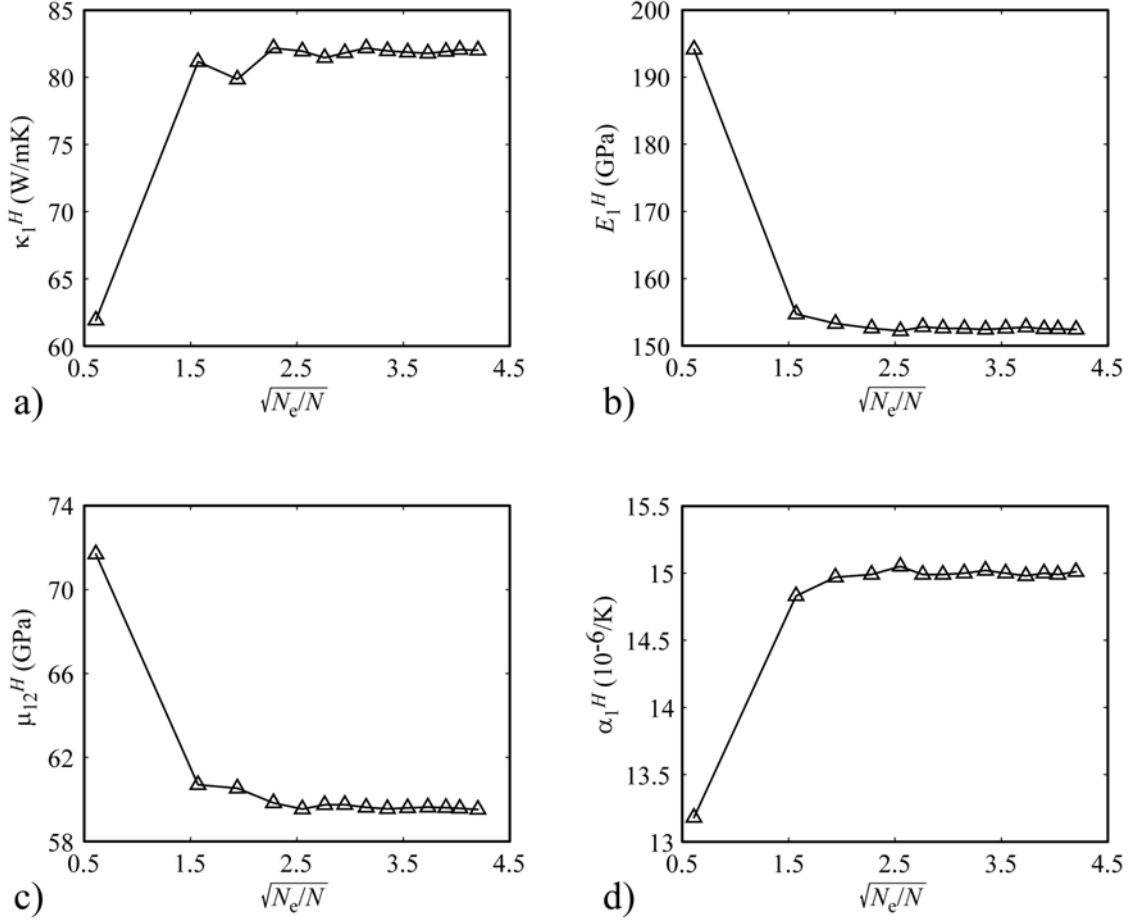
Figure 3.11. Convergence of material properties with mesh refinement for representative Al/Al$_2$O$_3$ RMDF microstructures with $N = 800$.

The homogenized properties of random microstructures will in general depend on the size of the chosen representative material element. In general, the RME should be large enough to contain a sampling of the different microstructural features that can occur for a given volume fraction. That is, the size ℓ of the RME relative to the characteristic length scale ℓ_S should be sufficiently large. There will be significant variation in the homogenized properties between different representative material elements if the ratio of ℓ/ℓ_S is small. It is evident from (56) that the ratio ℓ/ℓ_S can be increased by increasing the number of terms N in the RMDF. The variation of the homogenized material properties is investigated by analyzing a large number of different RMEs. The ensemble average of $1,000$ distinct RMEs is plotted in Figure 3.12.
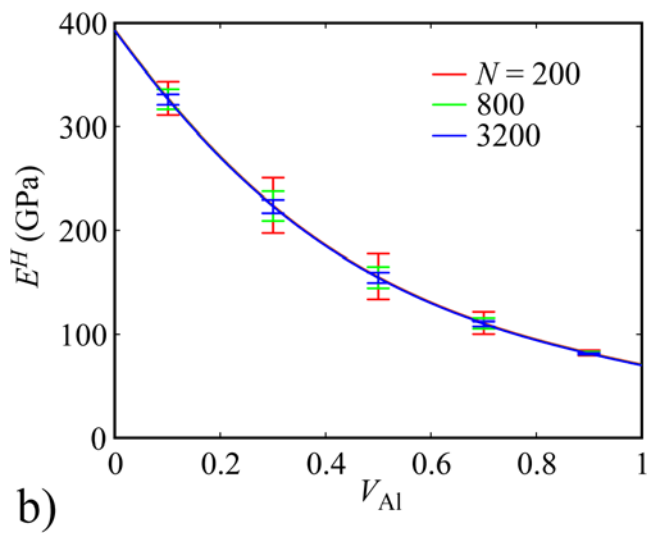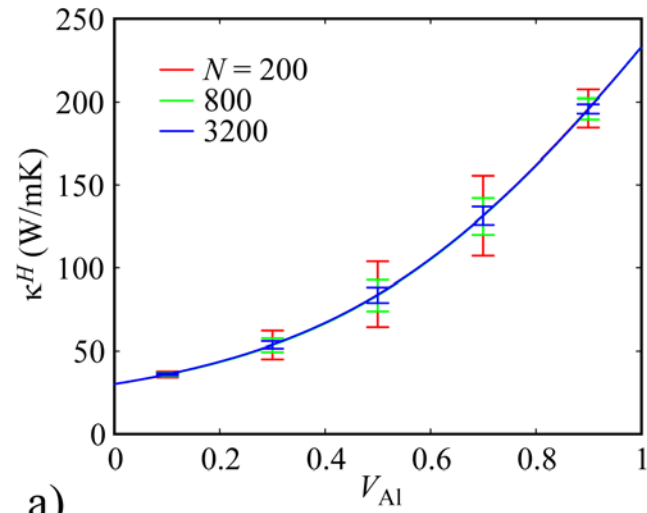
Figure 3.12. Comparison of homogenized material properties for different numbers of sources N for Al/Al$_2$O$_3$ random heterogeneous media with error bars of plus or minus three standard deviations. Shown are a) thermal conductivity and b) Young's modulus.

For all ensemble averages shown, an error bar denoting plus/minus three standard deviations is also presented. In other words, 99.73% of the random microstructures have homogenized properties that lie within the error bars. It is observed that the standard deviation for the homogenized material properties decreases as the number of terms N, and as a consequence the ratio ℓ/ℓ_S, increases. As expected, increasing the size of the RME relative to the characteristic length of the microstructural features leads to a better estimation of the material properties, $i.e.$ smaller variation in homogenized properties from one sample to another. Interestingly enough, the averaged material properties are the same for $N = 200, 800$ and $3,200$. Stated differently, the ensemble average of the homogenized material properties are independent of the size of the RME relative to its characteristic length. Thus, the homogenized material properties of a heterogeneous material can be computed accurately by averaging over a large number of small RMEs. This is computationally more efficient than performing a single finite element analysis of a very large RME, a process which can take a great deal of computational time.

The homogenized material properties are compared with the Hashin-Shtrikman bounds (Hashin and Rosen, 1964; Hill, 1964; Hashin, 1965; Rosen and Hashin, 1970; Hashin, 1979) and the self-consistent estimate (Hill, 1965) for transversely isotropic materials. The homogenized material properties for Al/Al_2O_3 are plotted in Figure 3.13 as a function of the volume fraction V_{Al} along with the corresponding Hashin-Shtrikman bounds and the self-consistent estimate. It is observed that, for this particular material combination, the homogenized material properties lie within the Hashin-Shtrikman bounds and are nearly identical to those obtained by the self-consistent scheme. The thermal conductivity κ^H predicted by the self-consistent method is off by less than 1.51% of the homogenized material properties for the entire range of volume fractions. As was the case for the thermal conductivity, the other homogenized properties also closely follow the self-consistent estimate with the maximum errors in the Young's
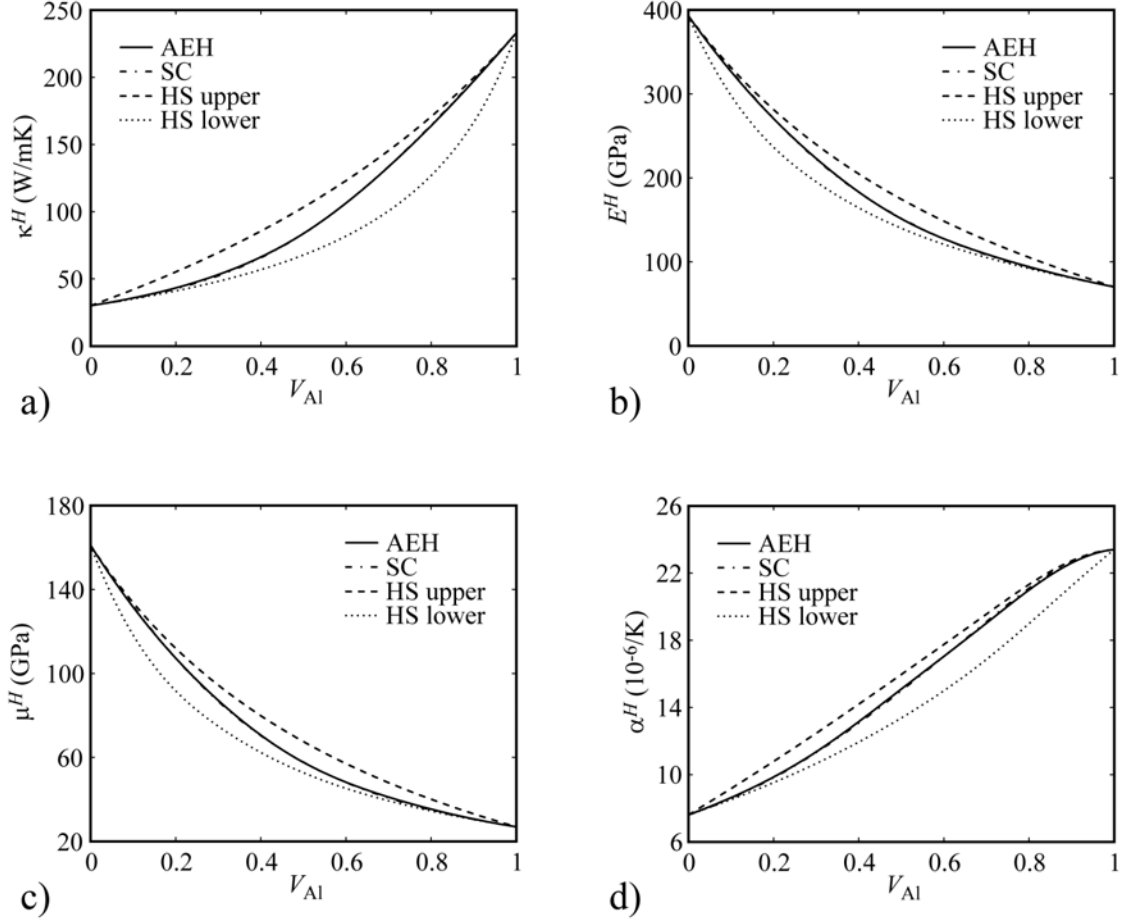
Figure 3.13. Comparison of Hashin-Shtrikman bounds, self-consistent estimate and obtained effective property results as a function of volume fraction for Al/Al$_2$O$_3$ random heterogeneous media. Results are shown for a) thermal conductivity, b) Young's modulus, c) shear modulus and d) thermal expansion coefficient.

modulus E^H, the shear modulus μ^H and the thermal expansion coefficient α^H being 0.86%, 1.16%, and 0.70%, respectively. We also consider a tungsten/copper (W/Cu) random heterogeneous material with microstructures similar to those shown in Figure 3.4(d)-(f) (Cheng *et al.*, 2006). The material properties of W and Cu are listed in Table 3.1. As is evident from Figure 3.14, the self-consistent and AEH material properties are in good agreement for the entire range of volume fractions. It is important to note that the close correlation between the homogenized material properties and the self-consistent estimate observed for these specific material combinations need
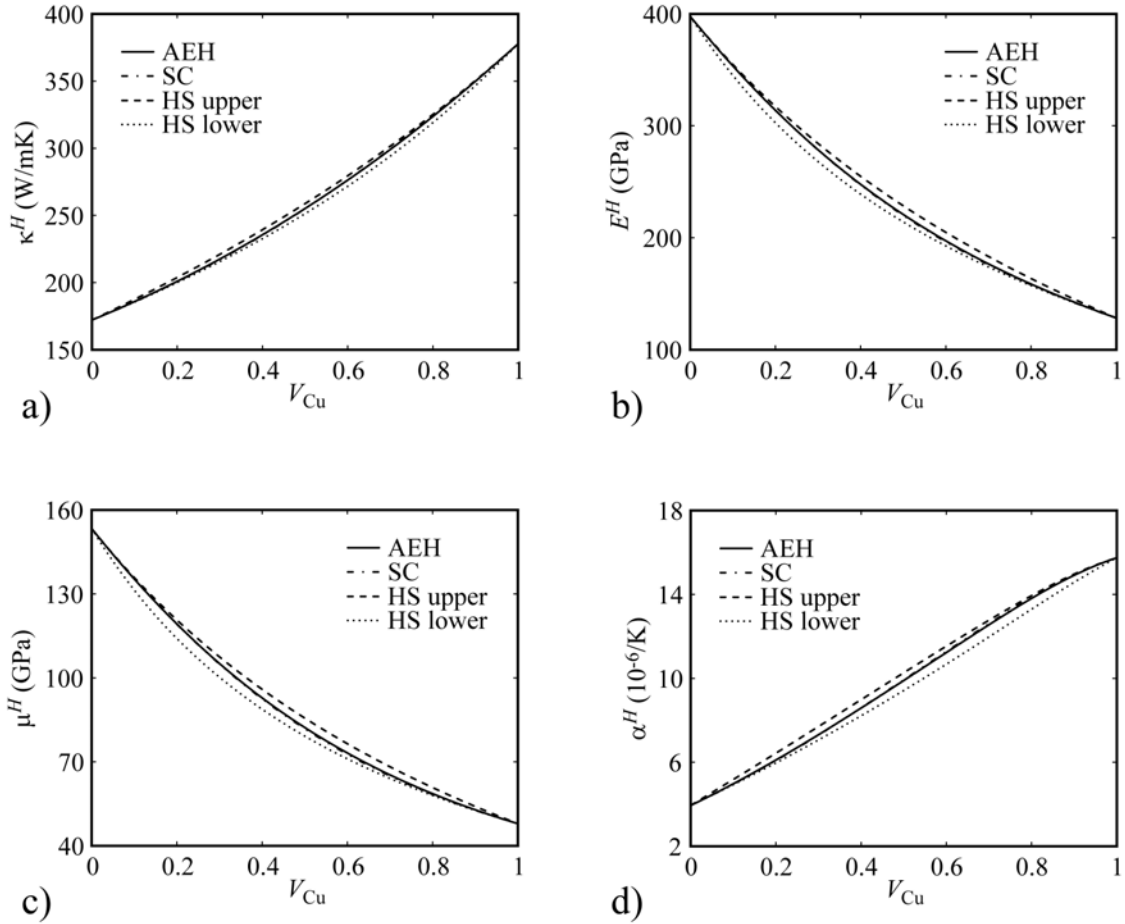
Figure 3.14. Comparison of Hashin-Shtrikman bounds, self-consistent estimate and obtained effective property results as a function of volume fraction for W/Cu random heterogeneous media. Results shown for a) thermal conductivity, b) Young's modulus, c) shear modulus and d) thermal expansion.

not necessarily hold true for other material combinations. Further study is necessary to quantify the correlation between the AEH and self-consistent estimates for high contrast materials.

The homogenized thermal conductivity is compared with experimental results for an actual Mullite/Mo random heterogeneous material with constituent properties listed in Table 3.1. Sample micrographs of the Mullite/Mo random material are shown in Figures 3.15(a)-(c) (Jin *et al.*, 2005). The homogenized and experimentally obtained thermal conductivity are compared in Figure 3.15(d) for a range of volume fractions.

53
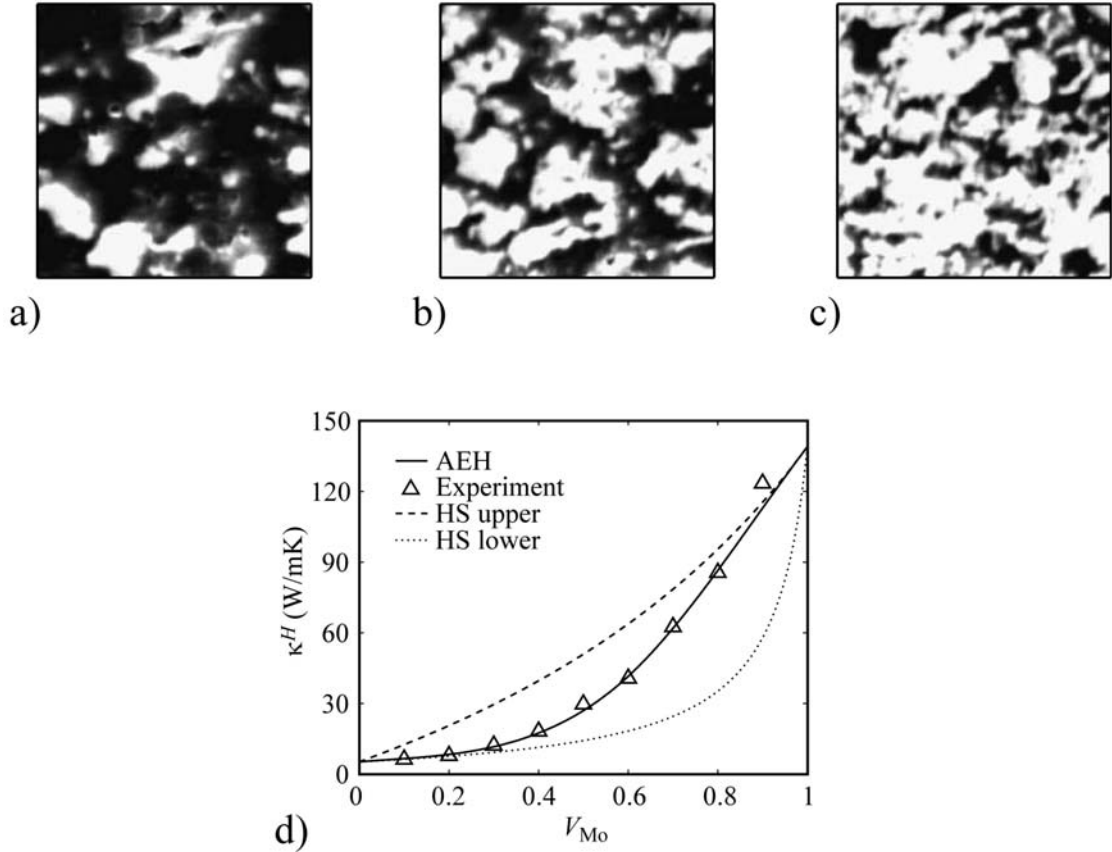
Figure 3.15. Actual Mullite/Mo micrographs (Jin *et al.*, 2005) and comparison of predicted and actual thermal conductivities. Volume fractions shown are a) V_{Mo} = 0.2, b) V_{Mo} = 0.4 and c) V_{Mo} = 0.6 with comparison of thermal conductivity predictions for RMDF microstructures, estimates and experimental values shown in d).

It is observed that the computed homogenized thermal conductivity matches the experimental data very well with the exception of the microstructure corresponding to V_{Mo} = 0.9. Next, the homogenized Young's modulus is compared with experimental data for Ni/Al$_2$O$_3$ random heterogeneous materials (Aldrich *et al.*, 2000). The constituent material properties of Ni/Al$_2$O$_3$ are listed in Table 3.1. Representative micrographs of Ni/Al$_2$O$_3$, shown in Figures 3.16(a)-(c), exhibit a great deal of randomness. The homogenized material properties shown in Figure 3.16(d) compare fairly well with experimental results for the most part except for certain intermediate

54
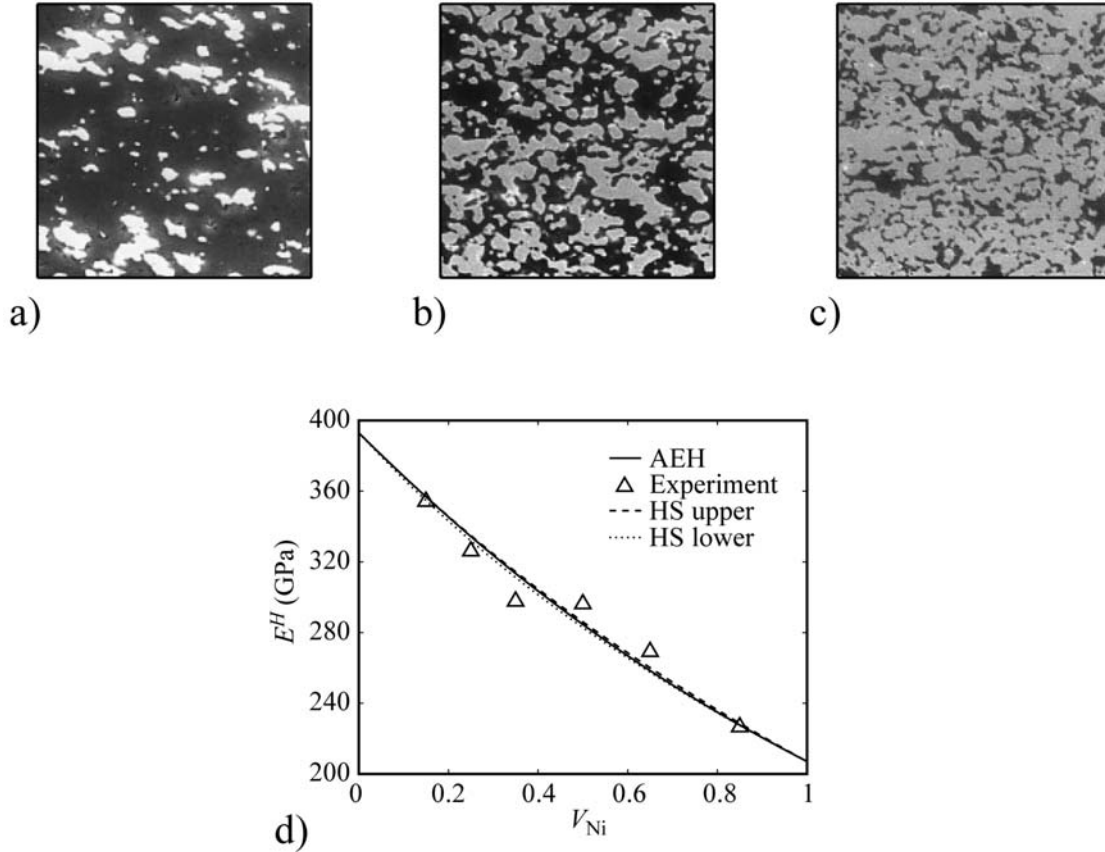
Figure 3.16. Actual N_i/Al2O$_3$ micrographs (Aldrich *et al.*, 2000) and comparison of predicted and actual Young's modulus. Volume fractions shown are a) $V_{Ni} = 0.15$, b) $V_{Ni} = 0.5$ and c) $V_{Ni} = 0.65$ with a comparison of Young's modulus predictions for RMDF microstructures, estimates and experimental values shown in d).

volume fractions. Due to a lack of error bars on the experimental results, it is not entirely clear whether the discrepancies are real or due to experimental variability.

The effect of contrast ratio on the homogenized material properties is investigated by considering a stainless steel/epoxy random heterogeneous material. As observed from Table 3.1, the contrast ratio between the Young's modulus of stainless steel and epoxy is 148. Sample stainless steel/epoxy micrographs are shown in Figures 3.17(a)-(c) for three different volume fractions (Wegner and Gibson, 2001). The homogenized material properties are shown in Figure 3.17(d) along with the experimental results, the Hashin-Shtrikman bounds and the self-consistent estimate. There is a large disparity
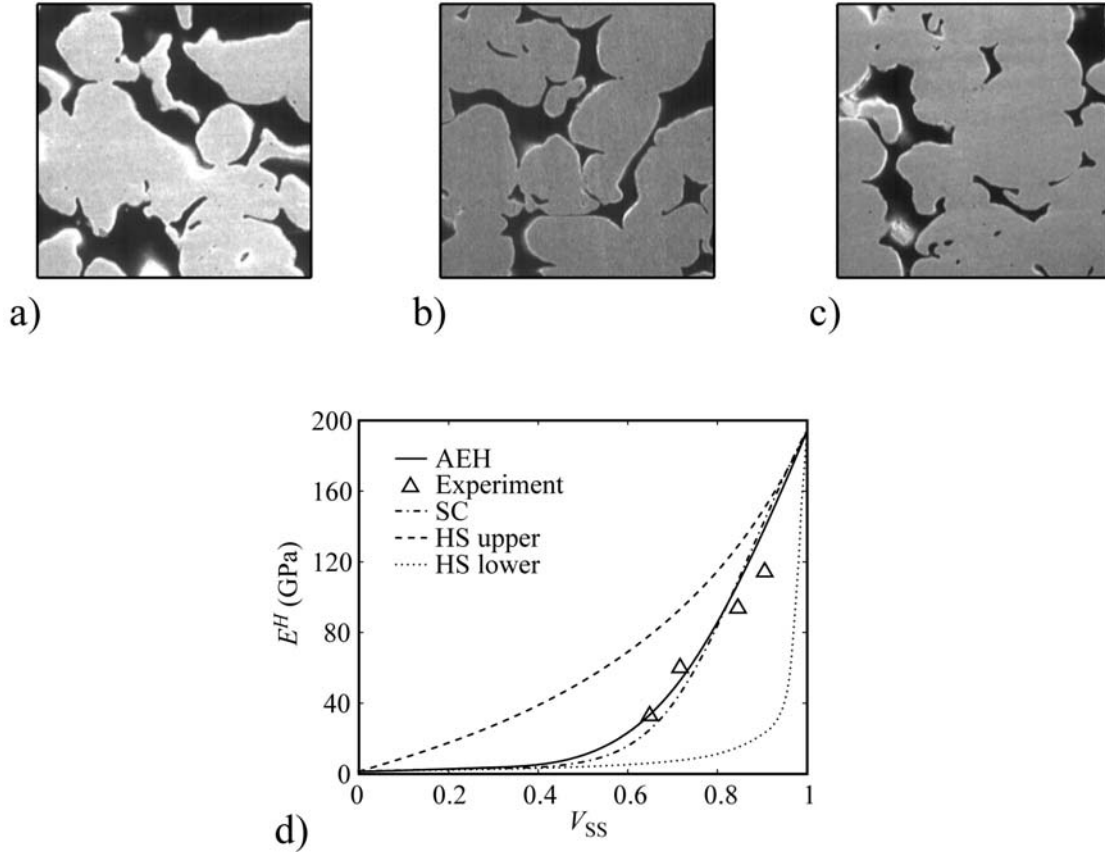
Figure 3.17. Actual SS/Resin micrographs (Wegner and Gibson, 2001) and comparison of predicted and actual Young's modulus. Volume fractions are shown for a) V_{SS} = 0.65, b) V_{SS} = 0.72 and c) V_{SS} = 0.91 with a comparison of Young's modulus predictions for RMDF microstructures, estimates and experimental values shown in d).

between the upper and lower bounds due to the significant difference in constituent material properties. The experimentally obtained values of the Young's moduli are in fairly good agreement with the AEH results except for large volume fractions. The difference between the two values is approximately 3.4% for V_{SS} = 0.65. The corresponding difference between the self-consistent and experimental values is 23.9%. Furthermore, unlike the other material combinations studied in this work that have moderate disparities in the phase material properties, the self-consistent values do not compare well with the AEH values for this high-contrast material combination. This

indicates that the self-consistent scheme may not be very reliable in estimating the effective properties for high-contrast composites, however, further study would need to be conducted in order to make more definitive statements with regard to this matter. In the least, this example demonstrates the importance of using a method such as AEH to accurately estimate homogenized material properties rather than assuming that various estimation schemes will provide accurate effective property values.

CHAPTER 4

DIRECT MICROMECHANICAL FAILURE ANALYSIS AND MULTISCALE SIMULATIONS OF RANDOM HETEROGENEOUS MATERIALS

In this chapter, the proposed multiscale approach for the analysis of heterogeneous structural components with random microstructure is demonstrated for representative metal/ceramic and metal/metal material combinations. After determining the initial failure envelopes of the random heterogeneous materials, the proposed multiscale analysis technique is demonstrated using two model problems with spatially varying material heterogeneity.

4.1 Microstructural Heat Flux and Stresses

The microscale heat flux and stresses are computed for prescribed macroscopic loads and a convergence study performed to ascertain the level of finite element refinement necessary to obtain accurate results. Consider a random Al/Al_2O_3 microstructure of width and height ℓ shown in Figure 4.1(a). This particular random microstructure has been created using the RMDF approach using a total of $N = 800$ random sources. The material properties of Al and Al_2O_3 are listed in Table 4.1. Both material phases in the chosen microstructure have identical volume fractions, $i.e.$, $V_{Al} = V_{Al_2O_3} = 0.5$. A representative finite element mesh used in the convergence study is shown in Figure 4.1(b). It consists of $7,920$ 6-noded triangular elements. As is evident, the complex morphological features are captured accurately by using a sufficient number of nodes on the material interfaces.

A convergence study is performed by applying a uniform uniaxial macroscopic stress state $\bar{\sigma}_{11}(\mathbf{x}) = 1$ MPa and the corresponding peak value of the microstresses in the RME are tracked as the mesh is refined. The maximum value of $\sigma_{11}^0(\mathbf{x}, \mathbf{y})$ is plotted as a function of the number of elements N_e in Figure 4.1(c). It should be noted that
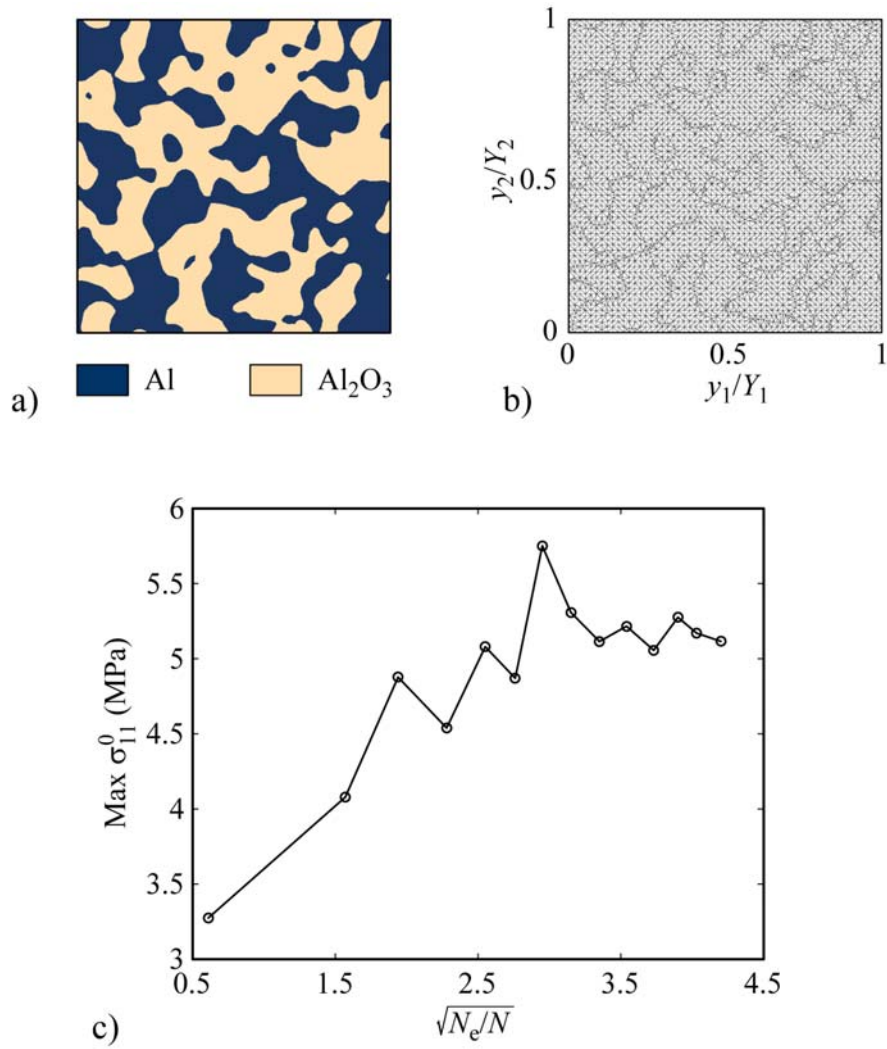
Figure 4.1. Sample Al/Al$_2$O$_3$ RMDF microstructure and accompanying finite element mesh consisting of 7,920 elements with convergence of σ_{11}^0 corresponding to an applied macroscopic stress $\bar{\sigma}_{11} = 1$ MPa. The RMDF microstructure is generated using $N = 800$ Gaussian sources with $V_{Al} = 0.5$.

the number of elements has been normalized by the number of RMDF sources N used to create the random microstructure since the number of elements needed to obtain accurate microstresses is expected to increase as the complexity of the microstructural morphology increases. It is observed that the ratio $\sqrt{N_e/N}$ has to be of the order of 3.15 or larger for the microstresses to converge. For example, a finite element mesh consisting of roughly $N_e = 8,000$ elements is necessary to obtain accurate microstresses for the random microstructure shown in Figure 4.1(a) which was created using $N = 800$ RMDF Gaussian functions. The results presented in the following sections are computed using a finite element mesh consisting of approximately $8,000$ elements to ensure sufficient accuracy.

A uniform macroscopic heat flux of $\bar{q}_1(\mathbf{x}) = 1$ W/m^2 is applied to a heterogeneous structure as depicted in Figure 4.2(a) and the corresponding microscopic heat flux components $q_1^0(\mathbf{x}, \mathbf{y})$ and $q_2^0(\mathbf{x}, \mathbf{y})$ are shown in Figures 4.2(b) and 4.2(c), respectively. It is observed that there are highly localized regions that have a relatively high microscopic heat flux $q_1^o(\mathbf{x}, \mathbf{y})$. The large heat flux occurs primarily in regions that have a narrow material pathway for the heat to flow in the highly conducting Aluminum phase. The ratio of the microscopic heat flux component $q_1^0(\mathbf{x}, \mathbf{y})$ to the macroscopic heat flux $\bar{q}_1(\mathbf{x})$ can be as high as 7.87 at certain locations for this particular random microstructure. The microscopic heat flux component $q_2^0(\mathbf{x}, \mathbf{y})$ need not be zero although the average macroscopic heat flux component $\bar{q}_2(\mathbf{x})$ is zero. This is due to the complex heat flow patterns within the random microstructure. It should be noted that results given here are for a specific microstructure and volume fraction. The distribution of heat flux and peak values will change significantly depending on the random microstructure being studied. Nonetheless, these results demonstrate that detailed information can be obtained at the microstructural level through a multiscale approach.
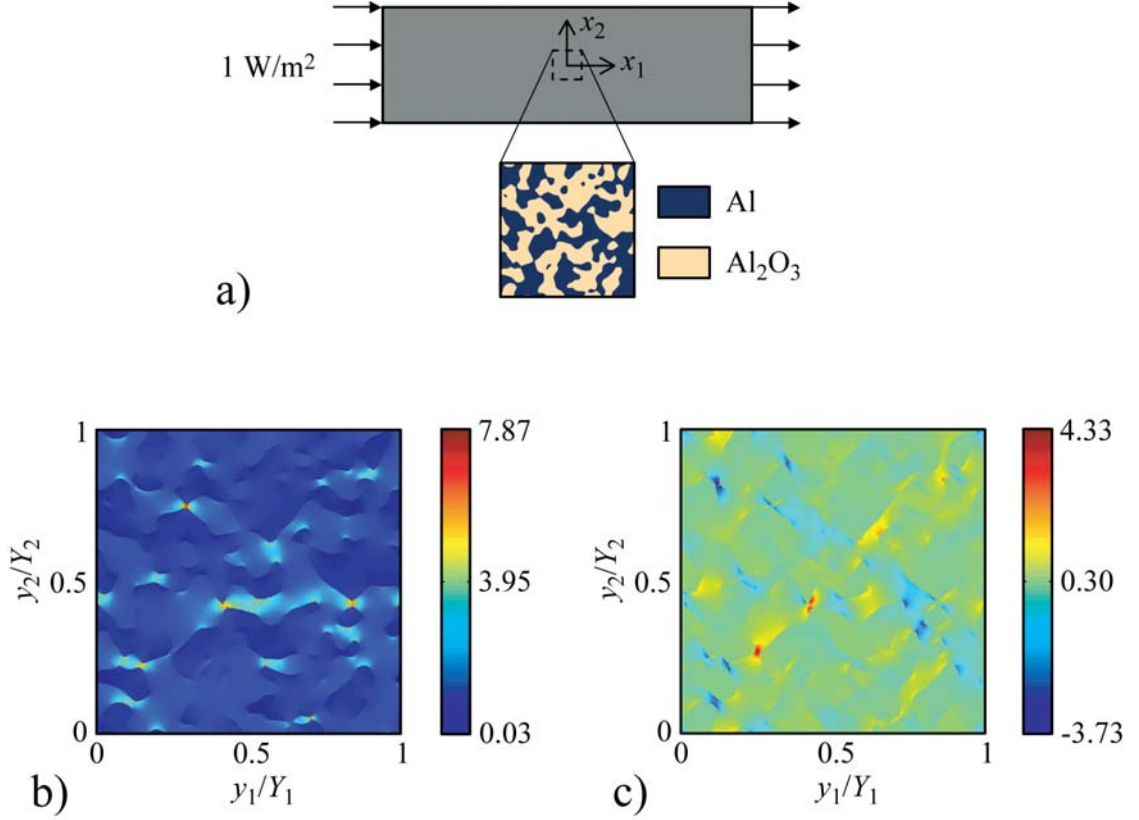
Figure 4.2. Schematic of a unit heat flux applied to a sample Al/Al_2O_3 random heterogeneous specimen and plots of the corresponding microflux components.

The thermal deformation and microstresses are investigated for a heterogenous structure that is subjected to a uniform macroscopic temperature change $\theta^o(\mathbf{x}) = 1°C$. The structure is free to expand in all directions. The deformed shape of the RME is shown in Figure 4.3(a). As is evident from the deformed shape of the boundaries, the periodic boundary conditions are satisfied. The thermal microstresses $\sigma_{11}^0(\mathbf{x}, \mathbf{y})$, $\sigma_{22}^0(\mathbf{x}, \mathbf{y})$, $\sigma_{12}^0(\mathbf{x}, \mathbf{y})$ and $\sigma_{33}^0(\mathbf{x}, \mathbf{y})$ are shown in Figures 4.3(b), (c), (d) and (e), respectively. It should be noted that the microstress components are non-zero although the average macroscopic stress components $\bar{\sigma}_{ij}(\mathbf{x})$ are zero. This is due to the heterogeneity of the material at lower length scales. In particular, the microstress component $\sigma_{33}^0(\mathbf{x}, \mathbf{y})$ is nonzero, as is evident from Figure 4.3(e), even though the average macrostress $\bar{\sigma}_{33}(\mathbf{x})$ is zero. This implies that in general a state of plane stress
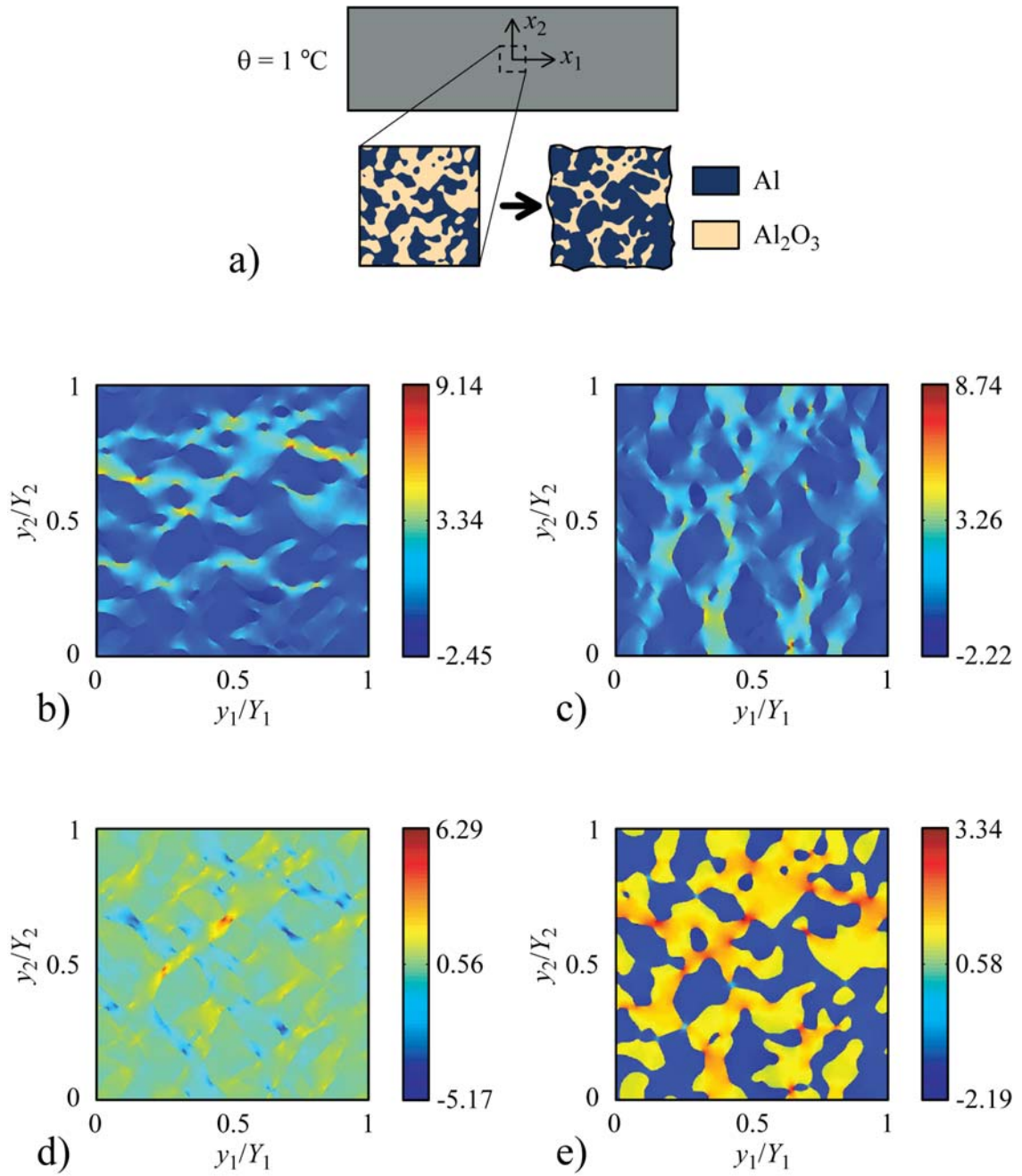
Figure 4.3. Schematic of sample Al/Al$_2$O$_3$ random heterogeneous specimen subjected to a unit temperature change along with the deformed microstructure and corresponding microstress components. Shown are b) σ_{11}^0 , c) σ_{22}^0, d) σ_{12}^0 and e) σ_{33}^0 in MPa.

at the macroscopic level does not necessarily imply plane stress conditions exist at the microscopic level. Since aluminum has a larger thermal expansion coefficient than alumina and the two phases are assumed to be perfectly bonded at the interface, a positive temperature change induces a compressive stress $\sigma_{33}^0(\mathbf{x}, \mathbf{y})$ in the Al phase and a tensile stress in the Al_2O_3 phase.

The microscopic deformation and microstress components due to an applied macroscopic uniaxial stress $\bar{\sigma}_{11}(\mathbf{x}) = 1$ MPa are presented in Figure 4.4. The peak microstress $\sigma_{11}^0(\mathbf{x}, \mathbf{y})$ within the RME is more than 5 times the applied macroscopic stress. In addition, the microstresses $\sigma_{22}^0(\mathbf{x}, \mathbf{y})$, $\sigma_{12}^0(\mathbf{x}, \mathbf{y})$ and $\sigma_{33}^0(\mathbf{x}, \mathbf{y})$, shown in Figures 4.4(c), (d) and (e), respectively, have minimum and maximum values that are on the order of the applied uniaxial stress in the x_1-direction, even though the corresponding average macroscopic stresses $\bar{\sigma}_{22}(\mathbf{x})$, $\bar{\sigma}_{12}(\mathbf{x})$ and $\bar{\sigma}_{33}(\mathbf{x})$ are all zero. While these results pertain to a particular microstructure, the figures indicate that stress patterns at the microscale are complex even when the macroscopic stress state is very simple. In addition, the results indicate that the stress concentrations at the microscale can be quite significant. This fact has important implications concerning the strength of random heterogenous media which will be addressed next.

4.2 Initial Failure Envelopes for Al/Al_2O_3 and W/Cu

In this section, we use direct micromechanical failure analysis to obtain failure envelopes for random heterogeneous materials. Initial failure envelopes are generated for random heterogeneous materials by applying macroscopically uniform temperature and average stresses and analyzing failure at the microstructural level. Failure is checked at the quadrature points at the microstructural level and the appropriate failure criteria is used depending on whether the point lies within the ductile or brittle phase. Initial failure of the microstructure is assumed to occur when the microstresses at one or more quadrature points exceeds the failure strength. The resulting failure
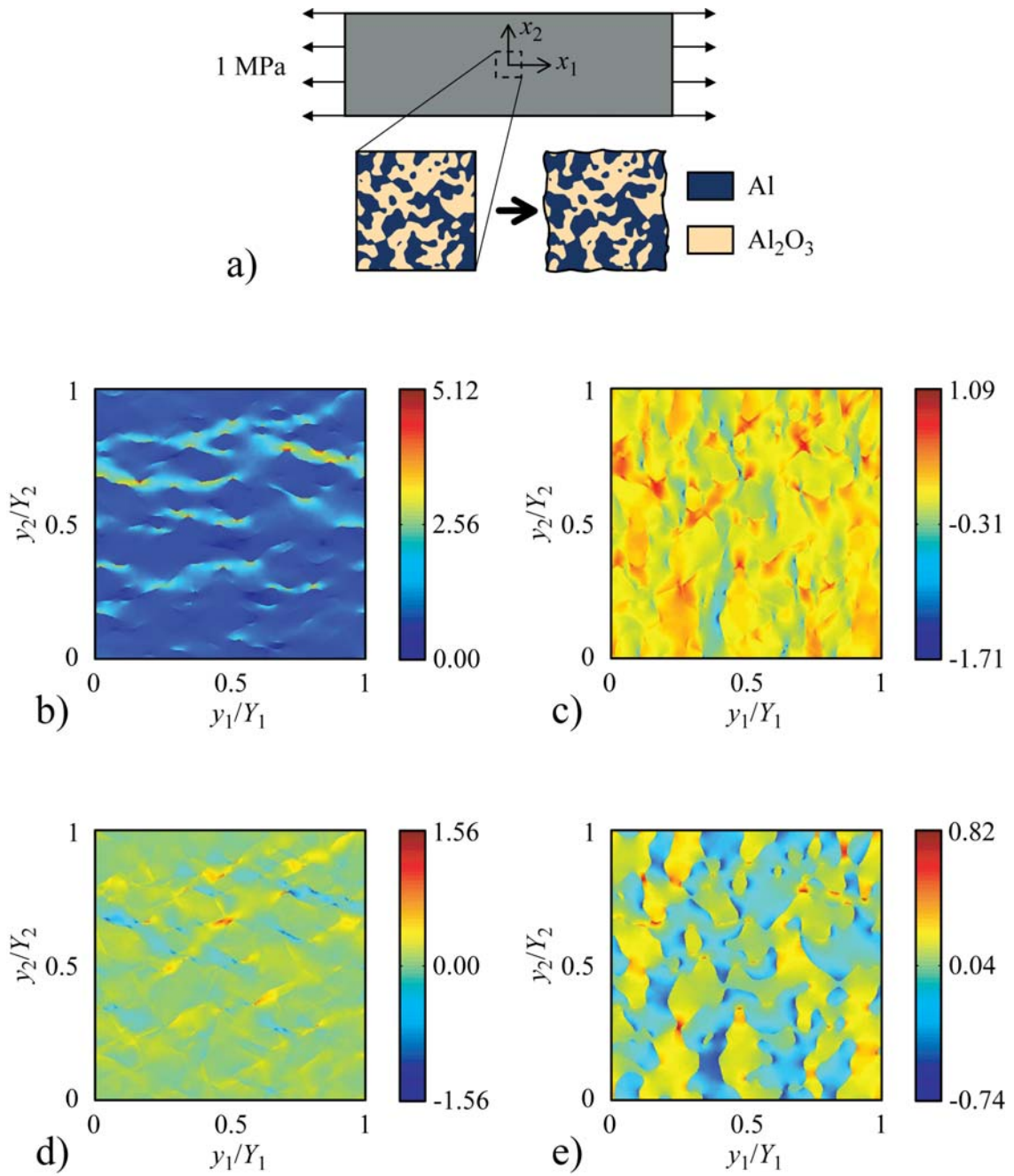
Figure 4.4. Schematic of sample Al/Al_2O_3 random heterogeneous specimen subjected to a uniform macroscopic stress $\bar{\sigma}_{11} = 1$ MPa along with the deformed microstructure and corresponding microstress components. Shown are b) σ_{11}^0, c) σ_{22}^0, d) σ_{12}^0 and e) σ_{33}^0 in MPa.

envelopes, while conservative, provide a realistic measure of the strength of random heterogeneous material under multi-axial stress states. It should be noted that the analysis of heterogenous materials loaded beyond their initial failure loads would require a nonlinear elastoplastic multiscale formulation (*e.g.* see (Terada and Kikuchi, 1995; Ghosh *et al.*, 1996; Soppa *et al.*, 2003)) which is not the focus of this work.

The microstresses consist of thermal and mechanical components which are evaluated separately. First, the thermal microstresses $(\sigma_{ij}^0)^{\text{thermal}}$ corresponding to a uniform temperature change θ and zero macroscopic stresses (*i.e.*, $\bar{\sigma}_{ij} = 0$) are determined through multiscale analysis. Next, the mechanical microstresses are evaluated for the following uniform macroscopic stress field,

$$\bar{\sigma}_{11}(\varphi) = \sigma_0 \cos \varphi, \quad \bar{\sigma}_{22}(\varphi) = \sigma_0 \sin \varphi, \tag{58}$$

and $\bar{\sigma}_{12}(\varphi) = 0$, where σ_0 is an arbitrary constant stress and φ is a fixed angle. The microstresses $(\sigma_{ij}^0)^{\text{mech}}$ corresponding to the average stresses (58) are obtained through the interscale transfer operators. The combined thermal and mechanical microstresses are obtained using superposition as follows,

$$\sigma_{ij}^0 = (\sigma_{ij}^0)^{\text{thermal}} + (\sigma_{ij}^0)^{\text{mech}}.$$

The value of σ_0 at which initial failure occurs at the microstructural level (*i.e.* $F_s^{\text{macro}} = 1$) is denoted by σ_0^f and the corresponding point on the failure envelope is

$$\bar{\sigma}_1^f(\varphi) = \sigma_0^f \cos \varphi, \quad \bar{\sigma}_2^f(\varphi) = \sigma_0^f \sin \varphi.$$

The complete failure envelope for a particular random microstructure is obtained by repeating the procedure with φ varying from $0°$ to $360°$. The initial failure envelopes

Material Property	Al	Al$_2$O$_3$	W	Cu
κ (W/m°C)	233.0	30.0	172.1	377.7
E (GPa)	70.0	393.0	397.8	128.2
ν	0.3	0.22	0.297	0.338
α (10^{-6}/°C)	23.4	7.6	3.94	15.74
S_y (MPa)	275.0	–	$1,352.2$	296.3
S_{ut} (MPa)	–	260.0	–	–
S_{uc} (MPa)	–	$2,600.0$	–	–

Table 4.1. Thermal conductivity, κ, Young's modulus, E, Poisson's ratio, ν, thermal expansion coefficient, α, yield strength, S_y, ultimate strength in tension, S_{ut}, and ultimate strength in compression, S_{uc}, of selected materials considered in the present chapter.

for an ensemble of $1,000$ random microstructures are averaged to obtain a mean failure envelope that is useful for assessing the strength of random heterogeneous components when precise information regarding the microstructure is lacking, which is often the case in practical applications.

We first focus on the strength of a metal/ceramic heterogenous material. Specifically, we consider Al/Al$_2$O$_3$ microstructures created using the RMDF approach. The relevant thermal and mechanical material properties of Al and Al$_2$O$_3$ are listed in Table 4.1. The yield strength of ductile Al is taken to be $S_y = 275$ MPa. The ultimate tensile and compressive strengths of the brittle Al$_2$O$_3$ are $S_{ut} = 260$ MPa and $S_{uc} = 2,600$ MPa, respectively. The initial failure envelopes are generated for $1,000$ distinct random microstructures. The average failure envelope as well as the failure envelopes corresponding to plus and minus one standard deviation are shown in Figure 4.5 for $V_{Al} = 0.5$. The stresses $\bar{\sigma}_1$ and $\bar{\sigma}_2$ in this and all subsequent failure envelopes are the macroscopic principal stresses. The scatter in the strength values
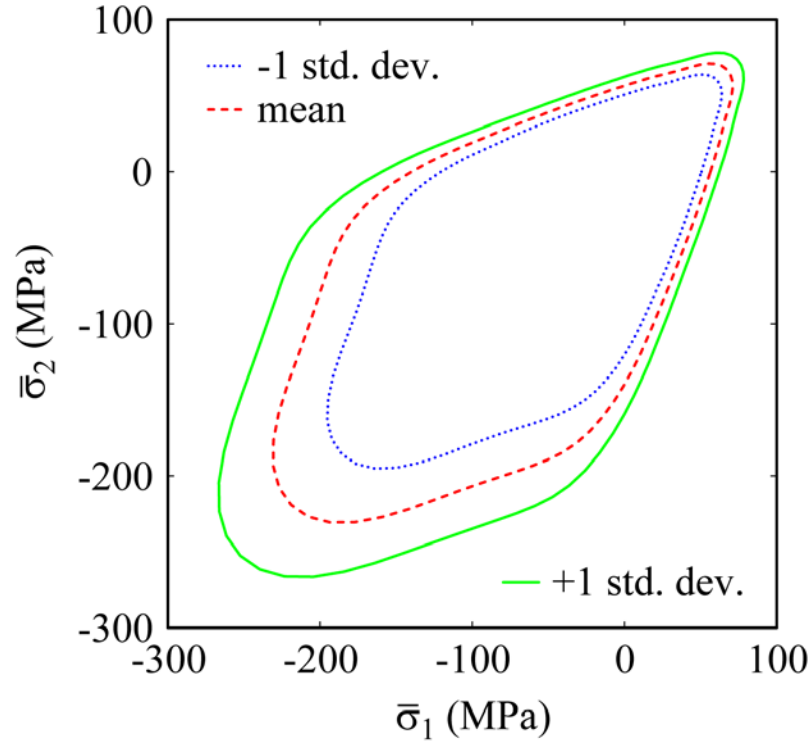
Figure 4.5. Initial failure envelope for Al/Al$_2$O$_3$ random heterogeneous materials with $V_{Al} = 0.5$ as well as envelopes representing plus and minus one standard deviation.

can be attributed to the fact that there is significant variation in the peak stresses from one random microstructure to another. The standard deviation is highest when both principal stresses are compressive. The coefficient of variation lies in the range of 10% to 16% for all points on the failure envelope. Despite the variability, the average initial failure envelope provides a reasonable estimate of the strength of random heterogeneous materials under multi-axial loads. In what follows, it is understood that the initial failure envelopes shown are obtained by averaging over a sufficiently large ensemble of random microstructures.

The initial failure envelopes for various volume fractions ranging from $V_{Al} = 0$ to $V_{Al} = 1$ are shown in Figure 4.6(a). As is expected, a modified-Mohr failure envelope for homogenous Al$_2$O$_3$ is obtained for $V_{Al} = 0$ and a von Mises elliptical failure envelope is obtained for $V_{Al} = 1$. The failure envelope of Al$_2$O$_3$ is in general larger than the
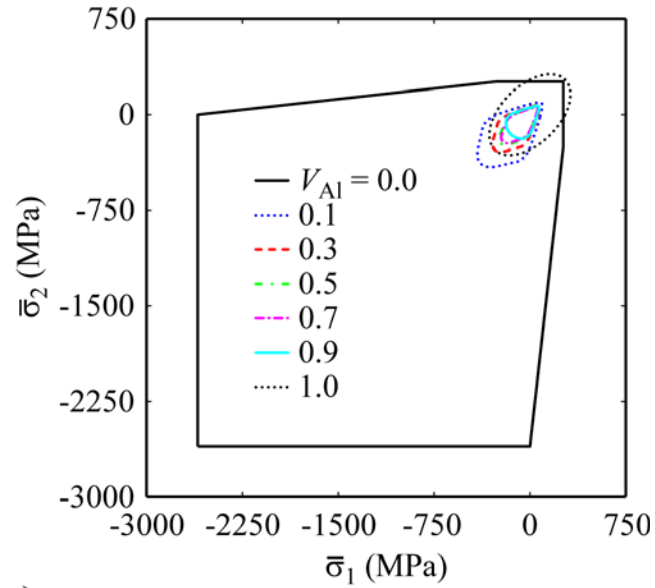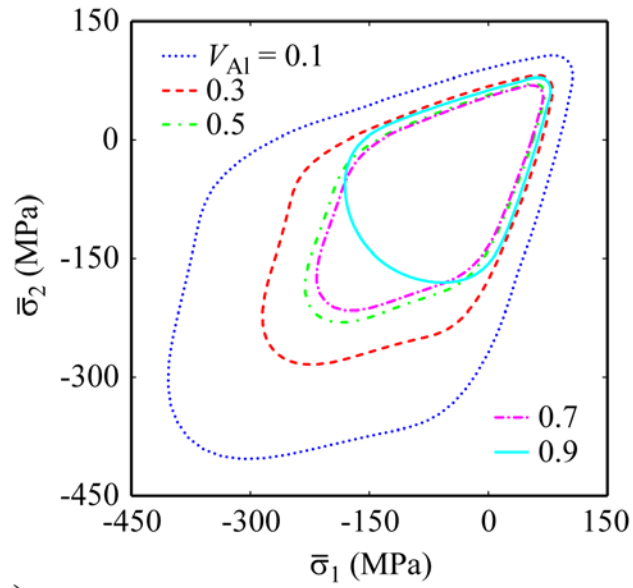
Figure 4.6. Initial failure envelopes for Al/Al$_2$O$_3$ random heterogeneous media. Shown are plots corresponding to a) the whole range of volume fractions and b) only intermediate volume fractions. The RMDF microstructures are generated using $N = 800$ Gaussian sources.

failure envelope for the Al phase especially when both $\bar{\sigma}_1$ and $\bar{\sigma}_2$ are compressive. The failure envelopes for the intermediate volume fractions are approximately the size of failure envelope for aluminum, or smaller. This indicates that the strength of the weaker phase is the dominant factor that influences the overall strength of the material. Enlarged failure envelopes for intermediate volume fractions are presented in Figure 4.6(b). As can be seen from this figure, all volume fractions shown with the exception of $V_{Al} = 0.1$ have failure envelopes that are completely contained within the aluminum failure envelope indicating that the combination of material phases often yields a heterogeneous material that is weaker than either of its constituents. The failure envelopes demonstrate that a metal/ceramic heterogeneous material has larger strengths under compressive stresses than under tensile stresses. This is due to the large compressive strengths of the ceramic phase relative to the tensile strength of the metal and ceramic phases. Heterogeneous materials have higher strengths under biaxial compression relative to the yield strength of the metal for low metal volume fractions, *e.g.* $V_{Al} = 0.1$. However, they exhibit lower strengths under tensile loads compared to that of the metal. The heterogeneous material has a diamond shaped failure envelope with rounded edges of varying radii that clearly draws some of its characteristic features from the elliptical von Mises failure envelope and some from the modified-Mohr failure envelope.

The failure envelope of a metal/metal heterogeneous is investigated next. Since both constituents are ductile, the failure envelopes are expected to be distinctly different from those presented earlier for metal/ceramic heterogeneous materials. The particular metal/metal heterogeneous material studied here is a W/Cu combination since it has several high temperature applications. Tungsten has a higher yield strength and stiffness but a significantly lower thermal conductivity than copper. The relevant material properties are listed in Table 4.1. Direct micromechanical failure analysis was performed by holding the material at its stress free reference temperature. The inter-
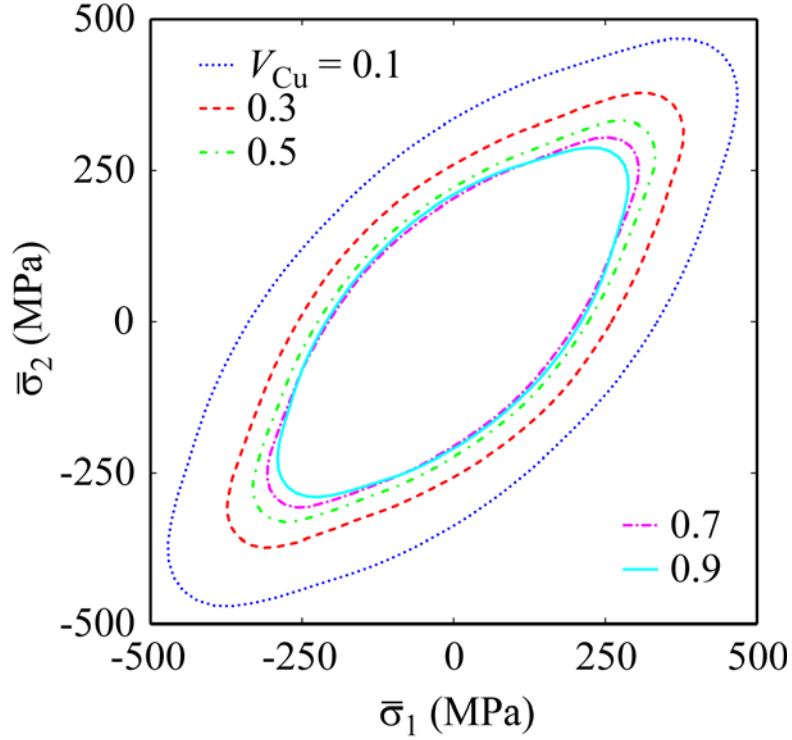
Figure 4.7. Initial failure envelopes for W/Cu random heterogeneous media for intermediate volume fractions. The RMDF microstructures are generated using $N = 800$ Gaussian sources.

faces are assumed to be perfectly bonded with an infinitely large interface strength. Initial failure envelopes for a W/Cu heterogeneous material are shown in Figure 4.7 for intermediate volume fractions of copper. The failure envelopes, which are nearly elliptical, decrease in size as the volume fraction of the copper phase increases since copper is weaker than tungsten.

It is important to understand how temperature effects the failure envelopes in practical applications. At high temperatures, the thermally induced microstresses can have a detrimental effect on the failure strength of a heterogeneous material. Failure envelopes are created by holding the temperature θ^o fixed while the macroscopically applied stresses are increased until the material fails at the microscopic level. Here, θ^o represents the change in temperature from the stress free temperature. Failure envelopes for a W/Cu heterogeneous material are shown in Figure 4.8 for three dif-
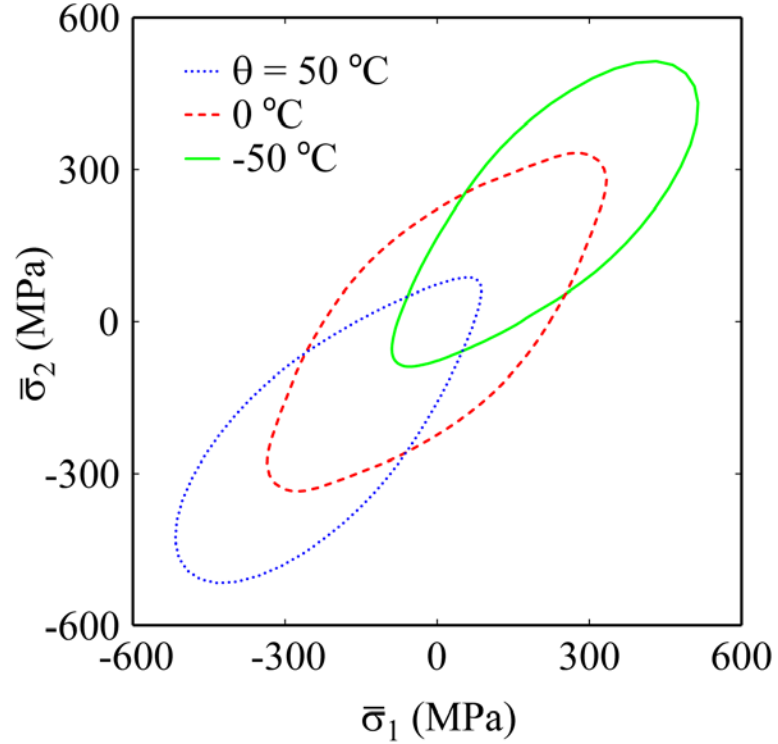
Figure 4.8. Initial failure envelopes for W/Cu random heterogeneous media for three different temperature changes θ = -50 °C, 0 °C and 50 °C. The RMDF microstructures are generated using $N = 800$ Gaussian sources with $V_{\text{Cu}} = 0.5$.

ferent temperatures $\theta^o = 0°C$, 50°C, and $-50°C$. The failure envelopes correspond to a volume fraction of $V_{\text{Cu}} = 0.5$. Figure 4.8 demonstrates that the temperature has a significant effect on the failure of heterogeneous materials. The failure envelope at the stress free reference temperature $\theta^o = 0°C$ is approximately an off-axis ellipse that is centered at $\bar{\sigma}_1 = 0$, $\bar{\sigma}_2 = 0$. As the temperature is increased by $\theta^o = 50°C$ from the stress free reference temperature, the internal thermal stresses cause the center of the failure envelope to shift to the third quadrant accompanied by a small change in shape. Thus, the heterogenous material cannot withstand large tensile stresses at elevated temperatures due to the thermal microstresses. However, it is still capable of withstanding large biaxial compressive stresses at temperatures above the stress-free reference temperature. The trend is reversed when the heterogeneous material is cooled below the stress-free reference temperature. The material can

71

withstand larger biaxial tensile stresses when it is cooled but its ability to withstand compressive stresses is reduced.

4.3 Multiscale Analysis of Heterogeneous Components

In this section, the proposed multiscale analysis technique is demonstrated using two model problems. The random heterogeneous materials considered in the model problems belong to a class of materials known as functionally graded materials. FGMs are heterogeneous material systems that are engineered to have a smooth spatial variation of material properties. This is achieved by gradually varying the microstructure and relative volume fractions of the constituent phases from one point to another during the fabrication process. By considering a spatially varying microstructure in the model problems, we demonstrate that the proposed multiscale approach is well suited for the accurate analysis of problems with complex spatially varying microstructural morphologies. In addition to accurately computing the macroscopic field quantities for both model problems, the multiscale approach also allows for a more detailed assessment of failure of the random heterogeneous material of which the FGM components are comprised. In both problems, the results show that the current implementation of the direct micromechanical failure analysis provides a fairly conservative estimate of failure.

4.3.1 Failure Analysis of an Al/Al_2O_3 Heterogeneous Component with Random Microstructure Subjected to a Pressure Load

In this first model problem, we perform a micro-macro computational analysis of a simply supported Al/Al_2O_3 functionally graded thick beam that is subjected to a mechanical load. The material exhibits a random heterogeneous microstructure with a spatially varying volume fraction distribution. The geometry, loading and boundary conditions of the functionally graded beam are shown in Figure 4.9. The beam, which is of length $2L = 60$ mm and height $H = 15$ mm, is subjected to a uniform
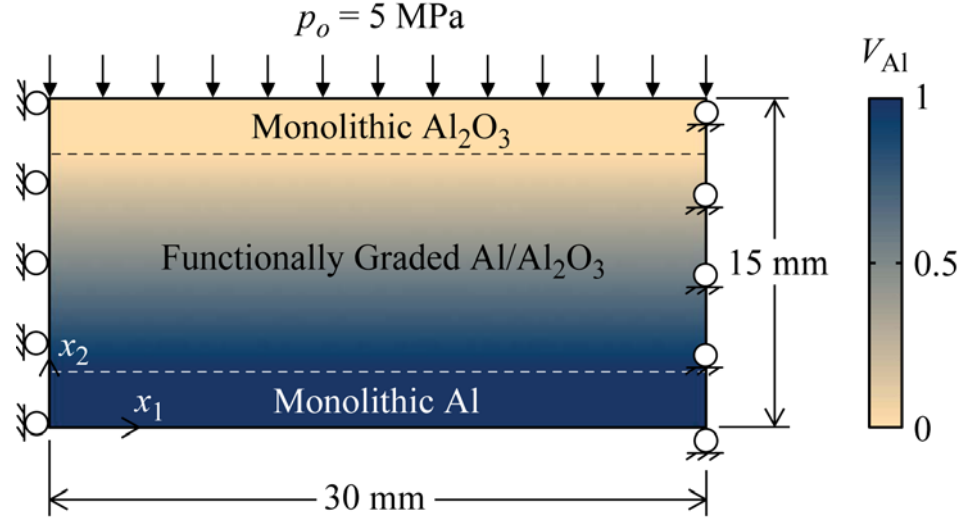
Figure 4.9.   Schematic of geometry and volume fraction distribution for a model Al/Al$_2$O$_3$ functionally graded beam that is simply supported on the edges and subjected to a uniform distributed load on its top surface.

distributed load of magnitude $p_0 = 5$ MPa on its upper surface. Only the right half of the beam is analyzed due to symmetry about the mid-span. The origin of the global $x_1 - x_2$ coordinate system is located on the bottom surface at the mid-span location. The x_1 and x_2 directions are aligned with the longitudinal and thickness directions, respectively. A two-dimensional plane stress analysis is performed at the macroscopic level with symmetry boundary conditions $u_1^0(0, x_2) = 0$ and $\bar{\sigma}_{12}(0, x_2) = 0$ applied along the left edge.   Simply supported boundary conditions at the right edge are simulated by the pointwise boundary conditions $u_2^0(L, x_2) = 0$ and $\bar{\sigma}_{11}(L, x_2) = 0$. The beam consists of monolithic layers of Al$_2$O$_3$ and Al on the top and bottom surfaces, respectively, each of which are of thickness $H/6$. The intermediate region has a linearly graded volume fraction that varies only in the thickness direction as follows,

$$
V_{\text{Al}}(x_1, x_2) = \begin{cases} 1 & \text{if} \quad x_2 \leq H/6 \\ 1 - \dfrac{3}{2H}(x_2 - \dfrac{H}{6}) & \text{if} \quad H/6 < x_2 < 5H/6 \\ 0 & \text{if} \quad x_2 \geq 5H/6 \end{cases} .
$$

73

The effective material properties at each location are determined using the asymptotic homogenization and ensemble averaging procedure described in the preceding chapter. A finite element mesh consisting of a total of $3,600$ 6-noded triangular elements is used to analyze the macroscopic thermoelasticity problem. The spatial variation of the average macroscopic stresses $\bar{\sigma}_{11}(\mathbf{x})$, $\bar{\sigma}_{12}(\mathbf{x})$ and $\bar{\sigma}_{22}(\mathbf{x})$ are shown in Figures 4.10(a)-(c) at the stress-free reference temperature. The peak compressive and tensile longitudinal stresses $\bar{\sigma}_{11}^{\min} = -105.45$ MPa and $\bar{\sigma}_{11}^{\max} = 36.38$ occur at the top and bottom surfaces, respectively. As expected, the largest shear stress occurs at the simply supported edge and it is of magnitude $|\bar{\sigma}_{12}|^{\max} = 16.00$ MPa. The factor of safety of the functionally graded beam is determined using the failure envelopes for Al/Al$_2$O$_3$ shown earlier in Figure 4.5 for various volume fractions of aluminum. The factor of safety $F_s^{\mathrm{macro}}(\mathbf{x})$ at a point $\mathbf{x}$ is defined as that factor by which the applied mechanical load of $p_0 = 5$ MPa can be multiplied that would result in failure at that point in the beam. The factor of safety thus obtained is plotted as a function of the spatial coordinates in Figure 4.10(d). The lowest factor of safety $F_s = 2.12$ over the entire domain occurs at point A at a point on the mid-span at coordinates $x_1 = 0, x_2 = 4.5$ mm with $V_{\mathrm{Al}} = 0.8$.

The macroscopic factor of safety distribution, shown in Figure 4.10(d), is based on an ensemble average of $1,000$ distinct random microstructures. This approach works well in practical applications since the specific random microstructures are seldom known at every location within the body. Nevertheless, it is useful to compare the factor of safety obtained from ensemble averages with the value obtained for sample random microstructures. Specific microstructures are assigned to the critical location A and their corresponding factor of safety $F_s^{\mathrm{micro}}(\mathbf{x}, \mathbf{y})$ obtained through failure analyses at the microscopic level. Three sample random microstructures and their corresponding microscopic factors of the safety are depicted in Figure 4.11. The minimum factor of safety occurs in the brittle Al$_2$O$_3$ particles which experience large tensile microstresses.
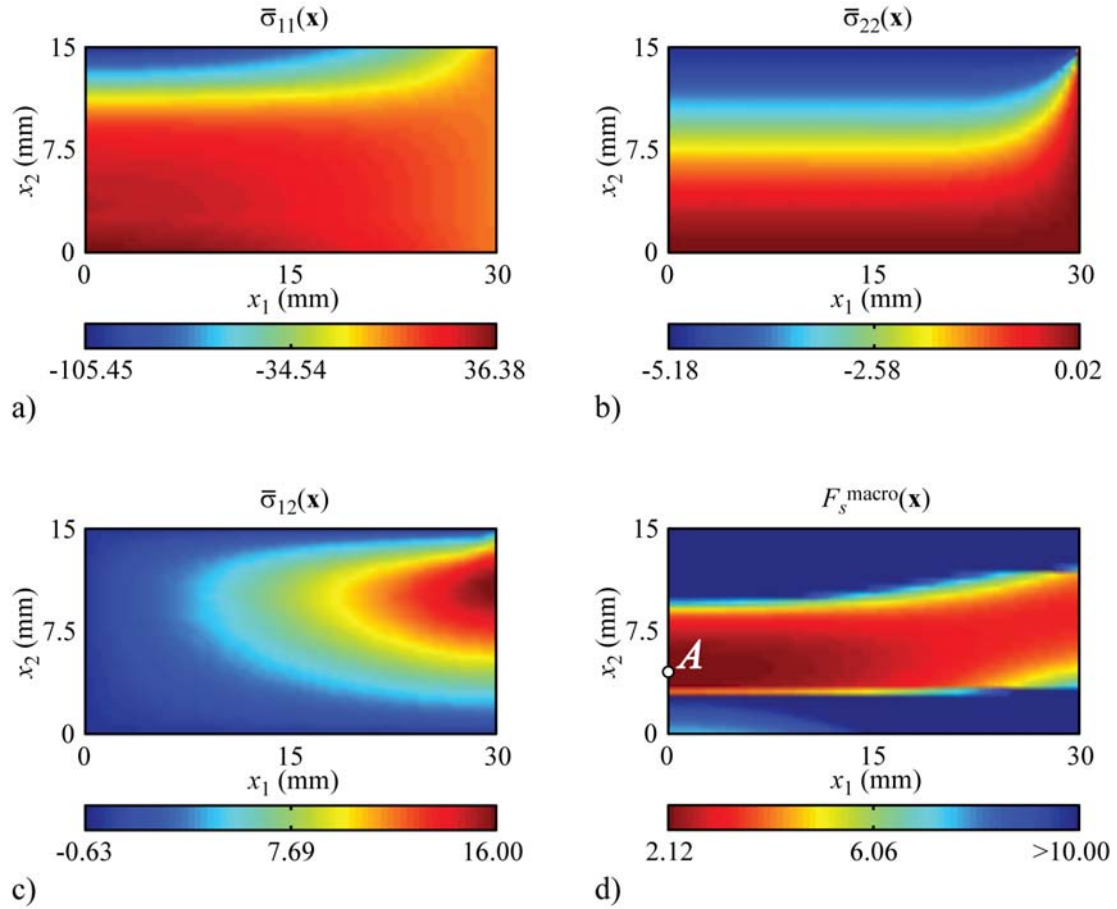
Figure 4.10. Contour plots of macroscopic stress components and factor of safety for model problem 1. Shown are a) $\bar{\sigma}_{11}$, b) $\bar{\sigma}_{22}$, c) $\bar{\sigma}_{12}$ in MPa and d) factor of safety F_s^{macro}. The minimum factor of safety occurs at the critical location A.

It is observed that although the sample random microstructures are all quite distinct, their minimum factors of safety, which are 1.94, 2.10 and 2.65, compare well with the value of 2.12 that was obtained earlier using ensemble averages (Figure 4.10(d)).

4.3.2 Failure Analysis of a W/Cu Heterogeneous Component with Random Microstructure Subjected to a High Heat Flux

The second model problem concerns a W/Cu functionally graded component that is subjected to an intense heat flux on a portion of its boundary. The geometry, boundary conditions and loading are shown in Figure 4.12. Only the right half of the body has been shown since it is symmetric about the plane $x_1 = 0$. A portion of

Figure 4.11. Three different sample RMDF microstructures at the critical location A ($V_{\mathrm{Al}} = 0.8$) and the corresponding factors of safety F_s^{micro} at the microscale. Shown are a,b) sample I, c,d) sample II and e,f) sample III.
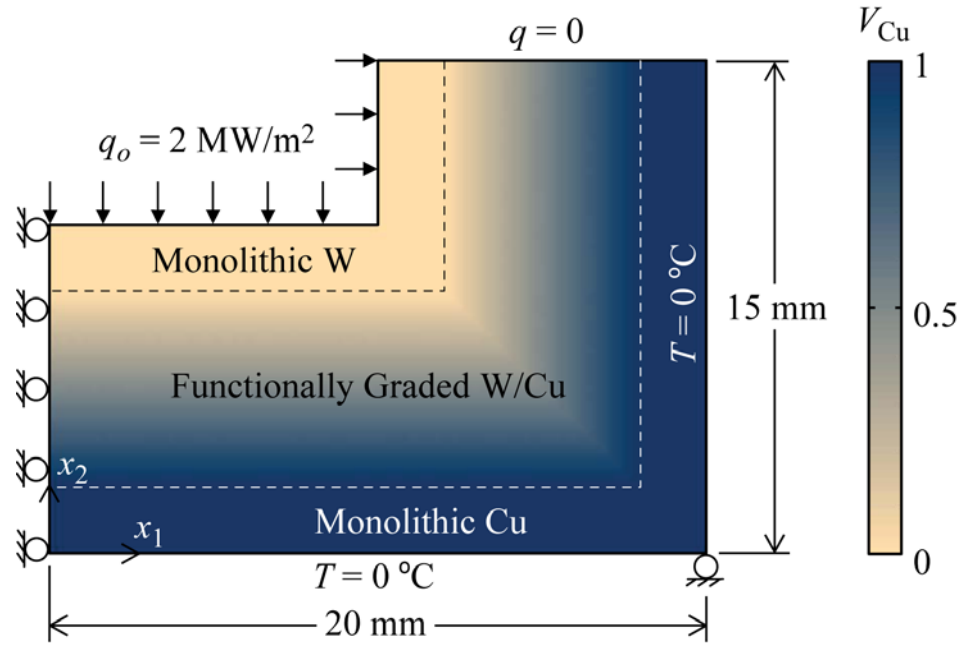
Figure 4.12. Schematic of geometry and volume fraction distribution for a W/Cu functionally graded component that is bi-directionally graded with an intense heat flux applied on a portion of its boundary.

its top surface is subjected to an intense heat flux of magnitude 2 MW/m² as shown in the figure. The bottom and right edges are held at the reference temperature. The W/Cu component has a 2 mm thick monolithic region of tungsten adjacent to the surfaces that are subjected to the high heat flux. In addition, it has a 2 mm thick monolithic region of copper near the bottom and right surfaces which are held at the reference temperature. The intermediate region has a bilinear volume fraction distribution, as shown in Figure 4.12. The material is assumed to be in a state of plane stress at the macroscopic level. The heterogeneous component is analyzed using a finite element mesh consisting of 4, 500 6-noded triangular elements.

The macroscopic temperature distribution is shown in Figure 4.13(a). The W/Cu component experiences a peak temperature change of 74.75°C at a point on the top surface which belongs to the monolithic tungsten region. The highest temperature change within the graded region is 52.12°C. The spatial variation of the average
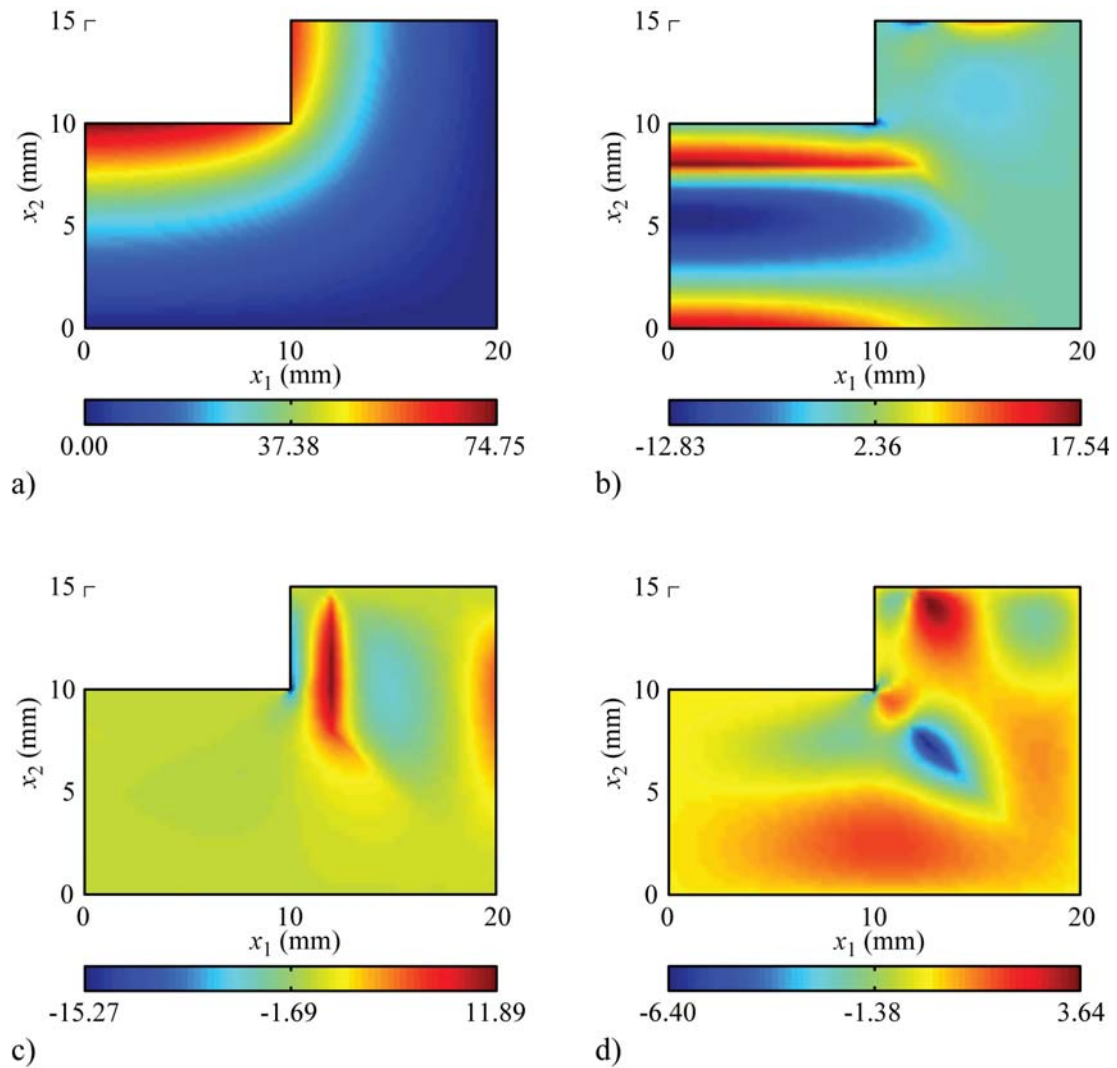
Figure 4.13. Contour plots of temperature and macroscopic stress components in a W/Cu functionally graded component. Shown are a) temperature θ in °C and macroscopic stress components b) $\bar{\sigma}_{11}$, c) $\bar{\sigma}_{22}$, d) $\bar{\sigma}_{12}$ in MPa.

macroscopic normal stresses $\bar{\sigma}_{11}(\mathbf{x})$ is shown in Figure 4.13(b). The peak tensile stress $\bar{\sigma}_{11}^{\max} = 17.54$ MPa occurs at the point $x_1 = 0, x_2 = 8.0$ mm which lies on the interface between the monolithic tungsten region and the graded region. The peak compressive stress $\bar{\sigma}_{11}^{\min} = -12.83$ MPa occurs in the functionally graded region at $x_1 = 0, x_2 = 5.33$ mm. The normal stress $\bar{\sigma}_{22}(\mathbf{x})$ and shear stress $\bar{\sigma}_{12}(\mathbf{x})$ are shown in Figures 4.13(c) and 4.13(d), respectively.

The accuracy of the macroscopic stress fields depends on the homogenization procedure used to determine the effective material properties. It has been previously shown the homogenized properties obtained using the self-consistent scheme are nearly identical to those obtained using the asymptotic homogenization technique for random heterogeneous materials for the types of material combinations considered here. Through-the-thickness plots of the macroscopic temperature and stress fields obtained using two different homogenization schemes are plotted in Figure 4.14. The results demonstrate that the macroscopic fields are almost identical for the self-consistent and the asymptotic homogenization methods. The peak temperature θ^o and peak normal stresses $\bar{\sigma}_{11}^{\max}$ obtained through the self-consistent homogenization scheme are off by 0.09% and 0.51%, respectively, from those obtained using the asymptotic homogenization technique. The fact that the self-consistent scheme gives accurate results for the homogenized material properties as well as the macroscopic temperature and stresses has important implications for practical applications. The self-consistent scheme, which is easier to implement than the asymptotic homogenization method, can lead to substantial time savings when analyzing large random heterogeneous structures. The determination of stresses and failure at the microstructural level would nevertheless require an accurate multiscale analysis for a given random microstructure.

The factor of safety $F_s^{\mathrm{macro}}(\mathbf{x})$ at each location within the W/Cu component is determined using failure envelopes for W/Cu similar to those presented earlier in Figures
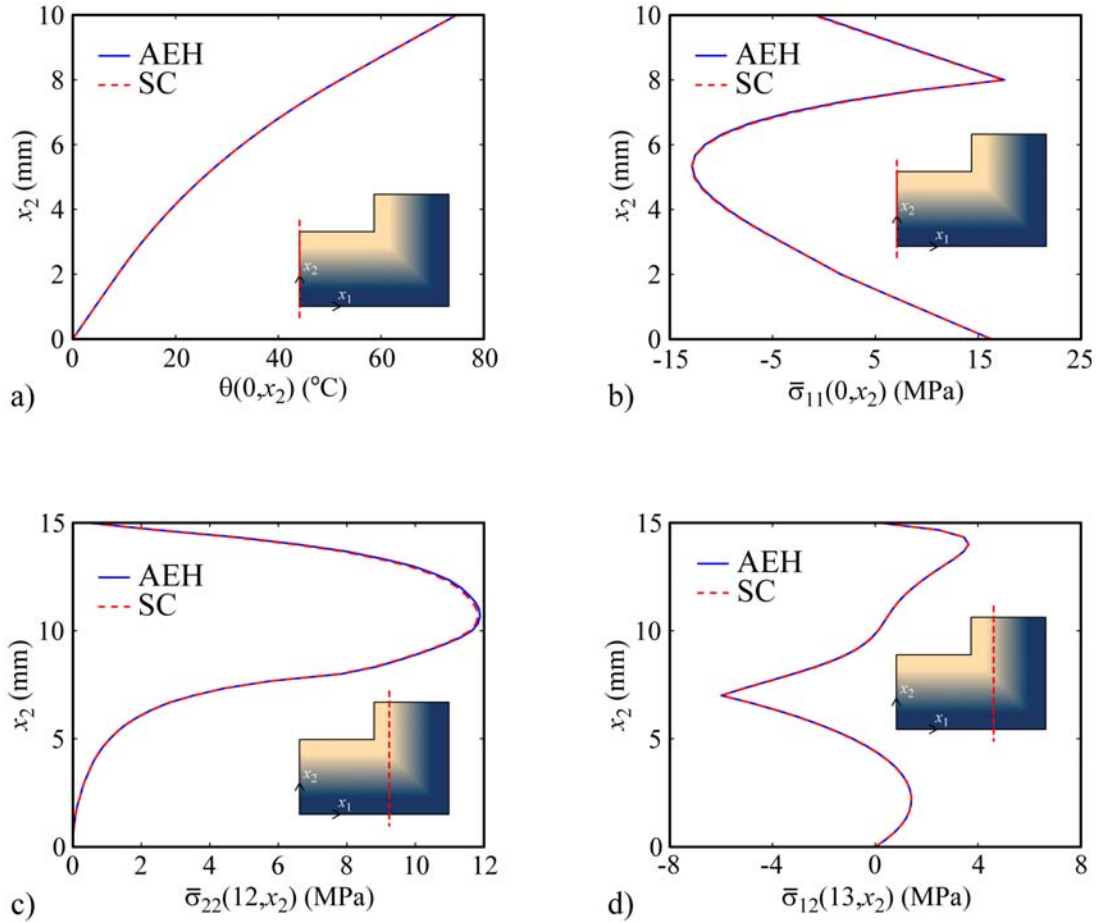
Figure 4.14. Comparison of temperature and macroscopic stress components using AEH homogenization vs. the self-consistent scheme. Shown are a) temperature θ in °C and macroscopic stress components b) $\bar{\sigma}_{11}$, c) $\bar{\sigma}_{22}$ and d) $\bar{\sigma}_{12}$ in MPa.

4.7 and 4.8 for different volume fractions and temperatures. The lowest factor of safety $F_s = 2.09$ occurs at critical location B with coordinates $x_1 = 0, x_2 = 6.33$ mm as shown in Figure 4.15. Said differently, the W/Cu component can withstand a maximum 4.18 MW/m^2 beyond which the microstresses at the critical location B will be large enough to cause failure. It should be noted that the minimum factor of safety does not occur at the location where the macroscopic stress $\bar{\sigma}_{11}$ is largest since failure depends not only on the macroscopic stresses but also on the temperature and local microstructure. Direct micromechanical failure analysis is performed at

80
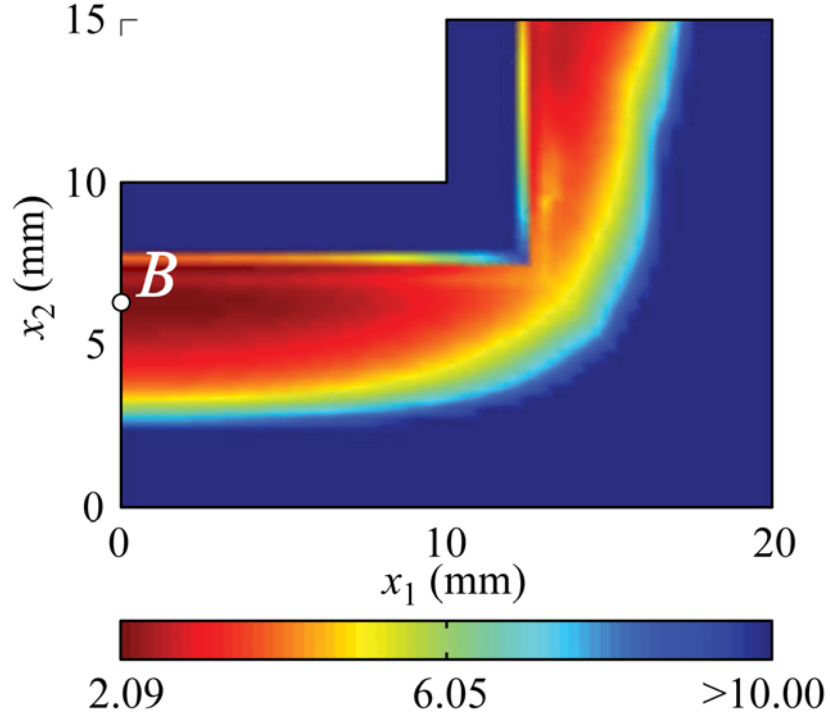
Figure 4.15. Contour plot of the factor of safety F_s^{macro} for the W/Cu functionally graded component. The minimum factor of safety occurs at the critical location B.

the critical location B for representative random microstructures with $V_{\mathrm{Cu}} = 0.278$. Three sample microstructures are shown in Figures 4.16(a), (c) and (e) and their corresponding factors of safety at the microstructural level $F_s^{\mathrm{micro}}(\mathbf{x}, \mathbf{y})$ are shown in Figures 4.16(b), (d) and (f), respectively. The minimum factors of safety occur in the weaker Cu phase for all three sample microstructures. Despite the significant differences between the three random microstructures, the minimum factors of safety obtained at the microstructural level, namely 1.70, 2.13 and 2.33, are reasonably close to the value of 2.09 that was obtained earlier using the failure envelopes.
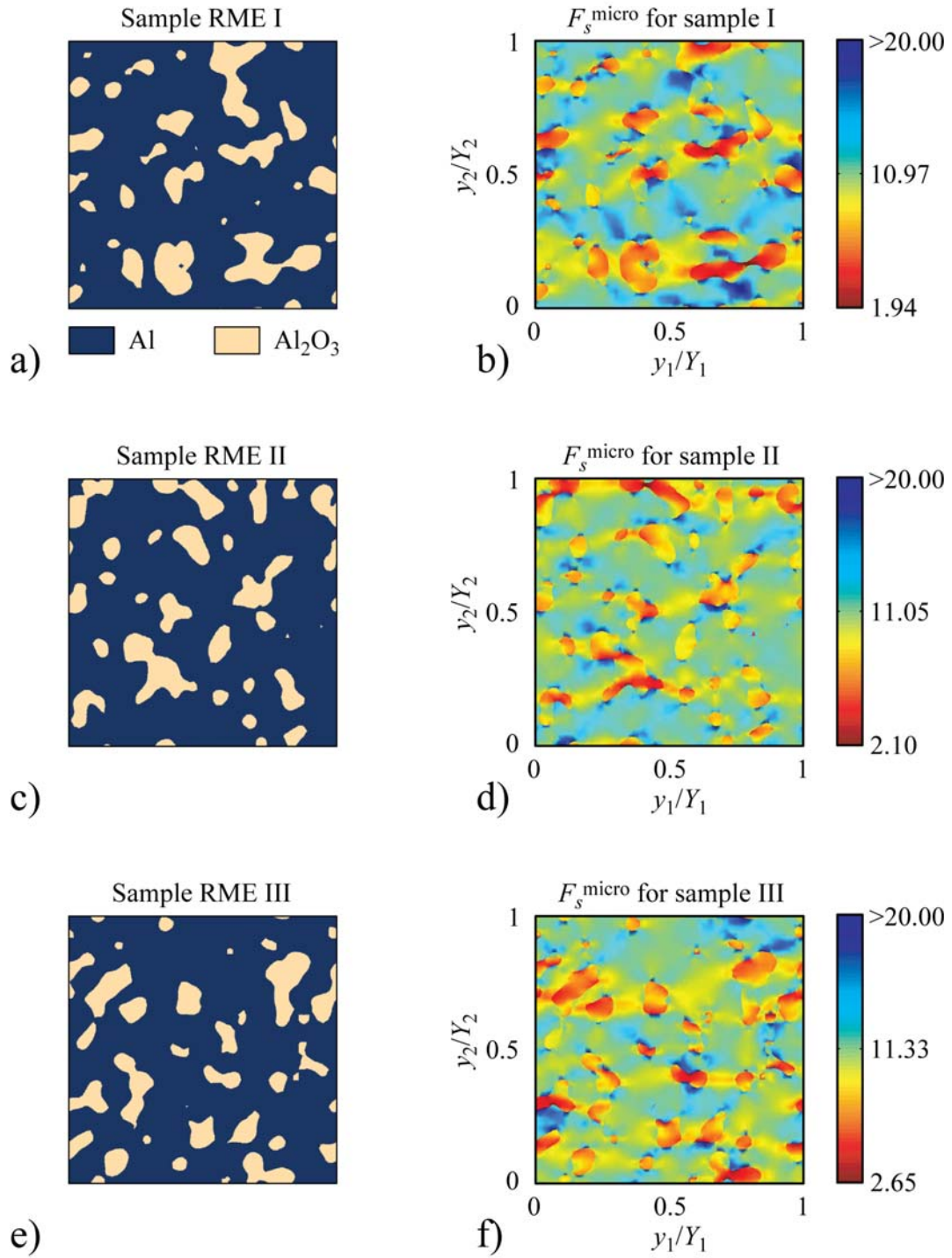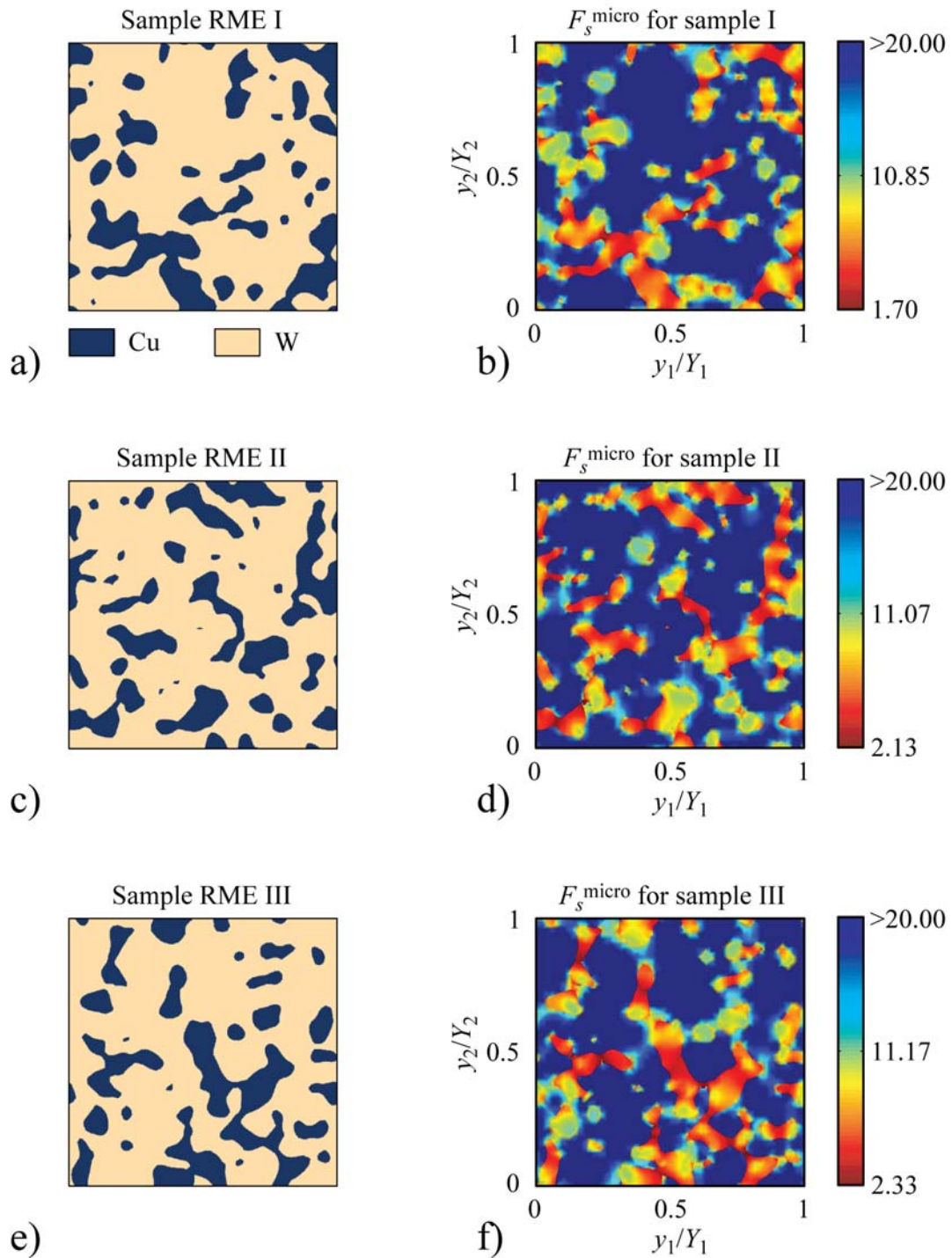
Figure 4.16. Three different sample RMDF microstructures at the critical location B ($V_{\mathrm{Cu}} = 0.278$) and the corresponding factors of safety F_s^{micro} at the microscale. Shown are a,b) sample I, c,d) sample II and e,f) sample III.

CHAPTER 5

TRANSIENT MULTISCALE THERMOELASTIC ANALYSIS OF FUNCTIONALLY GRADED MATERIALS

In this chapter, a methodology for the transient multiscale analyses of functionally graded components is presented. The methodology is validated against results found in the scientific literature to ensure that the multiscale procedure and macroscale time integration methods are working properly. Once validated, the methodology is demonstrated by performing transient failure analyses for two FGM problems, each which possess a smooth variation of phase volume fraction and microstructure morphology,

5.1 Microstructural Morphology Construction

Of interest in this work are two-phase functionally graded bodies with spatially varying microstructures, similar to the one shown in Figure 2.1. In order to proceed with the multiscale analysis, the microstructural morphology over the RME domain $\mathbf{y} \in Y$ must be known for all points in the macroscopic domain $\mathbf{x} \in \Omega$. To define the microstructural morphology, a MDF, similar in concept to the one implemented in (Cao and Liu, 2006) and in Section 3.1, is utilized. Depending on the choice of MDF, a wide range of microstructures corresponding to desired morphologies and phase volume fractions can be created. The variation of the microstructural morphologies over the domain Ω is specified by simply prescribing the macroscopic variation of the phase volume fractions.

The morphology description function, $f(\mathbf{y})$, is any periodic function in the RME domain Y normalized in such a fashion that $f(\mathbf{y}) \in [0, 1]$. Once a suitable MDF is created, the next step in creating a microstructure is to choose a cutoff value f_o that lies in the range $[0, 1]$. All locations in the RME domain $\mathbf{y} \in Y$ where $f(\mathbf{y}) > f_o$ are assumed to be occupied material phase 1. Conversely, all locations in the RME

where $f(\mathbf{y}) < f_o$ are occupied by material phase 2. To compute the volume fraction V_1 of the first phase, one can use the formula

$$V_1 = \frac{1}{|Y|} \int_Y \mathcal{H}\left(f(\mathbf{y}) - f_o\right) dY, \tag{59}$$

where $\mathcal{H}(\cdot)$ is the Heaviside step function. It is worth noting that the choice $f_o = 0$ yields $V_1 = 1$ and the selection $f_o = 1$ gives $V_1 = 0$. As there are only two material phases and material voids are prohibited, the sum of the phase volume fractions must always equal 1, $i.e.$, $V_1 + V_2 = 1$.

5.2 Validation of Multiscale Analysis

In this section, the multiscale analysis code is verified by comparing the results with those presented in the literature. The first validation problem, which will ensure that the microscale finite element results are accurate, is a static multiscale analysis. The second validation problem studied is a macroscopic transient heterogeneous material problem which is used to verify the accuracy of the transient macroscale finite element code.

5.2.1 Static Multiscale Analysis Validation Problem

In this first validation study, a multiscale analysis is performed for a boron/aluminum (B/Al) heterogenous thin plate with a hole in the center. This problem has been previously studied by Fish and Wagiman (1992) and Ghosh et $al.$ (1995). The Young's modulus and Poisson's ratio for the boron are $E = 400.0$ GPa and $\nu = 0.2$, respectively. For the aluminum, the Young's modulus is taken to be $E = 72.5$ GPa and the Poisson's ratio to be $\nu = 0.33$. Due to symmetry, only a quarter of the plate is modeled as shown in Figure 5.1(a). The entire plate is of height 3.0 m, of width 2.2 m and has a central hole of radius 0.1 m. The plate is subjected to an in-plane uniaxial traction of magnitude $p = 1.0$ Pa in the x_2 direction. The finite element mesh used for the macroscopic analysis, shown in Figure 5.1(b), consists
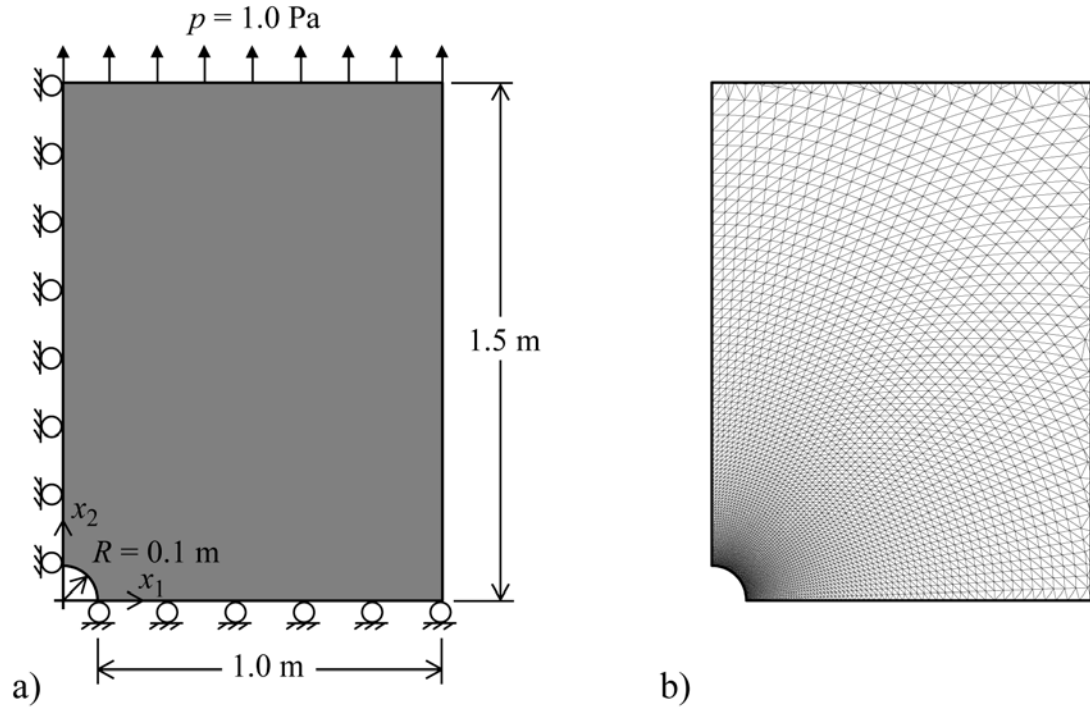
Figure 5.1. Schematic of plate with central hole loaded in tension and corresponding finite element mesh.
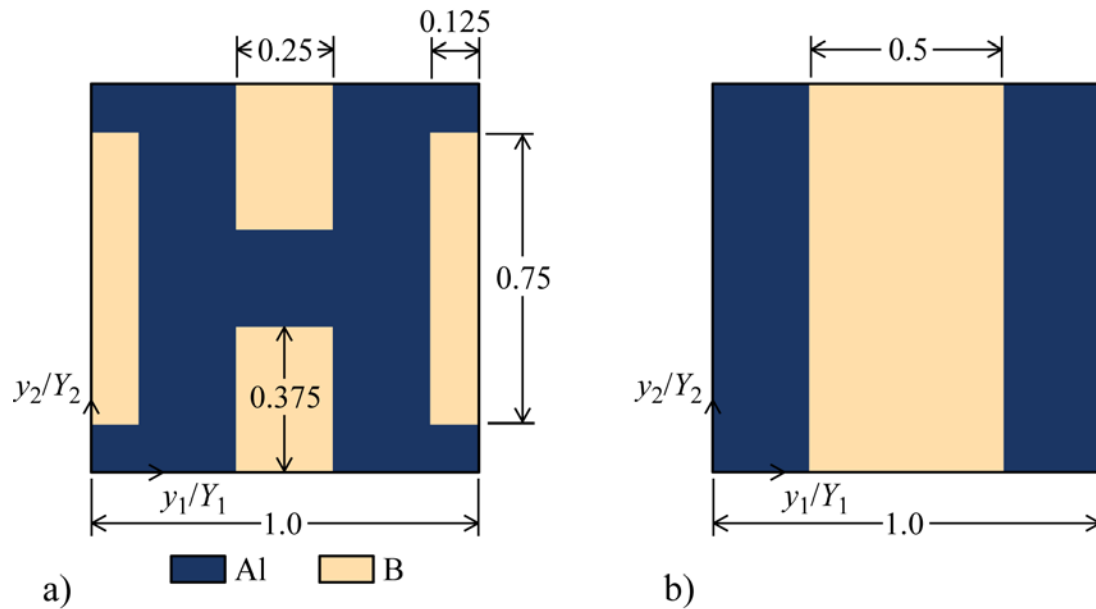
Figure 5.2. B/Al microstructure morphologies. Shown are a) short fiber and b) long fiber morphologies.

Method	D_{11}^H (GPa)	D_{22}^H (GPa)	D_{12}^H (GPa)	D_{33}^H (GPa)
AEH [Present Analysis]	122.29	151.03	36.30	42.07
Fish & Wagiman (1992)	122.46	151.35	36.19	42.11
VCFEM (Ghosh *et al.*, 1995)	118.81	139.76	38.05	42.44
HOMO2D (Ghosh *et al.*, 1995)	122.40	151.20	36.23	42.10

Table 5.1. Comparison of the homogenized B/Al short fiber elastic constants obtained from various methodologies.

of 8212 six-noded triangular (also called a linear strain triangle (LST)) elements. The plate is analyzed using two distinct B/Al microstructures. First, a short fiber morphology shown in Figure 5.2(a) of width and height ℓ is used, and second, a long fiber morphology also of width and height ℓ shown in Figure 5.2(b). In each case the microscale analyses are performed using a regular mesh of 3200 LST finite elements. Lastly, it is important to note that in previous studies of this problem not only is the macroscopic body in a state of plane-stress, it is also assumed that the material at the microscale level is in a state of plane-stress. While this in general is not true, the necessary modifications to the microscale finite element code are made for the sake of comparison in this validation problem.

The first step in performing the multiscale analyses is to compute the homogenized material properties. Table 5.1 compares the results for the homogenized elastic constants D_{ij}^H obtained using the AEH method of this work with the results of Fish and Wagiman (1992) and also the properties using the Voronoi cell finite element method (VCFEM) and two-dimensional (HOMO2D) code by Ghosh *et al.* (1995) for the short fiber microstructure. As can be seen in the table, the results for the homogenized elastic constants from the AEH method compare very well with those from literature with the one possible exception being the VCFEM results, which uses only four Voronoi cell finite elements. A similar comparison for the long fiber

Method	D_{11}^H (GPa)	D_{22}^H (GPa)	D_{12}^H (GPa)	D_{33}^H (GPa)
AEH [Present Analysis]	136.14	245.81	36.08	46.85
Fish & Wagiman (1992)	136.15	245.81	36.08	46.85
VCFEM (Ghosh *et al.*, 1995)	136.14	245.81	36.08	46.85
HOMO2D (Ghosh *et al.*, 1995)	136.10	245.80	36.08	46.85

Table 5.2. Comparison of the homogenized B/Al long fiber elastic constants obtained from various methodologies.

microstructure is given in Table 5.2. For the long fiber case, the AEH results are nearly identical to those provided by the other methods.

With the accuracy of the homogenized elastic constants established, a macroscopic analysis is performed to obtain the displacements, strains and average stresses. Once the macroscopic displacements $u_i^0(\mathbf{x})$ have been computed, the interscale transfer operator (25) is utilized to determine the stresses $\sigma_{ij}^0(\mathbf{x}, \mathbf{y})$ at the microscale. For comparison, the results of Ghosh *et al.* (1995), which use the commercial finite element package ANSYS at the macroscale and either the VCFEM or HOMO2D methods at the microscale, are used. The dominant microstress component $\sigma_{22}^0(\mathbf{x}, \mathbf{y})$ at the critical macroscopic location $x_1 = 0.1$ m, $x_2 = 0$, namely the right most edge of the hole, is shown in Figure 5.3. The tensile microstress in the y_2 direction is plotted along the width of the RME at locations along $y_2 = \ell/2$ for the short fiber case in Figure 5.3(a). The AEH stresses compare very well with the analysis using the HOMO2D microscale technique, and are similar to those generated with the VCFEM microscale method. The one significant discrepancy occurs with the multiscale results using the VCFEM microscale method in the regions surrounding the boundaries of the Voronoi cell elements, which incidentally occur at the locations $y_1/\ell = 0.25$, 0.75. However, as can be seen in the figure, the stress component in question is not continuous using the ANSYS/VCFEM methodology at the Voronoi cell boundaries,
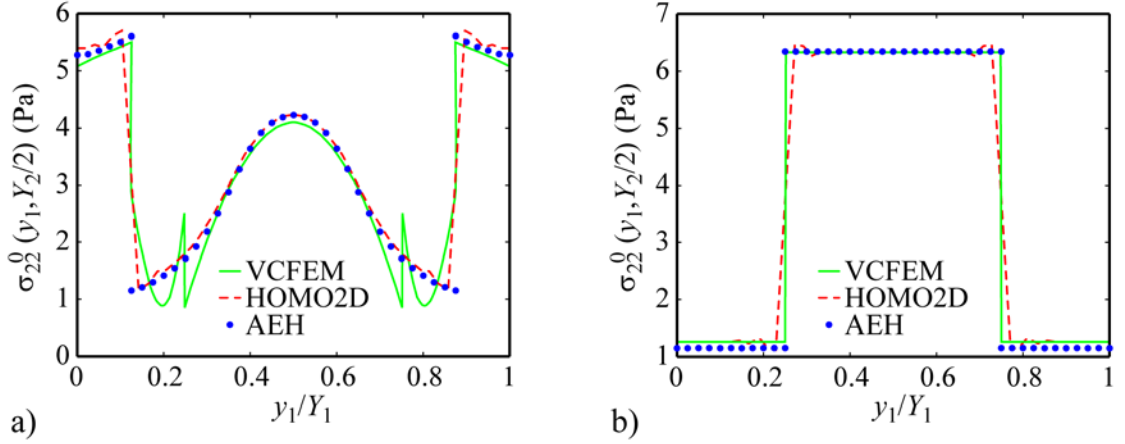
Figure 5.3. Comparison of through-the-width trends in the microstress component σ_{22}^0 at the critical location $x_1 = 0.1$ m, $x_2 = 0$. Cases shown are a) the short fiber case and b) the long fiber case.

as it should be. The AEH and ANSYS/HOMO2D techniques, which are in good agreement, predict a continuous variation in the stress component $\sigma_{22}^0(\mathbf{x}, \mathbf{y})$ with the exception of the phase boundary, which is expected. A similar comparison is given for the multiscale analysis using a long fiber microstructure in Figure 5.3(b). As can be seen in the figure, all three of the methodologies compare very well.

5.2.2 Transient Macroscopic Functionally Graded Material Analysis Validation Problem

In the second validation study, a functionally graded aluminum/silicon carbide (Al/SiC) thick plate subjected to a time-varying temperature increase on its top surface is investigated. The material properties for the phase materials is given in Table 5.3. The exact solution for the plate, for which the loading, SiC volume fraction variation V_{SiC} and boundary conditions are shown in Figure 5.4, is given by Vel and Batra (2003). Only one-half of the plate is modeled due to symmetry conditions, as shown in Figure 5.4 by setting the longitudinal displacement $u_1^0(0, x_2, t) = 0$ and average heat flux component $\bar{q}_1(0, x_2, t) = 0$ on the left edge of the domain. The right edge of the plate is simply supported, *i.e.* $u_2^0(0, x_2, t) = 0$. The two-dimensional plate,
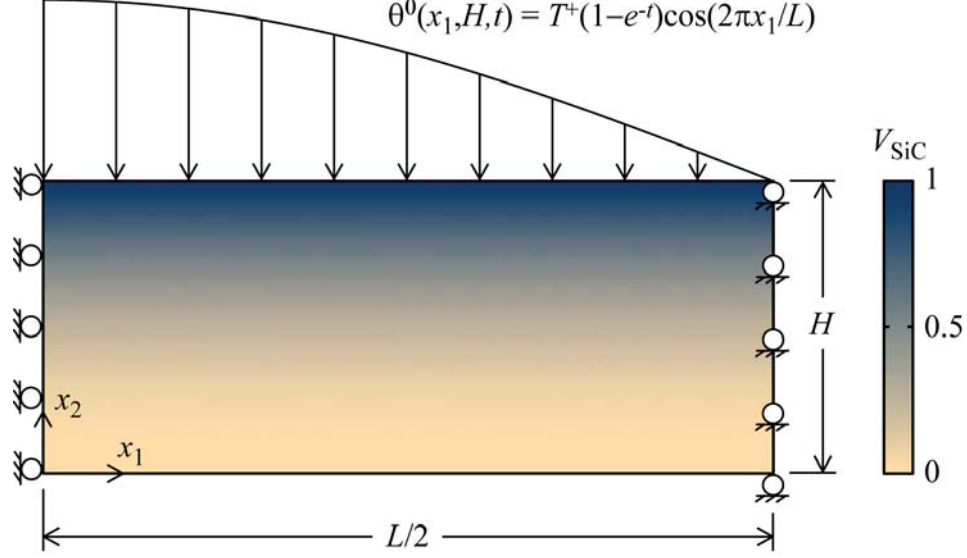
Figure 5.4. Schematic of loading, boundary conditions and volume fraction distribution for an Al/SiC functionally graded plate.

which is in a state of plane-strain, is of thickness H and of length L with $L/H = 5$. The SiC phase volume fraction varies only through the thickness direction and is of the form

$$V_{\text{SiC}}(\mathbf{x}) = \left(\frac{x_2}{H}\right)^2. \tag{60}$$

The temperature variation on the top surface is prescribed to be

$$\theta^0(x_1, H, t) = T^+ \left(1 - e^{-t}\right) \cos\left(2\pi x_1/L\right). \tag{61}$$

The temperature θ^0 is set to zero on the right and bottom edges of the domain. The homogenized properties of the Al/SiC heterogeneous material for the macroscopic analysis is obtained using the Mori-Tanaka method with metal as a matrix (Mori and Tanaka, 1973; Benveniste, 1987) in order to compare the results with those presented by Vel and Batra (2003). The Mori-Tanaka method requires only the phase volume fractions to obtain the homogenized effective properties. The macroscopic analysis is performed using a regular array of 2000 LST finite elements.

89
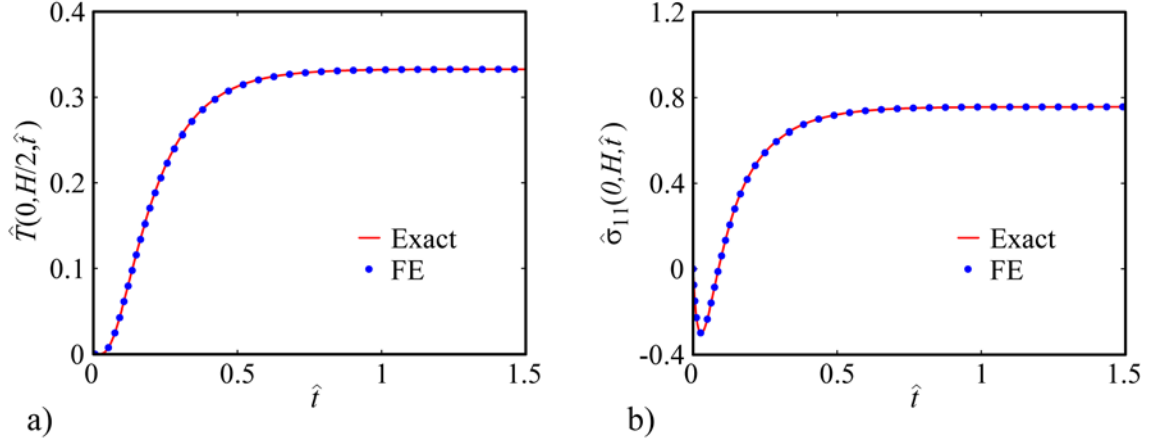
Figure 5.5. Comparison between the exact and finite element solutions at selected locations within the plate. Shown are a) normalized transient temperature variation and b) normalized transient bending stress.

The plots for this validation study utilize three non-dimensional quantities, these being

$$\hat{t} = \frac{t\kappa_{\text{Al}}}{C_{v\text{Al}}\rho_{\text{Al}}H^2}, \quad \hat{T} = \frac{\theta^0}{T^+}, \quad \hat{\sigma}_{11} = \frac{\bar{\sigma}_{11}}{E_{\text{Al}}\alpha_{\text{Al}}T^+}, \tag{62}$$

where $\hat{t}$ is the non-dimensional time, $\hat{T}$ is the non-dimensional temperature difference and $\hat{\sigma}_{11}$ is the non-dimensional bending stress component. The non-dimensional temperature and bending stress are plotted as function of non-dimensional time in Figure 5.5 for both the exact and macroscopic finite element solutions. The finite element solution is generated using a non-dimensional time step of $\Delta\hat{t} = 0.001$. As is evident from Figure 5.5, the two solutions are nearly coincident, indicating that the finite element approximation is fairly accurate. To further solidify the accuracy of the macroscopic finite element analysis, through-thickness plots are compared at the midspan of the plate at instant $\hat{t} = 0.1$. Figure 5.6 displays the non-dimensional temperature and longitudinal stress as a function of $\hat{x}_2 = x_2/H$ for the exact solution and finite element solution. Both compare very well with the error in the approximate solution being 2.38% for the peak stress $\hat{\sigma}_{11}$ at $\hat{x}_2 = 1.0$ in Figure 5.6(b).

90

a)

b)
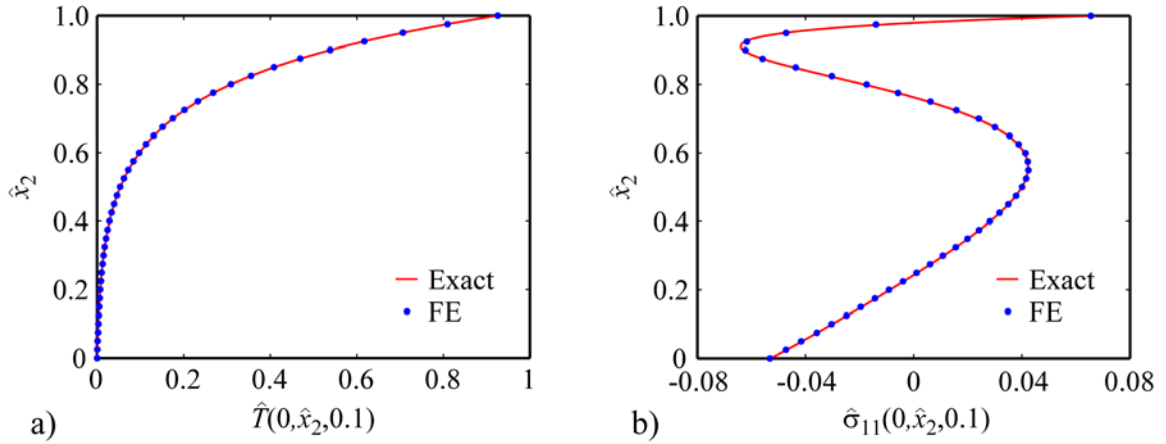
Figure 5.6. Through-thickness trends in the normalized temperature and bending stress at the normalized time $\hat{t} = 0.1$.

5.3 Multiscale Failure Analysis of Functionally Graded Material Components

In this section, two model problems are studied to illustrate the transient multiscale analysis of functionally graded materials. The first model problem is a tungsten/copper (W/Cu) beam with a spatially varying tungsten volume fraction subjected to a time-varying heat flux on a portion of its top surface. The two-phase W/Cu microstructures are created using a simplistic MDF that results in correspondingly simple microstructures for the entire volume fraction range. In the second model problem, a functionally graded titanium/zirconia (Ti/ZrO$_2$) turbine blade geometry with spatially varying volume fraction is studied. The Ti/ZrO$_2$ microstructural morphologies are created using a random MDF which results in fairly complex, realistic microstructures that compare well with actual micrographs of heterogeneous materials fabricated using plasma spraying or powder metallurgy.

5.3.1 Failure Analysis of a W/Cu Functionally Graded Component Subjected to a Localized Heat Flux

Figure 5.7 depicts the geometry, volume fraction distribution and boundary conditions for the W/Cu functionally graded component studied in this section. The material

91
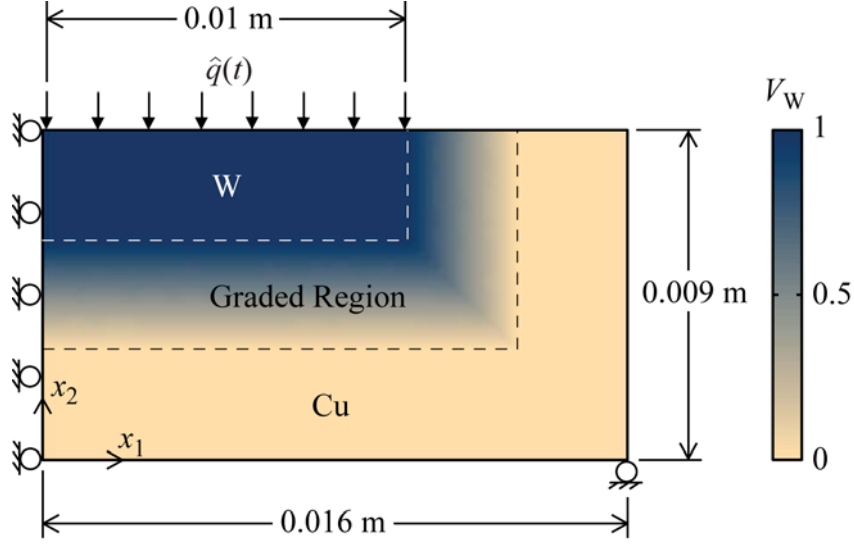
Figure 5.7. Schematic of loading, boundary conditions and volume fraction distribution for a W/Cu functionally graded specimen.

properties for tungsten and copper are given in Table 5.3. Only the right half of the plane-stress body is modeled due to symmetry conditions, as shown in Figure 5.7. The W/Cu specimen is of thickness 9.0 mm and length 32.0 mm. The bidirectional grading consists of a 3.0 mm thick monolithic layer of tungsten on a portion of its top edge, a 3.0 mm thick monolithic layer of copper along the bottom and right edges and a linear variation of the volume fraction in between the monolithic layers. A transient heat flux loading of the form

$$\hat{q}(t) = \begin{cases} 2.5\,(1-t) \ \mathrm{MW/m^2}, \ 0 < t < 1 \ \mathrm{s} \\ 0, \ t > 1 \ \mathrm{s} \end{cases} \tag{63}$$

is applied on the left 0.01 m of the top surface of the analysis domain as shown in Figure 5.7.

The microstructures of the W/Cu heterogeneous material are created using the MDF method described earlier. The particular MDF chosen for the model problem considered here is

$$f(\mathbf{y}) = \frac{1}{4} \left[2 - \cos\left(\frac{2\pi y_1}{\ell}\right) - \cos\left(\frac{2\pi y_2}{\ell}\right) \right]. \tag{64}$$

92

Material Property	Al	SiC	W	Cu
κ (W/mK)	233.0	65.0	163.3	385.0
E (GPa)	70.0	427.0	400.0	110.0
ν	0.3	0.17	0.28	0.34
α ($10^{-6}/K$)	23.4	4.3	4.4	16.4
ρ (kg/m^3)	2707	3100	19300	8960
C_v (J/kgK)	896.0	670.0	134.0	385.0
S_y (MPa)	–	–	1352.2	296.3

Table 5.3. Properties of selected materials considered in the present chapter.

A two-dimensional surface plot of the MDF over the RME domain is shown in Figure 5.8(a). Using equation (59), a relationship between a desired phase volume fraction and the corresponding cutoff value f_o is easily constructed. Microstructural morphologies corresponding to tungsten volume fractions of $V_W = 0.05$, 0.40, 0.50 and 0.75 are displayed in a 'tiled' 2×2 format in Figures 5.8(b)-(e), respectively. A sample finite element mesh corresponding to the microstructure with $V_W = 0.05$ is shown in Figure 5.8(f). It consists of approximately 3200 LST elements. The homogenized material properties for the series of W/Cu heterogeneous microstructures created using the MDF (64) are plotted in Figure 5.9 as a function of the tungsten volume fraction. A steep variation in the material properties occurs at a volume fraction of $V_W = 0.5$ for the homogenized thermal conductivity κ_{11}^H, Young's modulus E_{11}^H, Poisson's ratio ν_{12}^H and thermal expansion coefficient α_{11}^H. This is due to the fact that this particular volume fraction represents the point of percolation for the chosen MDF, or in other words, the point at which the tungsten transitions from being the particulate phase to becoming the matrix phase. The morphologies shown earlier in Figure 5.8 help illustrate this concept.

Figure 5.8. Microstructure morphology and analysis mesh used for the W/Cu hetero-geneous material. Shown are a) morphology description function, b)-e) morphologies for volume fractions of $V_W = 0.05$, 0.4, 0.5 and 0.75 respectively and f) finite element mesh for $V_W = 0.05$.
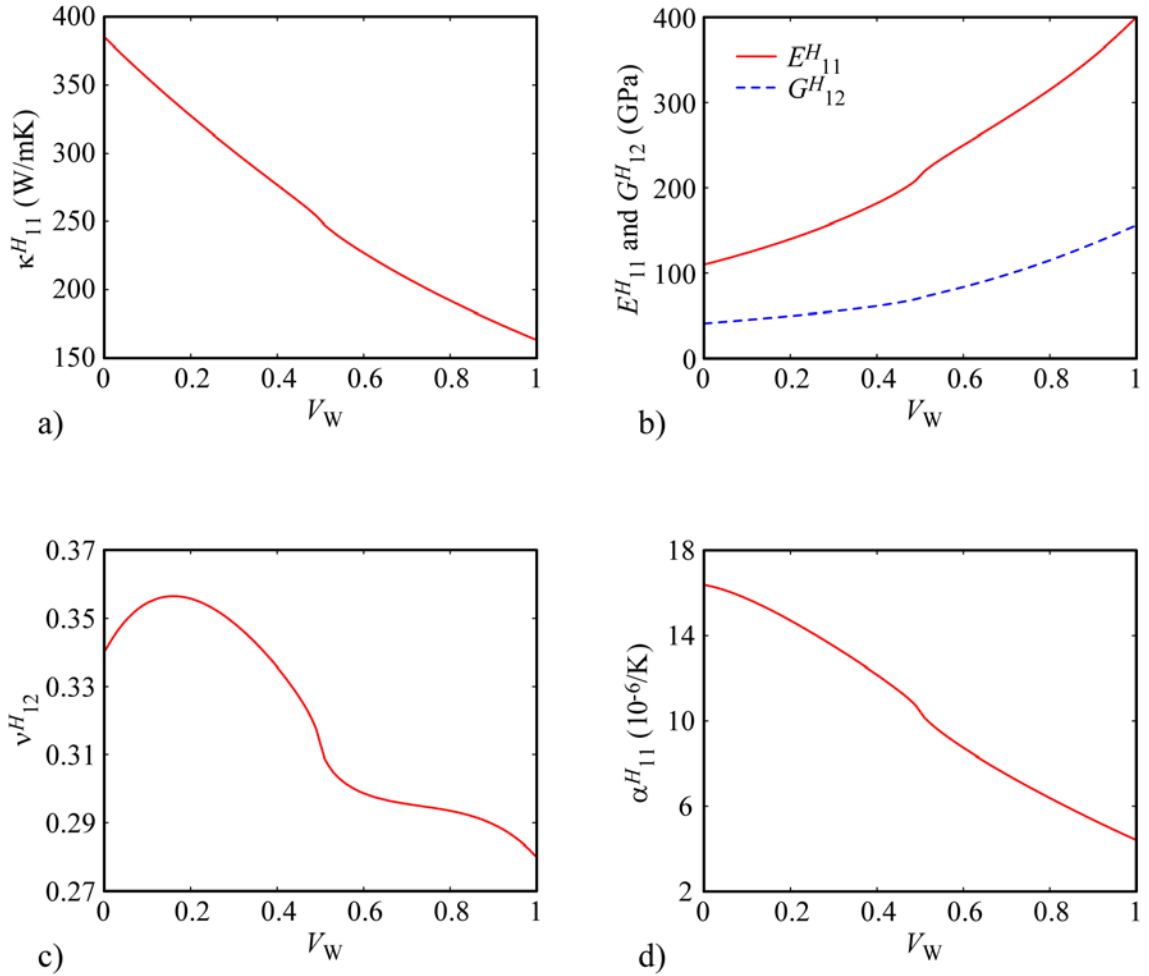
Figure 5.9. Homogenized properties for the W/Cu microstructures as a function of V_W. Shown are a) thermal conductivity, b) Young's and shear moduli, c) Poisson's ratio and d) thermal expansion.

A transient finite element analysis is performed using a regular array of 2592 LST finite elements at the macroscopic level with a time step of $\Delta t = 0.0005$ seconds. A direct micromechanical failure analysis is performed at each time step. The factor of safety against initial material failure is plotted in Figure 5.10. The minimum factor of safety F_s over the specimen is given as a function of time in Figure 5.10(a). The minimum value of $F_s = 2.05$ occurs at $t = 0.475$ seconds. The x_1 and x_2 coordinates of the location of the minimum F_s in the beam as a function of time are given in Figure 5.10(b). As can be seen from the figure, the critical location in the
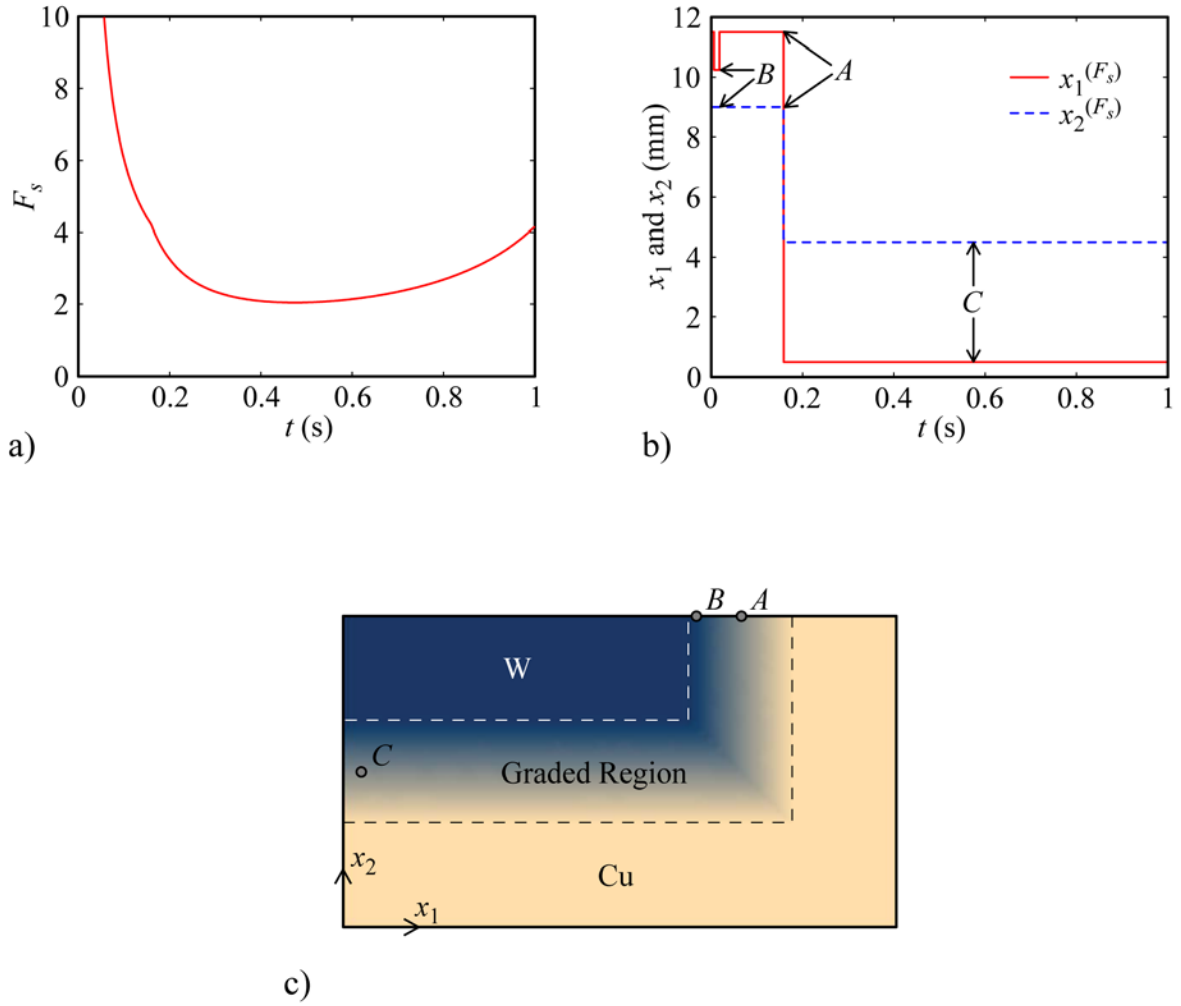
Figure 5.10. Transient factor of safety F_s, coordinates of critical location for the W/Cu functionally graded beam and a graphical depiction of critical locations.

beam changes as function of time. The minimum factor of safety occurs at point A from $0 < t < 0.008$ s as well as 0.016 s $< t < 0.154$ s and it changes to point B at instants 0.008 s $< t < 0.016$ s. The critical locations are shown graphically in Figure 5.10(c). The location of the minimum factor of safety $F_s = 2.05$ at $t = 0.475$ seconds occurs at $x_1 = 0.5$ mm, $x_2 = 4.5$ mm which is denoted as point C in Figure 5.10(c). The volume fractions at point C are $V_W = V_{Cu} = 0.5$ which correspond to the checkerboard microstructure of Figure 5.8(d).
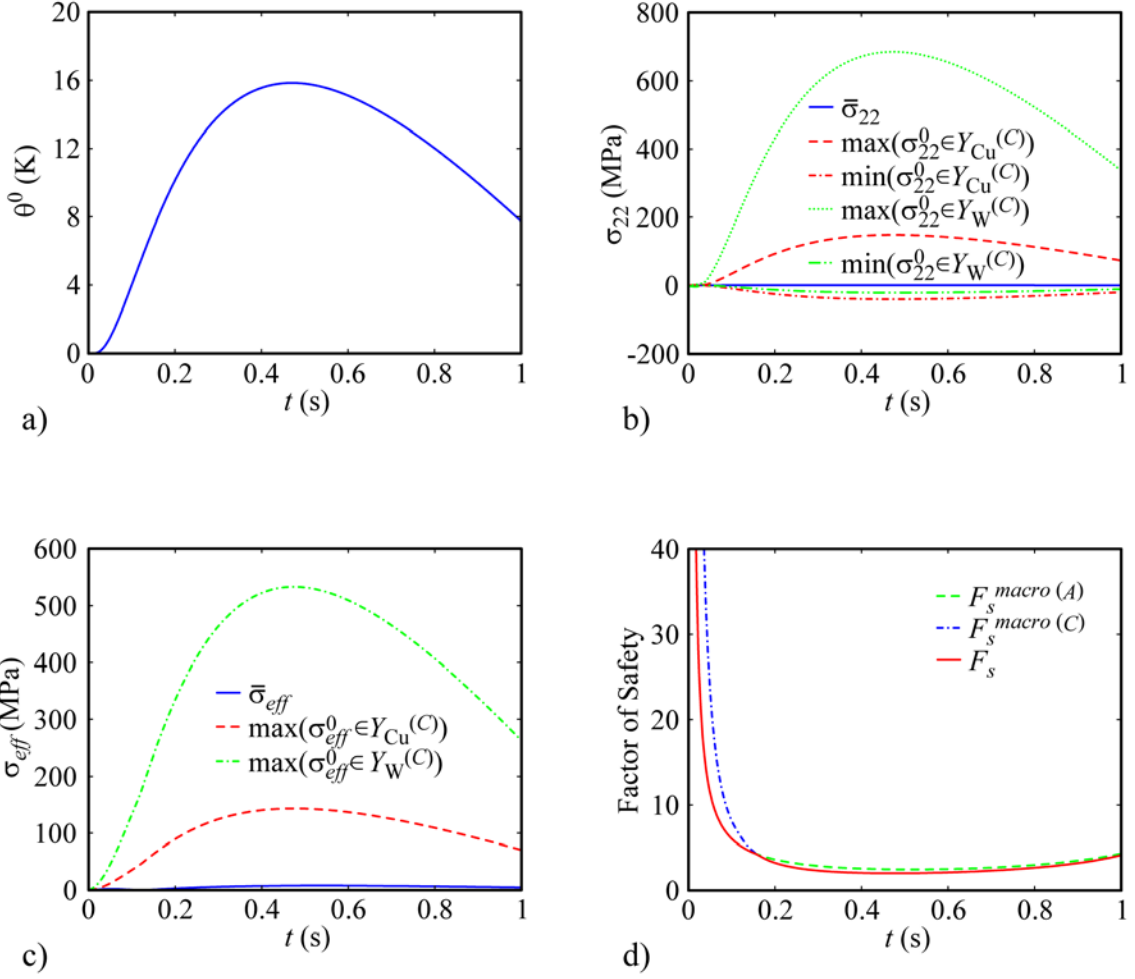
Figure 5.11. Various field variable trends at the critical location C. Shown quantities include a) transient temperature, b) transient average stress $\bar{\sigma}_{22}$ and corresponding minimum and maximum microstress components, c) transient average effective stress $\bar{\sigma}_{eff}$ and corresponding maximum microstress components and d) factor of safety F_s^{macro} at A and C vs. the factor of F_s.

To further emphasize the wealth of information provided by a multiscale analysis, transient trends at the critical location C are presented in Figure 5.11. Figure 5.11(a) shows the temporal variation of the temperature at point C. Figures 5.11(b) and (c) depict the macroscopic, or averaged stress component $\bar{\sigma}_{22}$ and von Mises stress $\bar{\sigma}_{eff}$, respectively, along with the minimum and maximum corresponding microstress component in the respective copper and tungsten microstructure domains Y_{Cu} and Y_{W}. Figure 5.11(d) shows the factor of safety curve of Figure 5.10(a) along with

97

the curve for F_s^{macro} for points A and C. Referring to Figures 5.11(b) and (c), it is clear that the maximum and minimum microstress components occurring over the microstructure can be much larger than their corresponding macroscopic counterpart. In addition, one can conclude from Figures 5.11(a)-(c) that the macroscopic temperature variation has a significant influence on the microstresses as the microstress magnitudes are approximately proportional to the temperature increase θ^0 for this particular thermoelastic multiscale problem. It is also evident from the figures that stress concentrations in the checkerboard microstructure at this location magnify the peak microstress components a great deal as the macroscopic temperature and stress components are all relatively small while the peak microstresses are very large. More specifically, the peak von Mises microstress component in the tungsten phase is 533.9 MPa while the corresponding macroscopic von Mises stress at the same time t is only 8.14 MPa. A further point which should be emphasized is that even though the W/Cu component is in a state of plain stress at the macroscopic level, and hence $\bar{\sigma}_{33} = 0$ for all time, the microstress components σ_{33}^0 need not be zero. During the transient, the maximum microstress component σ_{33}^0 in the tungsten and copper phases reaches 239.6 MPa and 31.6 MPa, respectively. Lastly, the factor of safety F_s^{micro} at point C at $t = 0.475$, as well as two corresponding microstress components, are plotted over the entire microstructure in Figure 5.12. Figure 5.12(a) depicts the variation of σ_{11}^0 over the microstructure, the peak value being 563.0 MPa. The microstress component σ_{12}^0 is plotted over the microstructure in Figure 5.12(b). In both Figures 5.12(a) and (b), it is evident that the sharp phase material interfaces created by the checkerboard pattern microstructure give rise to very significant stress concentrations in the microstress fields. As can be seen in Figure 5.12(c), the factor of safety F_s^{micro} is small in very localized regions and is much larger for a majority of the microstructure which is logical in light of the stress fields given in Figures 5.12(a) and (b). This indicates that as the macroscopic loads are increased beyond the point
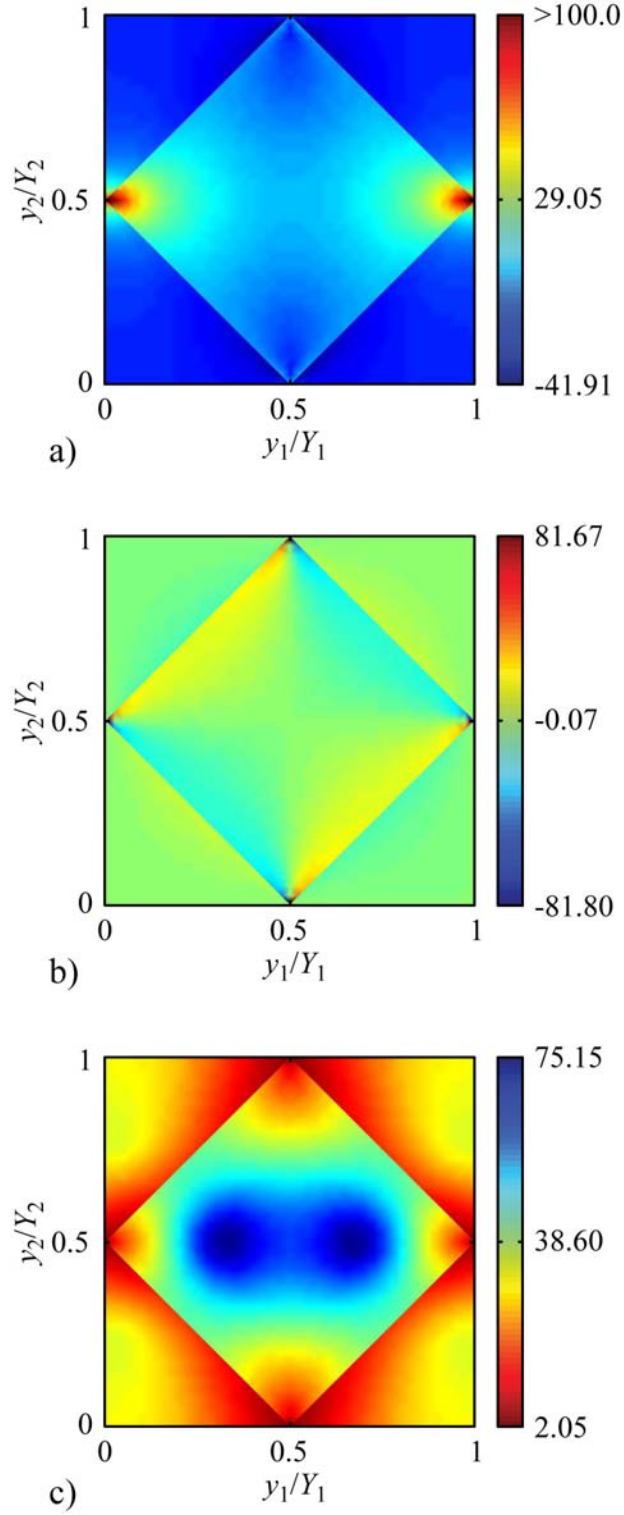
Figure 5.12. Distribution of field quantities over the microstructure at the critical location C at $t = 0.475$ s. Shown are a) microstress σ_{11}^0 in MPa, b) microstress σ_{12}^0 in MPa and c) factor of safety F_s^{micro}.

99

where the minimum of F_s^{micro}, that is F_s^{macro}, is equal to 1.0, yielding and damage will occur only in very small regions of the microstructure. This indicates that the methodology presented here is rather conservative and that at loads which give rise to a F_s^{macro} less than 1.0, the two-phase microstructures are likely to still exhibit a significant amount of additional load carrying capacity.

5.3.2 Failure Analysis of a Ti/ZrO$_2$ Functionally Graded Material Turbine Blade

The second model problem considered in this work is a Ti/ZrO$_2$ functionally graded turbine blade component. This model problem incorporates a range of additional complexities including a more realistic component geometry, microstructures which closely resemble actual random heterogeneous materials and lastly, phase materials with temperature dependent material properties. A schematic of the geometry, loading and grading architecture for the turbine blade is given in Figure 5.13(a). The turbine blade grading consists of a monolithic outer 0.5 mm layer of zirconia, a titanium inner core surrounding each of the three inner cooling channels with a minimum thickness of 0.5 mm, and a linear variation of the volume fraction V_{ZrO_2} between the two monolithic regions computed using the distance fields method (Biswas *et al.*, 2004). As for the thermal loading, the inner surfaces are held at the reference temperature of 300 K ($\theta = 0$ K) and the temperature of the outer surface is prescribed to increase rapidly by 100 K as follows

$$\theta^0(t) = 100 \left(1 - e^{-10t}\right) \text{ K}, \ t > 0. \tag{65}$$

The blade, which is assumed to be in a state of plane stress at the macroscale, is analyzed using a mesh of 2414 LST finite elements as shown in Figure 5.13(b). The time step utilized in the time integration scheme is $\Delta t = 0.005$ seconds.

For the second model problem, a more complex MDF is employed to create the microstructure morphologies. More specifically, a particular choice of random MDF borrowed from Section 3.1, is used which creates realistic microstructures across the

$\theta^0(t) = 100(1\text{-}e^{-10t})$ K, t > 0

30°

$\theta^0 = 0$ K

0.0602 m

x_2

V_{ZrO_2}

0   0.5   1

x_1

60°
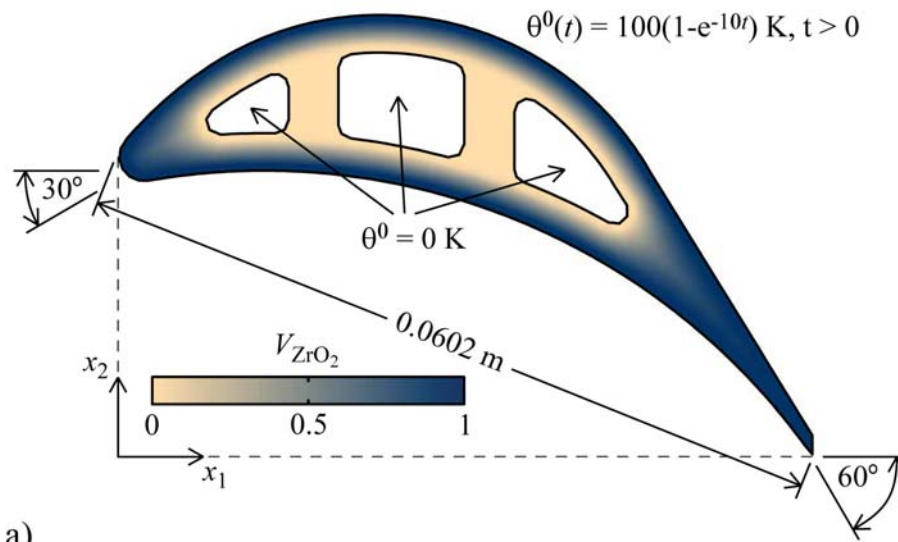
a)
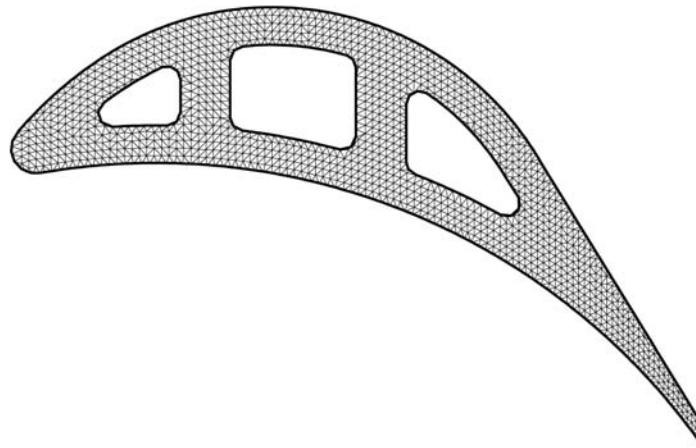
b)

Figure 5.13. Schematic of loading, boundary conditions and volume fraction distribution for a Ti/ZrO$_2$ turbine blade and corresponding finite element mesh.
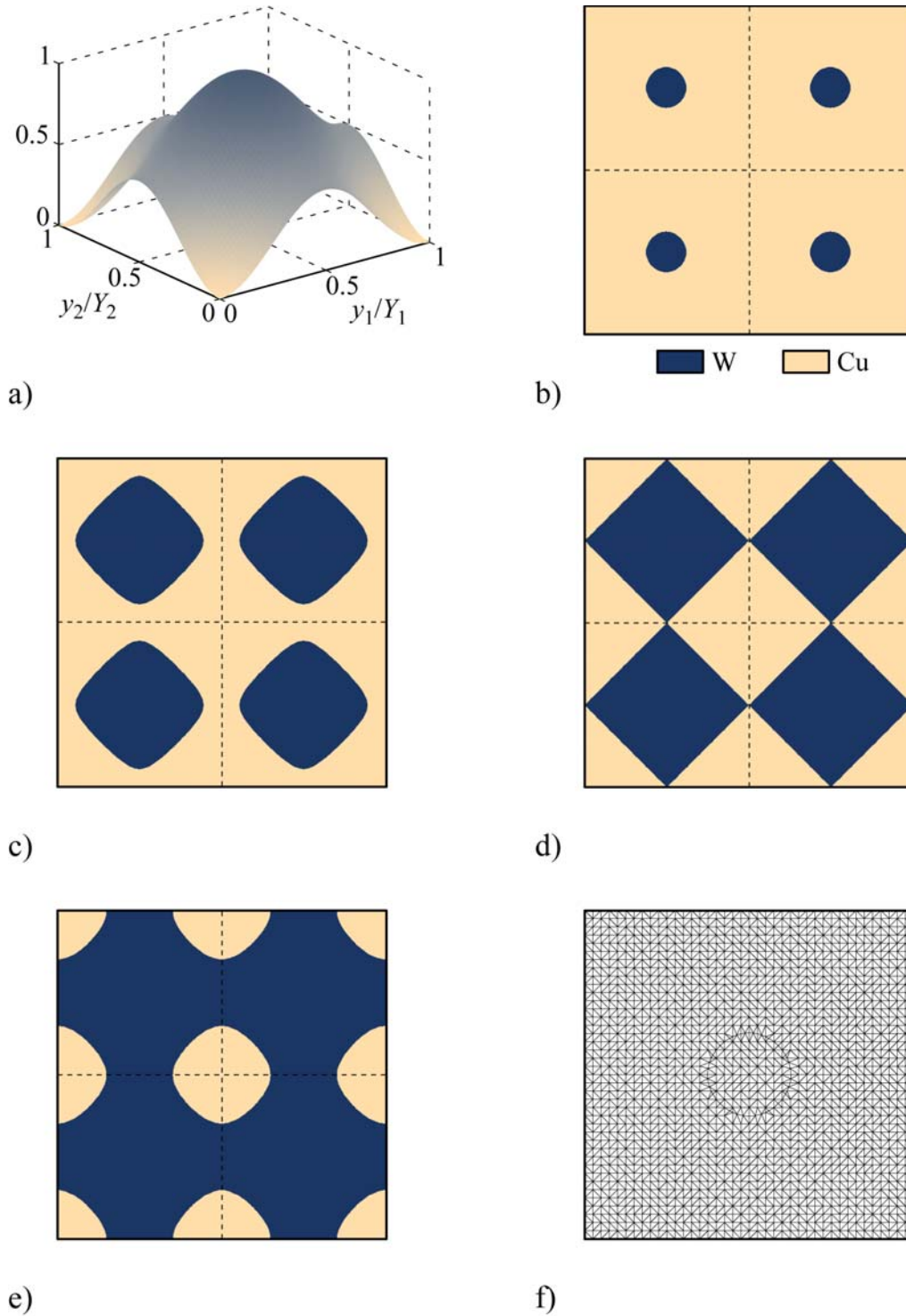
101
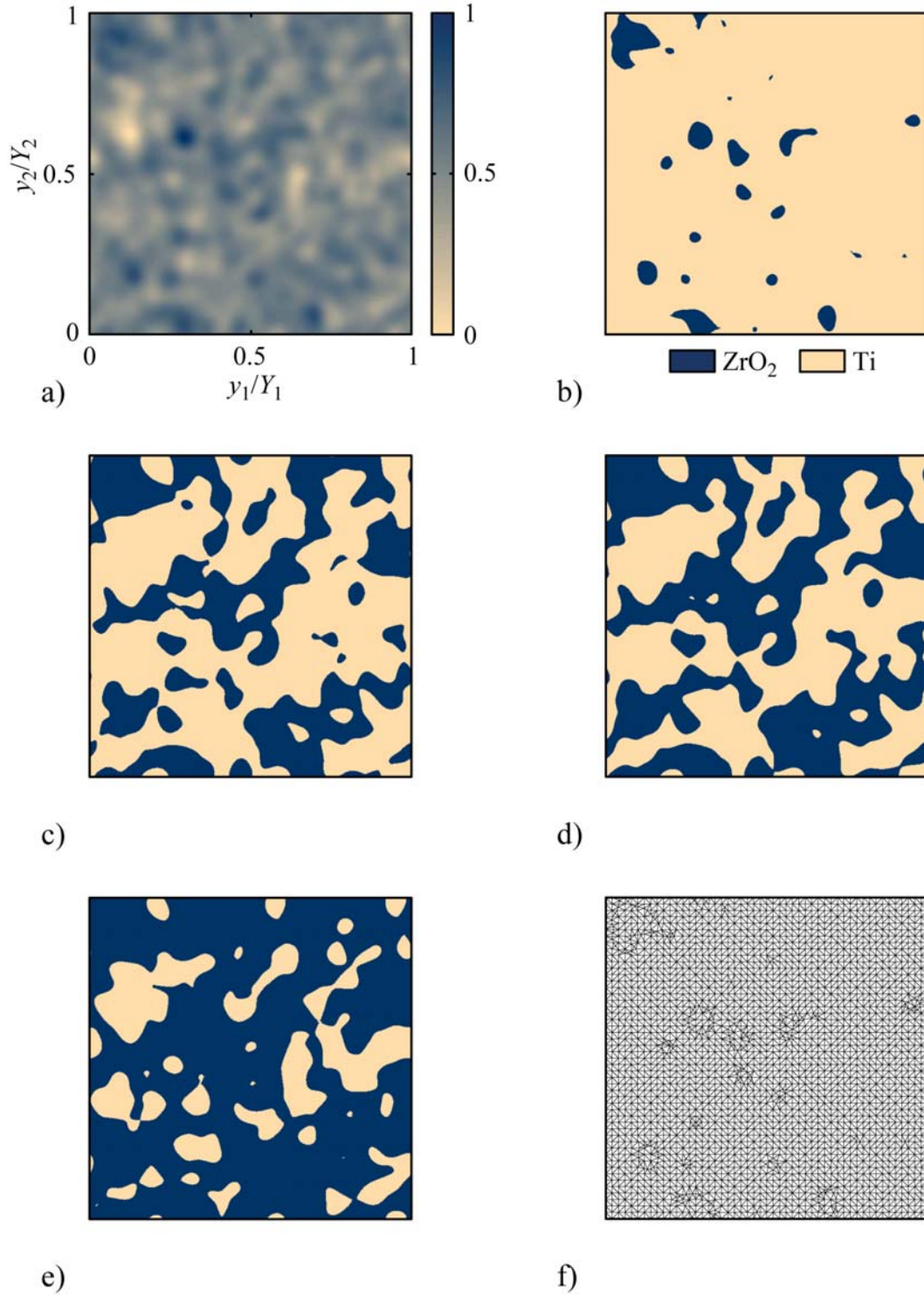
Figure 5.14. Microstructure morphology and analysis mesh used for Ti/ZrO$_2$ heterogeneous material. Shown are a) random morphology description function, b)-e) morphologies for volume fractions of $V_{\text{ZrO}_2} = 0.05$, 0.4, 0.5 and 0.75 respectively and f) finite element mesh for $V_{\text{ZrO}_2} = 0.05$.

entire volume fraction spectrum. The random MDF used in the present model problem is

$$\bar{f}(\mathbf{y}) = \sum_{i=1}^{800} c_i e^{-800\left[\frac{\left(y_1-y_1^{(i)}\right)^2+\left(y_2-y_2^{(i)}\right)^2}{\ell^2}\right]}, \qquad (66)$$

where the coefficients $c_i \in [-1, 1]$ and locations $(y_1^{(i)}, y_2^{(i)}) \in Y$ are chosen randomly. The MDF $\bar{f}(\mathbf{y})$ is normalized to lie in the range 0 to 1 to create the modified MDF $f(\mathbf{y})$ and is shown in Figure 5.14(a). By varying the cutoff f_o, a variety of realistic microstructures can be created, as evidenced by the morphologies shown in Figures 5.14(b)-(e). For cases when the phase volume fractions are quite distinct, a particulate in matrix microstructure arises as seen in the morphologies of Figures 5.14(b) and (e). When the volume fractions are similar in magnitude as they are in Figure 5.14(d), an interconnected skeletal microstructure is created with no distinct matrix or particulate phases, known as an interpenetrating phase composite (e.g. see (Wegner and Gibson, 2001; Feng et al., 2004)). The Ti/ZrO$_2$ microstructures are analyzed using approximately $5,000$ to $6,000$ LST elements depending on microstructural intricacy, an example mesh of which is shown for the $V_{\text{ZrO}_2} = 0.05$ microstructure of Figure 5.14(b) in Figure 5.14(f). The material properties for the titanium and zirconia phases are temperature dependent and are given in Table 5.4. The homogenized thermoelastic properties at three different temperatures for the Ti/ZrO$_2$ random composite obtained via the AEH method are given in Figure 5.15.

A transient multiscale analysis of the Ti/ZrO$_2$ functionally graded turbine blade with random microstructures of Figure 5.14 yields the macroscopic temperatures, displacements, average stresses and microstresses. A direct micromechanical failure analysis is performed to obtain the minimum factor of safety over the domain. As can be seen in Figure 5.16(a), the factor of safety F_s drops rapidly to a value of approximately 5 within the first half a second and then continues to gradually decrease as the steady state is approached. A near steady state factor of safety value of $F_s = 2.72$ is ob-

Material Property	Ti	ZrO$_2$
κ (W/mK)	$1.1 + 0.017T$	$1.71 + 0.21 \times 10^{-3}T$ $+0.116 \times 10^{-6}T^2$
E (GPa)	$122.7 - 0.0565T$	$132.2 - 50.3 \times 10^{-3}T$ $-8.1 \times 10^{-6}T^2$
ν	$0.2888 + 32 \times 10^{-6}T$	0.333
α ($10^{-6}/K$)	$7.43 \times 10^{-6} + 5.56 \times 10^{-9}T$ $-2.69 \times 10^{-12}T^2$	$13.31 \times 10^{-6} - 18.9 \times 10^{-9}T$ $+12.7 \times 10^{-12}T^2$
ρ (kg/m^3)	$4,420.0$	$5,700.0$
C_v (J/kgK)	$350.0 + 0.878T - 0.974 \times 10^{-3}T^2$ $+0.443 \times 10^{-6}T^3$	$274.0 + 0.795T$ $-0.619 \times 10^{-3}T^2$ $+0.171 \times 10^{-6}T^3$
S_y (MPa)	$1,252.0 - 0.8486T$	$-$
S_{ut} (MPa)	$-$	$148.1 + 1.184 \times 10^{-3}T$ $-31.4 \times 10^{-6}T^2$
S_{uc} (MPa)	$-$	$3,181.2 + 25.43 \times 10^{-3}T$ $-0.675 \times 10^{-3}T^2$

Table 5.4. Material properties for functionally graded turbine blade, T in Kelvin.

tained at the end of the analysis at $t = 10.0$ s. Referring to Figure 5.16(b), which shows the coordinates of the critical location in the blade as a function of time, it is noted that the critical location varies within the functionally graded component up until $t = 0.820$ s at which point the location $x_1 = 42.5$ mm, $x_2 = 16.4$ mm (which will be denoted as point D) becomes the critical location for the remainder of the transient. At $t = 0^+$, the critical location occurs within the outer monolithic zirconia layer of the turbine blade. At $t = 0.055$ s, the critical location moves into the graded region of the blade and transitions from the $V_{\text{ZrO}_2} = 1.0$ outer monolithic layer through successively smaller zirconia volume fractions before coming to rest at the aforementioned point D which has a volume fraction of $V_{\text{ZrO}_2} = 0.53$. The trajectory of the critical location is shown graphically in Figure 5.16(c).
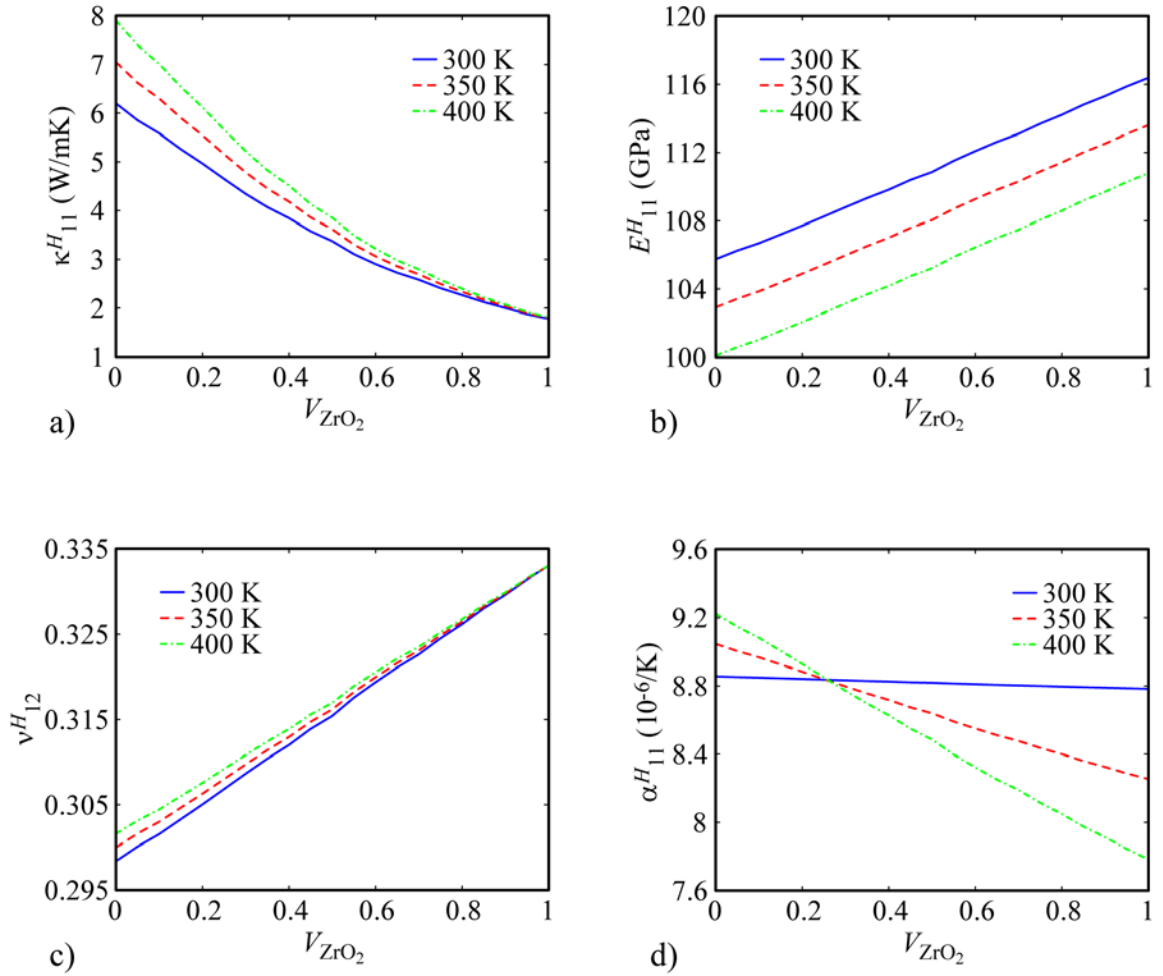
Figure 5.15. Homogenized material properties for the Ti/ZrO_2 microstructures as a function of $VZrO_2$. Properties shown are a) thermal conductivity, b) Young's and shear moduli, c) Poisson's ratio and d) thermal expansion.

For further analysis, detailed transient information is given for point D in the functionally graded turbine blade and is presented in Figure 5.17. Figure 5.17(a) shows the transient temperature change θ^0 at point D which monotonically increases with a near steady-state value of 64.42 K at $t = 10.0$ s. Transient stress profiles are given in Figures 5.17(b) and (c). Figure 5.17(b) depicts the variation of the macroscopic component $\bar{\sigma}_{11}$ at D as a function time t as well the corresponding maximum and minimum microstress components σ^0_{11} in the titanium and zirconia phases of the microstructure. The maximum macroscopic stress $\bar{\sigma}_{11}$ occurs during the transient at
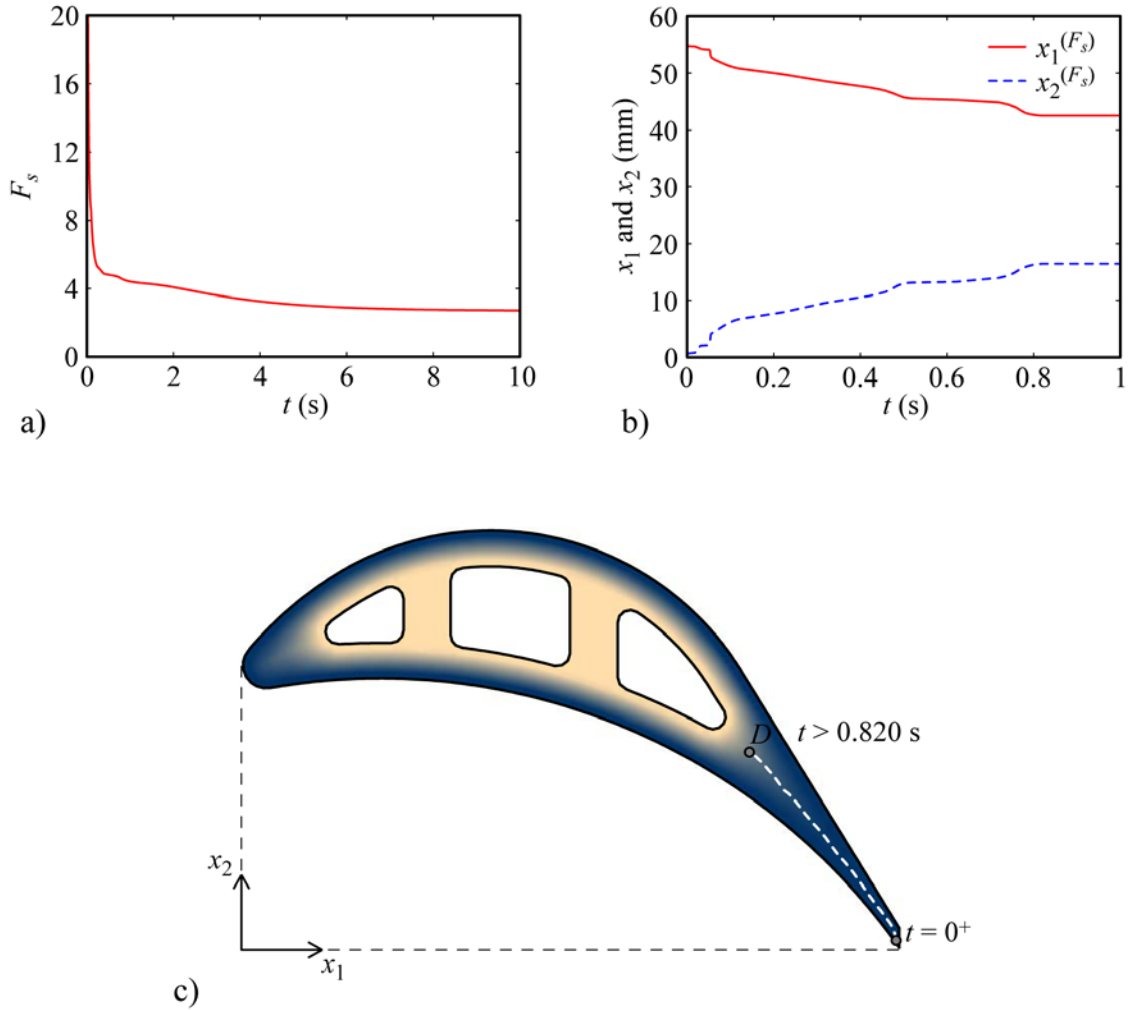
Figure 5.16. Transient factor of safety F_s, coordinates of critical location for the Ti/ZrO$_2$ functionally graded turbine blade and graphical depiction of critical location trajectory.

$t = 1.00$ s with a value of 12.01 MPa. However, with the exception of the curve for the maximum σ_{11}^0 in the titanium phase, the magnitude of the three other microstress is largest at the steady state, which is also the case for the maximum temperature change value θ^0, as discussed previously. This indicates that the temperature increase θ^0 is the dominant influence on the microstress components. To help quantify the effect of temperature increase on microstress magnitude, it is noted that at $t = 1.00$ s $\theta^0 = 8.02$ K and the peak microstress component σ_{11}^0 in the entire microstructure at D is 18.47 MPa yielding a peak stress concentration factor of $\max(\sigma_{11}^0)/\bar{\sigma}_{11} = 1.54$.
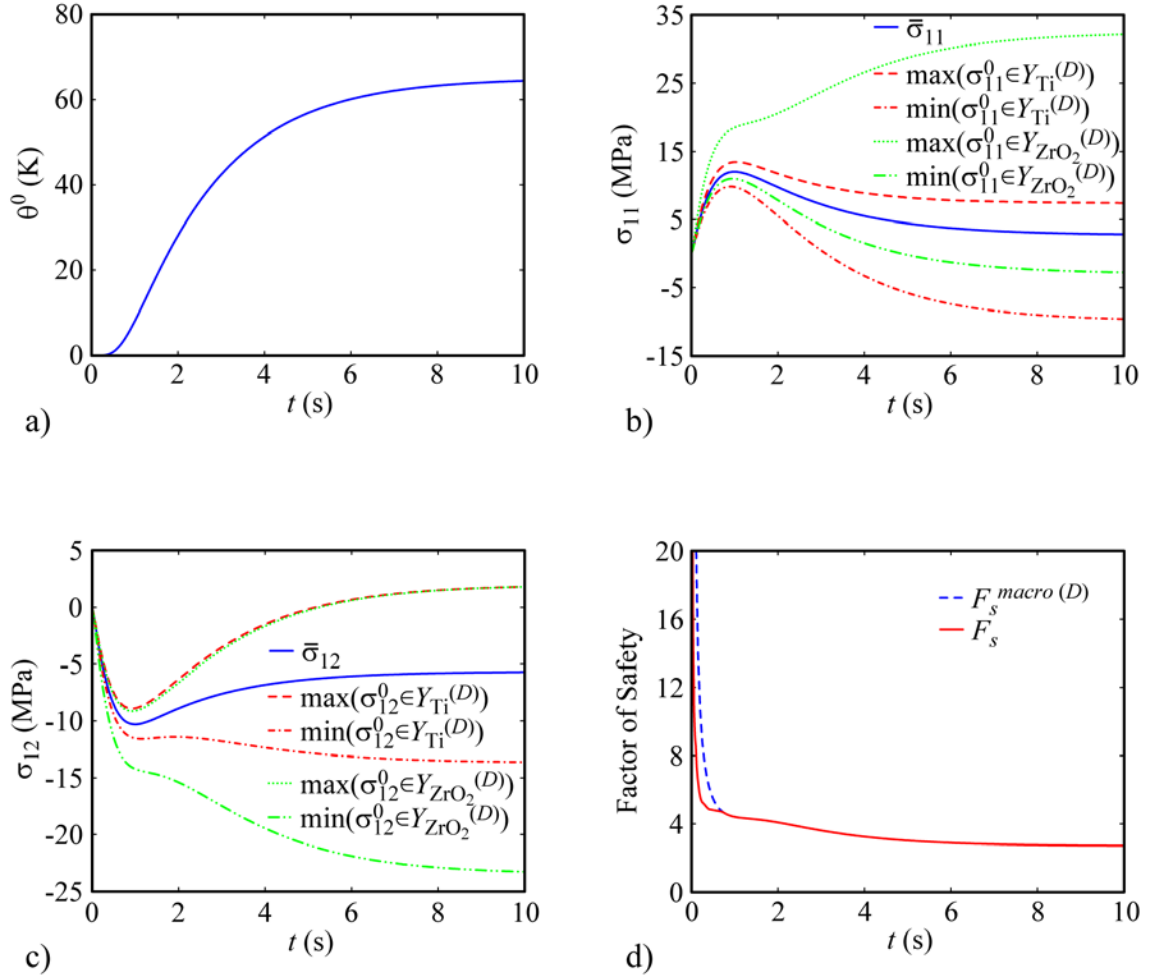
Figure 5.17. Various field variable trends at the critical location D. Quantities shown include a) transient temperature, b) transient average stress $\bar{\sigma}_{11}$ and corresponding minimum and maximum microstress components, c) transient average stress $\bar{\sigma}_{12}$ and corresponding minimum and maximum microstress components and d) factor of safety F_s^{macro} at C vs. the factor of safety F_s.

At $t = 10.0$ s, where $\theta^0 = 64.42$ K at D, which is 8.03 times the value at $t = 1.00$ s, the peak stress concentration factor is also increased by approximately a factor of eight with the value $\max(\sigma_{11}^0)/\bar{\sigma}_{11} = 11.33$. The importance of increase in temperature from the reference state on the microstress component magnitudes is also borne out in Figure 5.17(c) which shows the transient macroscopic stress $\bar{\sigma}_{12}$ at D and the corresponding minimum and maximum microstress components σ_{12}^0 in both material phases of the microstructure. In Figure 5.17(c), similar to the trends in 5.17(b), the variation between the maximum and minimum microstress components and the averaged or macroscopic stress increases approximately in proportion to the magnitude of the temperature difference θ^0. However, while θ^0 has a significant impact on the microstress magnitudes and hence, the failure of the two-phase material, it is not the only factor. There are large areas of the turbine blade of Figure 5.13(a) with higher temperatures than point D during the transient and steady-state in the graded region, however, it is point D that is the critical location in the body as shown by the comparison of the factor of safety F_s and factor of safety F_s^{macro} at point D in Figure 5.17(d). This indicates that while temperature increase θ^0 is an important factor influencing failure of the two-phase material, microstructural morphology is also of great importance. Figure 5.18 shows two of the microstress components, namely σ_{22}^0 and σ_{33}^0, as well as the factor of safety F_s^{micro} over the microstructure at the critical location D at $t = 10.0$ s. The microstress component σ_{22}^0 in Figure 5.18(a) exhibits a complex variation with a number of local stress concentrations. The microstress component σ_{33}^0 shown in Figure 5.18(b), however, is not as complex. Nonetheless, σ_{33}^0 is significant in magnitude even though the macroscale problem is being analyzed in state of plane stress. The F_s^{macro} value at the macroscopic location D at $t = 10.0$ s is 2.72, as noted earlier as can be seen by the minimum value of the F_s^{micro} plot given in Figure 5.18(c). It is also worth noting in Figure 5.18(c) that the zirconia regions of the random microstructure possess low factors of safety F_s^{micro}
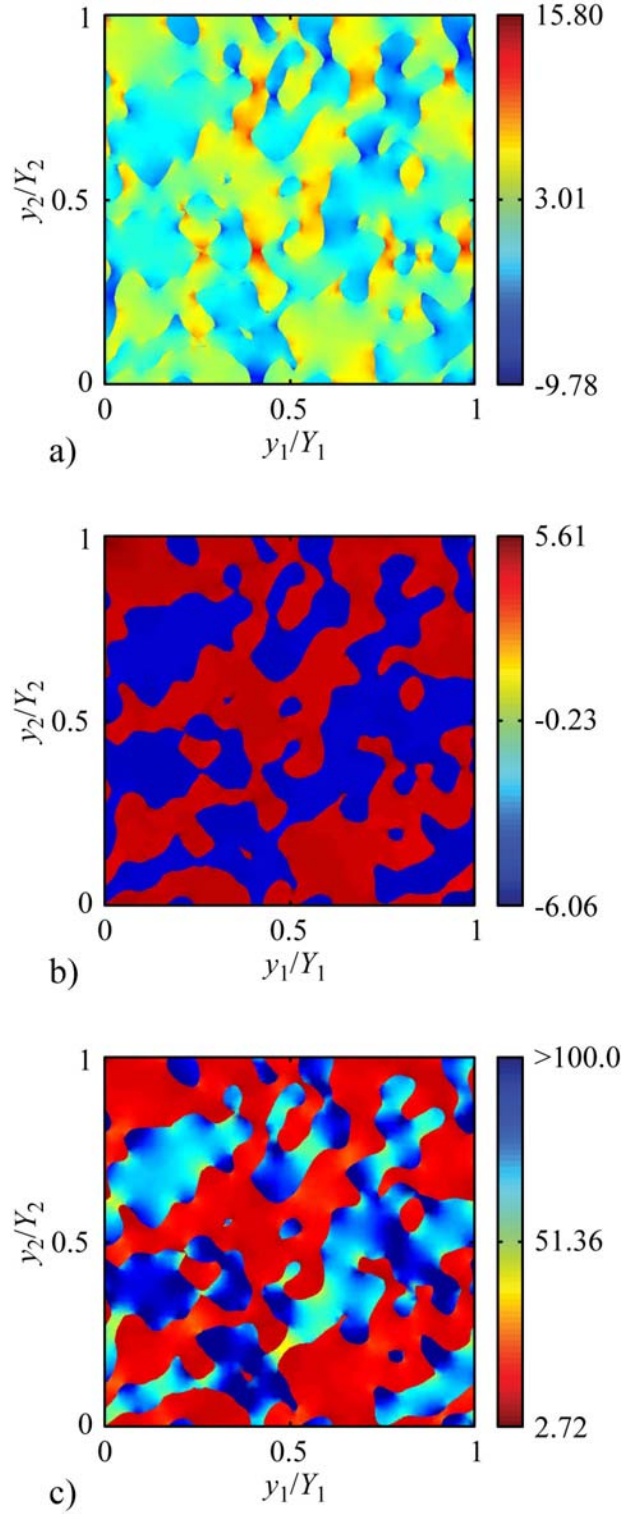
Figure 5.18. Distribution of field quantities over the microstructure at the critical location D at $t = 10.0$ s. Shown are a) microstress σ_{22}^0 in MPa, b) microstress σ_{33}^0 in MPa and c) factor of safety F_s^{micro}.

whereas the regions of titanium material exhibit significantly higher factors of safety, indicating that the zirconia is the critical phase for the conditions at point D.

The multiscale analysis reveals that the combination of the moderately high temperature θ^0, microstructural morphology and, to a lesser extent, the macroscopic stress state create a critical location in the turbine blade at point D where F_s^{macro} is a minimum. The multiscale approach presented here provides detailed information about the macroscopic and microscopic stresses and enables a direct micromechanical failure analysis, which is invaluable in analysis and design applications.

CHAPTER 6

THE ROLE OF ROCK FABRIC IN SEISMIC WAVE SPEED ANISOTROPY

In this chapter, the role of key rock fabric features on seismic wave speed anisotropy is investigated. Recall from Chapter 1 that the concept of seismic anisotropy essentially indicates an existence of a wave speed velocity dependence on propagation direction. To begin the investigation, parametrized, synthetic quartz/muscovite rock fabric microstructures are created and their wave speed velocities are determined using homogenized elastic stiffnesses obtained via the AEH method. The AEH stiffness derived wave speeds for polycrystalline rock fabrics, such as the one shown in Figure 6.1, are compared to wave speed velocities determined from analytic homogenization schemes commonly used in the geophysical community. Lastly, a parametric study is performed using the synthetic rock fabric microstructures in order to determine the influence of rock fabric features on seismic wave speed anisotropy.

6.1 Analytic Bounds and Estimates

Primarily for comparison purposes, a few of the common homogenization bounding methods and analytic estimation methods are presented here. These include the Voigt (1928) (upper) and Reuss (1929) (lower) bounds as well as the geometric (Matthies and Humbert, 1993) and arithmetic (Hill, 1952) mean, the formulae for which are presented in the remainder of this section.

To compute the Voigt bound it is assumed that the strain is constant throughout the entire microstructural domain Y, which of course, is not true in general. Nonetheless, the result is that the homogenized elastic constants are essentially the volume averaged elastic constants of the rock fabric constituents. Expressed in integral form, the Voigt bound C_{ijkl}^V is
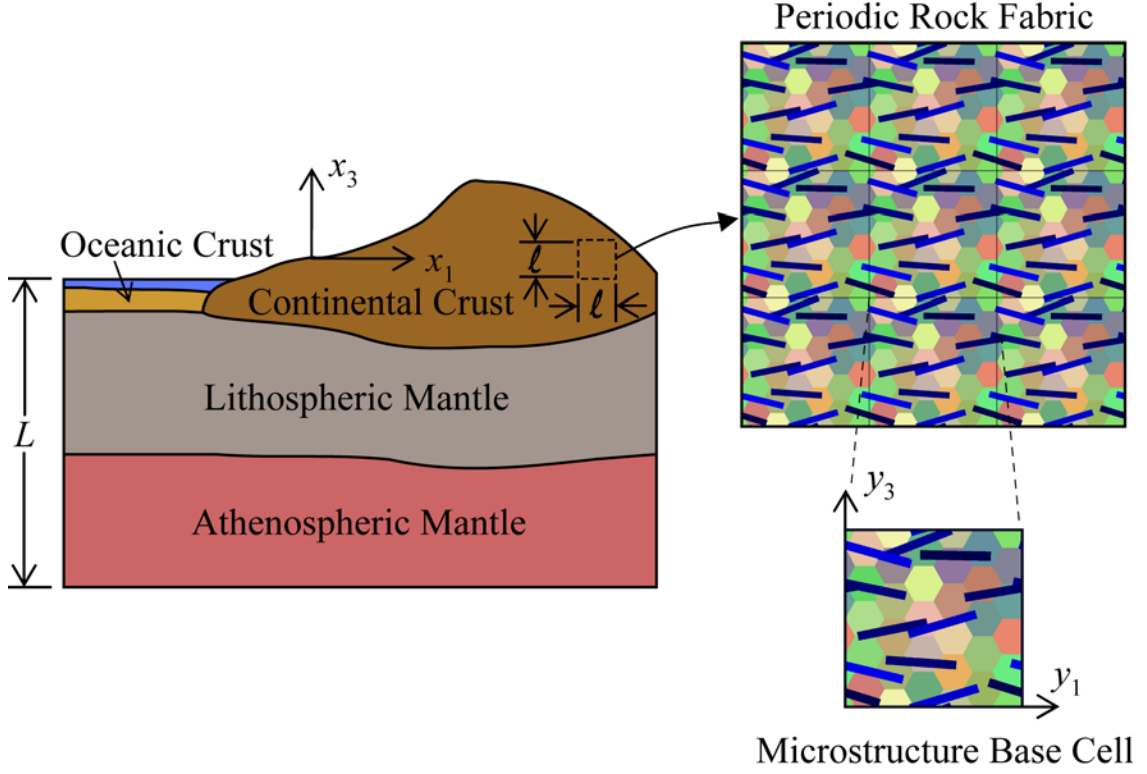
Figure 6.1. Schematic of relationship between macroscale, periodic rock fabric and microstructure base cell.

$$C_{ijkl}^V = \frac{1}{|Y|} \int_Y C_{ijkl}^\varepsilon dY, \tag{67}$$

where C_{ijkl}^ε are the spatially varying elastic stiffnesses and $|Y|$ is the volume of the microstructural domain. Conversely, the Reuss bound assumes that the stress is constant throughout the entire microstructural domain which is also unlikely in most physically realistic cases. However, assuming an isostress state, the Reuss bound C_{ijkl}^R is computed with the formula

$$C_{ijkl}^R = \left(\frac{1}{|Y|} \int_Y S_{ijkl}^\varepsilon dY \right)^{-1}, \tag{68}$$

where $S_{ijkl}^\varepsilon = C_{ijkl}^{\varepsilon-1}$ are the spatially varying compliances within the rock fabric microstructure. As the Voigt and Reuss estimates represent the respective upper and lower bounds of the homogenized elastic constants, it stands to reason that a sim-

plistic means of obtaining a better estimate between the bounds is to simply average them. The average of C_{ijkl}^V and C_{ijkl}^R yields the arithmetic mean C_{ijkl}^{VRH}, also known as the Voigt-Reuss-Hill estimate. It should be noted, however, that there is no legitimate mathematical justification for performing this averaging scheme (*e.g.* see (Mainprice and Humbert, 1994)). The last estimate to be discussed is the geometric mean which imposes the constraint that homogenized elastic stiffnesses be equal to the inverse of the homogenized elastic compliances, which is not true in the instance of the Voigt and Reuss bounds, for example. Computation of the geometric mean in contracted notation, D_{PQ}^G, is performed as follows:

$$
\mathbf{D}^G = e^{\left[\frac{1}{|Y|}\int_Y \ln(\mathbf{D}^\varepsilon)\, dY\right]},
\tag{69}
$$

where D_{PQ}^ε is the the 6×6 engineering contracted form of C_{ijkl}^ε and $e^{(\cdot)}$ and $\ln(\cdot)$ indicate the matrix exponential and matrix logarithm, respectively (*e.g.* see (Horn and Johnson, 1999)). As expected, the geometric mean lies between the upper and lower bounds. However, like all of the other estimates presented in this section, the geometric mean depends only on the relative volume fraction and orientation of the polycrystals comprising the rock fabric and has no means to account for the elastic interplay between polycrystals. AEH, on the other hand, does account for this effect which can have a significant influence on the homogenized elastic constants computed, and hence, the wave speed velocities traveling through the bulk rock.

6.2 Computation and Characterization of Seismic Anisotropy

In this section, the determination of the three wave speed velocities in an unbounded rock media is presented first. Subsequently, measures of seismic anisotropy are presented which help characterize the dependence of the wave speed velocities on propagation direction.

6.2.1 Wave Propagation in Unbounded Media

The details of computing the wave speed velocities in the homogenized anisotropic rock media are now outlined. For the purposes of this work, a solution is sought for wave speeds in unbounded media, which is common when studying waves propagating through Earth's crust where the wavelength is much larger than the geologic feature. In this scenario it is common to represent the rock fabric as a homogenized media, which as mentioned previously, is the case in this work. One begins the process of determining the wave speeds with the equations of motion written in terms of the macroscopic displacements and homogenized material properties, which is

$$C_{ijkl}^H \frac{\partial^2 u_k^{(0)}}{\partial x_l \partial x_j} = \rho^H \frac{\partial^2 u_i^{(0)}}{\partial t^2}. \tag{70}$$

A plane wave solution is sought for (70) and is of the form

$$u_i^{(0)}(\mathbf{x}, t) = a_i f\left(t - \frac{n_j x_j}{V}\right), \tag{71}$$

where a_i are displacement amplitudes, n_i are components of the unit vector that defines the direction of wave propagation at the speed V and $f(\cdot)$ is an arbitrary function that defines the wave form. Inserting (71) into (70) and noting that the second derivative of $f(\cdot)$ need not be zero as $f(\cdot)$ is arbitrary eventually leads to the Christoffel equation (Christoffel, 1877),

$$\left[C_{ijkl}^H n_j n_l - \rho^H V^2 \delta_{ik}\right] a_k = 0, \tag{72}$$

where δ_{ik} is the Kronecker delta. The Christoffel equation (72) represent an eigenvalue problem where $\rho^H V^2$ are the eigenvalues and a_k are the corresponding eigenvectors, also called polarization vectors. The solution of (72) (*e.g.* see (Auld, 1990)) yields three real eigenvalues, and hence, three real wave speeds V, one P-wave whose normalized eigenvector is similar to the propagation direction and two, typically smaller magnitude S-waves with polarization directions approximately orthogonal

114

to the propagation direction. For the purposes of this work, the P-wave will be denoted as V_P and the two S-waves as $V_{S1} \geq V_{S2}$.

6.2.2 Measures of Seismic Anisotropy

Once the homogenized elastic stiffnesses have been obtained, the investigation of seismic anisotropy in rock fabrics can be conducted. Recall that the concept of seismic anisotropy is the phenomena where the wave speed velocities are dependent on the propagation direction $\mathbf{n}$. In addition to studying the effects of varying $\mathbf{n}$ on the various wave speeds V directly other seismic anisotropy measures generated from these wave speeds will also be investigated. These measures distill trends found in directional wave speed information into a few simple, easy to understand and physically meaningful quantities which facilitate the study of seismic anisotropy. A brief discussion of the computation and significance of these measures is now presented.

For the results presented in future sections the propagation directions investigated will lie in the $y_1 - y_3$ plane and will be oriented using the incidence angle γ, this being the angle between the propagation direction and the y_3 axis. Thus, $\mathbf{n}$ can be written as

$$\mathbf{n}^T = \left[\begin{array}{ccc} \sin\gamma & 0 & \cos\gamma \end{array} \right]. \tag{73}$$

A schematic of propagation direction is given in Figure 6.2. For use in the proceeding outline, a plot of the three wave speeds as a function of the incidence angle γ are shown in Figure 6.3 for the Haast Schist (Okaya and Christensen, 2002). The bulk elastic stiffness of the Haast Schist, obtained through petrophysical measurements (Okaya and Christensen, 2002) are used to obtain the wave speeds at different incidence angles. The first measure of interest is the P-wave speed anisotropy (Birch, 1960) which is computed using the formula

$$A_P = \frac{\left(V_P^{\max} - V_P^{\min} \right)}{\frac{1}{2} \left(V_P^{\max} + V_P^{\min} \right)} \times 100\%, \tag{74}$$

115
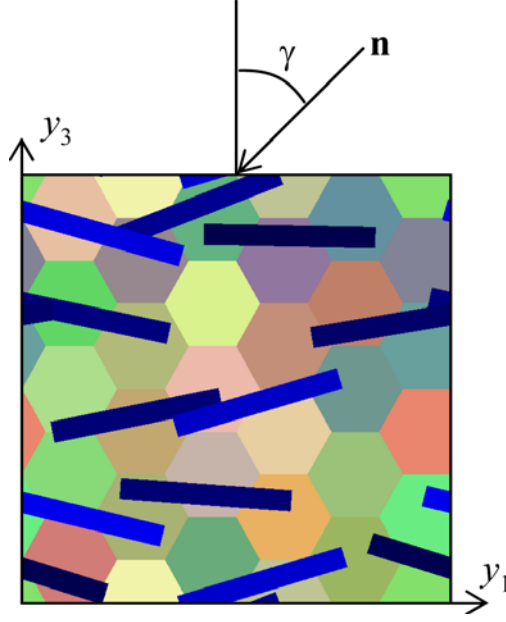
Figure 6.2. Illustration of propagation direction $\mathbf{n}$ as defined by the incidence angle γ.

where $V_P^{\max}$ and $V_P^{\min}$ are the maximum and minimum values of $V_P(\gamma)$ computed over the entire range of angles γ, respectively. For the Haast Schist wave speed plot in Figure 6.3, A_P would be computed using points B ($V_P^{\min}$) and D ($V_P^{\max}$) with a final result of $A_P^{HS} = 12.75\%$. As can be seen in the figure, A_P is a normalized measure of the spread in the possible $V_P(\gamma)$ velocities over the range of incidence angles. For an isotropic material $A_P = 0$, yet, for anisotropic materials, A_P can be quite large depending on the severity of the rock fabric anisotropy. In addition to A_P, a S-wave speed anisotropy, A_S, is also of interest (Birch, 1960). The formula for this seismic wave speed anisotropy measure is

$$A_S = \frac{\left(V_S^{\max} - V_S^{\min}\right)}{\frac{1}{2}\left(V_S^{\max} + V_S^{\min}\right)} \times 100\%, \tag{75}$$

$V_S^{\max}$ being the maximum of $V_{S1}(\gamma)$ (Point F for the Haast Schist of Figure 6.3) and $V_S^{\min}$ being the minimum of $V_{S2}(\gamma)$ (Point E for the Haast Schist of Figure 6.3). Similar to A_P, $A_S = 0$ for isotropic materials. For the Haast Schist, $A_S^{HS} = 16.49\%$. As for other materials, petrophysical data show that crustal foliated rocks such as

116
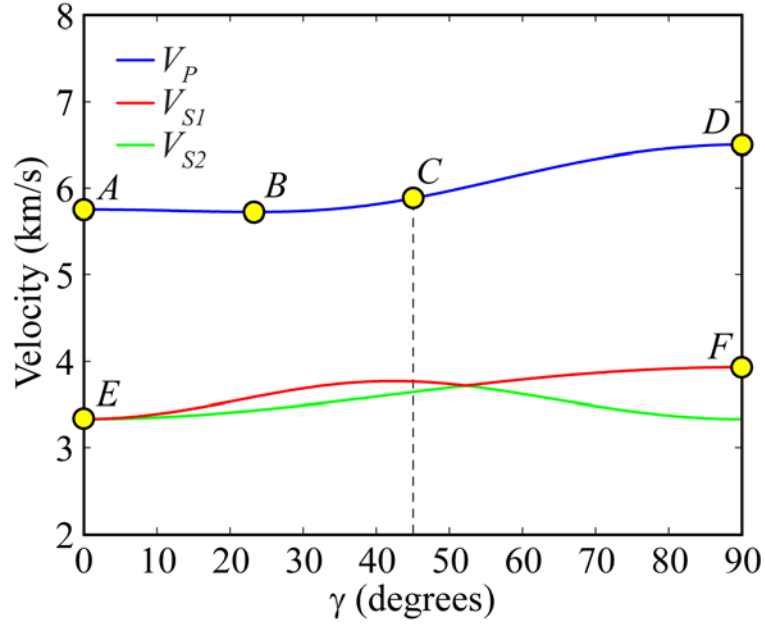
Figure 6.3. Wave speeds for the Haast Schist as a function of incidence angle γ (Okaya and Christensen, 2002).

schists, gneisses and amphibolites can possess A_P as high as 17 to 20% (20.5% for the Poultney slate, Vermont) and A_S as high as 25 to 30% (37.4% for the Poultney slate, Vermont) (Christensen, 1956; Christensen, 1966; Godfrey *et al.*, 2000).

Another seismic anisotropy characteristic of interest to the seismic community is the magnitude of $V_P (45°)$ relative to $V_P (\gamma)$ at $\gamma = 0°$ and at $\gamma = 90°$. This is often termed the V_P-45 effect. It is of interest since $V_P (45°)$ is rarely the average of $V_P (0°)$ and $V_P (90°)$ for real rock fabrics, even though it often assumed to be. To study the V_P-45 effect, a normalized $V_P (45°)$ (Okaya and Christensen, 2002) is computed as

$$\nu_{P45} = \frac{(V_P (45°) - V_P (0°))}{(V_P (90°) - V_P (0°))} \times 100\%, \tag{76}$$

which for the Haast Schist curves in Figure 6.3 would involve points A, C and D. As mentioned previously, $V_P (45°)$ is often assumed to be the average of $V_P (0°)$ and $V_P (90°)$ which would give a ν_{P45} of 50%. As proof that this is not necessarily true for real rock fabrics, the Haast Schist exhibits a normalized ν_{P45} of 17.44%.

117

In addition to the aforementioned measures of seismic anisotropy, two other parameters will also be investigated. The first is termed the P-delay which is computed as

$$\Delta t_P \left(\gamma \right) = \frac{1}{V_P \left(\gamma \right)} - \frac{1}{V_P^{\mathrm{max}}}.$$ (77)

The P-delay quantity computed in (77) has units of time per unit length and measures the delay in time required by a P-wave to travel a unit distance (usually a kilometer) relative to the time the maximum P-wave velocity V_P^{max} takes to cover the same unit distance as a function of incidence angle. The last measure of seismic anisotropy to be investigated is the S-split,

$$\Delta t_S \left(\gamma \right) = \frac{1}{V_{S2} \left(\gamma \right)} - \frac{1}{V_{S1} \left(\gamma \right)},$$ (78)

which also has units of time per unit length. The quantity $\Delta t_S \left(\gamma \right)$ measures the difference in time for the two S-waves to cover a unit distance as a function of incidence angle. As expected, both $\Delta t_P \left(\gamma \right)$ and $\Delta t_S \left(\gamma \right)$ are zero for isotropic materials at all possible angles γ. However, realistic rock fabrics rarely possess isotropic material symmetry and hence display unique trends in the P-delay and S-split curves.

6.3 Creation of Synthetic Quartz/Muscovite Rich Rock Microstructures

As mentioned earlier, the aim of this work is to investigate the effects of rock fabric features on seismic anisotropy. In order to accomplish this task, one might consider analyzing various actual rock fabric microstructure micrographs using image-based meshing and numerical homogenization techniques (*e.g.* see (Langer *et al.*, 2001)). However, it is difficult to thoroughly investigate the entire range of fabric possibilities in this manner. Therefore, in this work, the role of various rock fabric features on seismic wave speed anisotropy is studied using synthetic rock fabric geometries which exhibit the prescribed morphological characteristics. Note that the term synthetic merely indicates that the rock fabric geometries are not copies of actual micrographs,
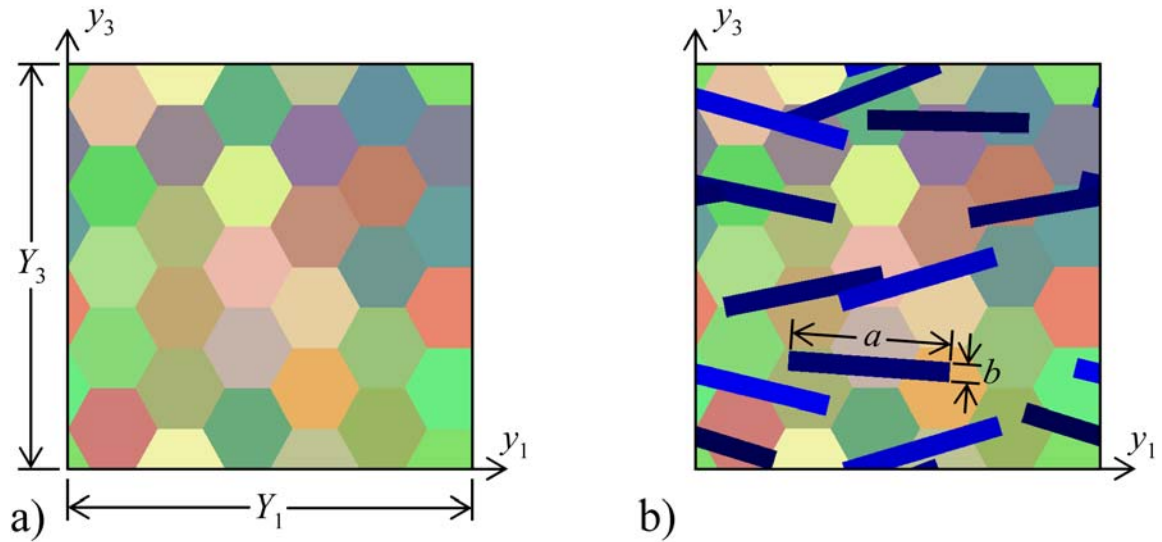
Figure 6.4. Beginning of base cell of sample synthetic microstructure showing grid of quartz crystals and completed synthetic microstructure with rectangular muscovite inclusions yielding a muscovite volume fraction of 0.2.

but are generated automatically by a computer program based on some parameters such as volume fraction and grain orientation.

In order to focus this study, only rock fabrics comprised of quartz and muscovite are considered. Quartz is a trigonal material with mild elastic anisotropy and muscovite is a monoclinic material with strong elastic anisotropy. Muscovite is typically present in sheets with the material axis perpendicular to the plane of the sheet being very compliant relative to the stiffnesses in the plane of the sheet. In an effort to model potentially high anisotropy quartz/muscovite rock fabrics in a simple fashion, synthetic quartz/muscovite rock fabrics are created and parametrized in such a fashion that the only geometry parameters investigated are muscovite volume fraction and muscovite grain orientation distribution. To create the synthetic microstructures, first a background of similarly sized hexagons is placed over the base cell, of length Y_1 and height Y_2, as shown in Figure 6.4(a). These hexagons represent the quartz grains, each with its own particular material orientation. The orientations, which are denoted by varying quartz grain colors, may be all identical or each randomly

119

oriented (as they are in Figure 6.4) in this study. This will allow the exploration of fabrics with essentially an isotropic behaving quartz matrix phase as well as the extremes of highly ordered quartz grains. To complete the microstructure, a series of slender rectangles of length a and thickness b, which represent the muscovite grains, are overlaid at random locations over the grid of hexagons until the desired muscovite volume fraction is achieved as shown in Figure 6.4(b). The muscovite grains are oriented with a mean angle of zero degrees with respect to the y_1 axis plus or minus a given standard deviation angle α. In other words, approximately 68% of the muscovite inclusions are oriented within $\pm\alpha$ of the y_1 axis and over 99% of the inclusions are oriented within $\pm 3\alpha$ of the y_1 axis. For the rock fabric microstructure in Figure 6.4(b), the muscovite volume fraction is $V_M = 0.2$ and the muscovite grain distribution standard deviation parameter is $\alpha = 10.0°$. Note that if $\alpha = 0°$, a planar foliation of the muscovite grains is formed. As for the material orientation of the muscovite, the compliant material axis is always oriented perpendicular to the long axis of the muscovite grain. The other two stiff material axes are randomly oriented about the axis perpendicular to the long axis of the muscovite grain. The color of the grains indicates the angle of rotation of the stiff axes about the aforementioned perpendicular axis from the reference material configuration. Prior to proceeding, it should be noted that the rock fabric geometries created here are periodic as is required by the AEH method. In other words, if the synthetic microstructure is 'tiled' repeatedly to create a larger sample of the microstructure, there is no discontinuity in the geometric features from one instance of the microstructure to another, as shown in Figure 6.1.

The final step in creating a synthetic microstructure that can be homogenized to find the effective elastic constants is to determine the elastic constants of each of the quartz and muscovite grains in the analysis frame $\mathbf{y}$. To begin this process, it is first noted that the orthonormal base vectors of the analysis frame $\mathbf{y}$ are $\mathbf{e}_i^s$. Each crystal

has its own unique material symmetry axis denoted by a separate set of orthonormal base vectors $\mathbf{e}_j^c$. For each crystal the direction cosines a_{ij} are constructed by taking the dot products of the combinations of $\mathbf{e}_j^c$ and $\mathbf{e}_i^s$, i.e.,

$$a_{ij} = \mathbf{e}_i^s \cdot \mathbf{e}_j^c. \tag{79}$$

Since both the crystal and reference base vectors are of unit length, a_{ij} represents the cosine of the angle between the vectors $\mathbf{e}_j^c$ and $\mathbf{e}_i^s$. With a_{ij} computed, the Bond transformation matrix (Bond, 1943) $\mathbf{M}$ can be constructed as

$$\mathbf{M} = \begin{bmatrix} a_{11}^2 & a_{12}^2 & a_{13}^2 & 2a_{12}a_{13} & 2a_{13}a_{11} & 2a_{11}a_{12} \\ a_{21}^2 & a_{22}^2 & a_{23}^2 & 2a_{22}a_{23} & 2a_{23}a_{21} & 2a_{21}a_{22} \\ a_{31}^2 & a_{32}^2 & a_{33}^2 & 2a_{32}a_{33} & 2a_{33}a_{31} & 2a_{31}a_{32} \\ a_{21}a_{31} & a_{22}a_{32} & a_{23}a_{33} & a_{22}a_{33}+a_{23}a_{32} & a_{21}a_{33}+a_{23}a_{31} & a_{22}a_{31}+a_{21}a_{32} \\ a_{31}a_{11} & a_{32}a_{12} & a_{33}a_{13} & a_{12}a_{33}+a_{13}a_{32} & a_{13}a_{31}+a_{11}a_{33} & a_{11}a_{32}+a_{12}a_{31} \\ a_{11}a_{21} & a_{12}a_{22} & a_{13}a_{23} & a_{12}a_{23}+a_{13}a_{22} & a_{13}a_{21}+a_{11}a_{23} & a_{11}a_{22}+a_{12}a_{21} \end{bmatrix}. \tag{80}$$

The Bond transformation matrix is used to obtain the crystal properties in the analysis reference frame $\mathbf{y}$ via the relation

$$D_{PQ}^{\varepsilon} = M_{PR}M_{QS}D_{RS}, \tag{81}$$

where D_{RS} is contracted form of the grain stiffness in its symmetry axis C_{ijkl} and D_{PQ}^{ε} is the stiffness tensor for the grain in the analysis frame $\mathbf{y}$. The contracted notation stiffness tensors used for the quartz and muscovite in this work are (Bass, 1995)

$$\mathbf{D}^{Quartz} = \begin{bmatrix} 86.6 & 12.6 & 6.7 & 17.8 & 0 & 0 \\ & 106.1 & 12.6 & 0 & 0 & 0 \\ & & 86.6 & -17.8 & 0 & 0 \\ & & & 57.8 & 0 & 0 \\ & \text{Sym.} & & & 39.95 & 17.8 \\ & & & & & 57.8 \end{bmatrix} \text{GPa,}$$

$$\mathbf{D}^{Muscovite} = \begin{bmatrix} 184.3 & 48.3 & 23.8 & 0 & -2.0 & 0 \\ & 178.4 & 21.7 & 0 & 3.9 & 0 \\ & & 59.1 & 0 & 1.2 & 0 \\ & & & 16 & 0 & 0.5 \\ & \text{Sym.} & & & 17.6 & 0 \\ & & & & & 72.4 \end{bmatrix} \text{GPa.} \tag{82}$$

Note that the values given are for grains whose symmetry axes are aligned with the analysis axes.

6.4 Results for the Seismic Anisotropy of Quartz/Muscovite Rock Fabrics

The first portion of this section will compare the seismic wave speeds computed from the AEH results with those generated from the other homogenization schemes in Section 6.1 for the synthetic rock fabric microstructures. Subsequently, a comprehensive parametric study will be performed to assess the roles of muscovite volume fraction, muscovite crystal orientation distribution and quartz crystal orientation on seismic anisotropy of quartz/muscovite rich rock fabrics using the aforementioned synthetic rock fabric microstructures. In all of the following sections, all results are generated using synthetic microstructures which possess 30 distinct quartz grains and have muscovite inclusions with dimensions $a = 0.4\ell$ and $b = 0.05\ell$. All homogenized stiffness tensors, which are required for computing the wave speeds, are generated via an ensemble average of 100 distinct realizations of the synthetic microstructures for a particular set of parameters. This is done in lieu of analyzing a single, large, detailed microstructure with the same fabric description parameters as it is computationally more efficient and provides the same homogenized stiffness tensor as discussed in Section 3.3. With regard to number of finite elements employed in each AEH analysis, let us first briefly investigate the convergence of the wave speed velocities with mesh refinement for a sample microstructure. Table 6.1 displays the convergence of seven particular wave speeds in km/s for a sample microstructure with $V_M = 0.3$, $\alpha = 10°$ and all quartz grains randomly oriented. As can be seen in the table, even the smallest mesh shown yields very good estimates for each of the wave speeds tabulated. For microstructures with the aforementioned volume fraction and muscovite inclusion distribution parameters, the analyses presented in the following sections utilize approximately $2,000$ to $2,500$ LST finite elements. As can be inferred from Table 6.1, this is a sufficient level of refinement. Therefore, to ensure good accuracy,

122

No. of Elements	$V_P(0°)$	$V_P(45°)$	$V_P(90°)$	$V_{S1}(0°)$	$V_{S1}(90°)$	$V_{S2}(0°)$	$V_{S2}(90°)$
948	5.519	5.897	6.497	3.456	4.229	3.398	3.444
1,326	5.515	8.891	6.500	3.451	4.231	3.391	3.438
1,998	5.514	5.890	6.499	3.450	4.230	3.391	3.437
2,448	5.514	5.889	6.499	3.449	4.230	3.390	3.436
3,642	5.514	5.889	6.498	3.449	4.230	3.390	3.436
5,038	5.513	5.888	6.498	3.448	4.229	3.390	3.436
6,904	5.513	5.888	6.498	3.448	4.229	3.390	3.436
9,008	5.513	5.888	6.498	3.448	4.229	3.390	3.436

Table 6.1. Convergence of selected wave speed velocities for a sample microstructure with $V_M = 0.3$, $\alpha = 10°$ and randomly oriented quartz grains. All wave speeds are in km/s.

all analyses employ between $1,000$ and $9,000$ LST finite elements depending on the complexity of the microstructure.

6.4.1 Comparison of Asymptotic Expansion Homogenization and Analytic Estimates

In this section, a comparison of the computed wave speed velocities obtained by the analytic estimates, bounds and AEH methods is performed. In order to carry out this investigation, select synthetic microstructures will be studied to emphasize the importance of using an accurate homogenization technique such as AEH to obtain accurate homogenized stiffnesses, and therefore, accurate wave speed velocities.

The first synthetic microstructure to be studied is for a synthetic microstructure with a muscovite volume fraction of $V_M = 0.3$, $\alpha = 0°$, and randomly oriented quartz crystals. The P and S-wave speed velocities are plotted in Figure 6.5(a) as a function of incidence angle γ using stiffnesses computed from the Voigt and Reuss bounds, the geometric and arithmetic means and the AEH method. As can be seen in Figure 6.5(a), V_P for the geometric mean, arithmetic mean and AEH methods are
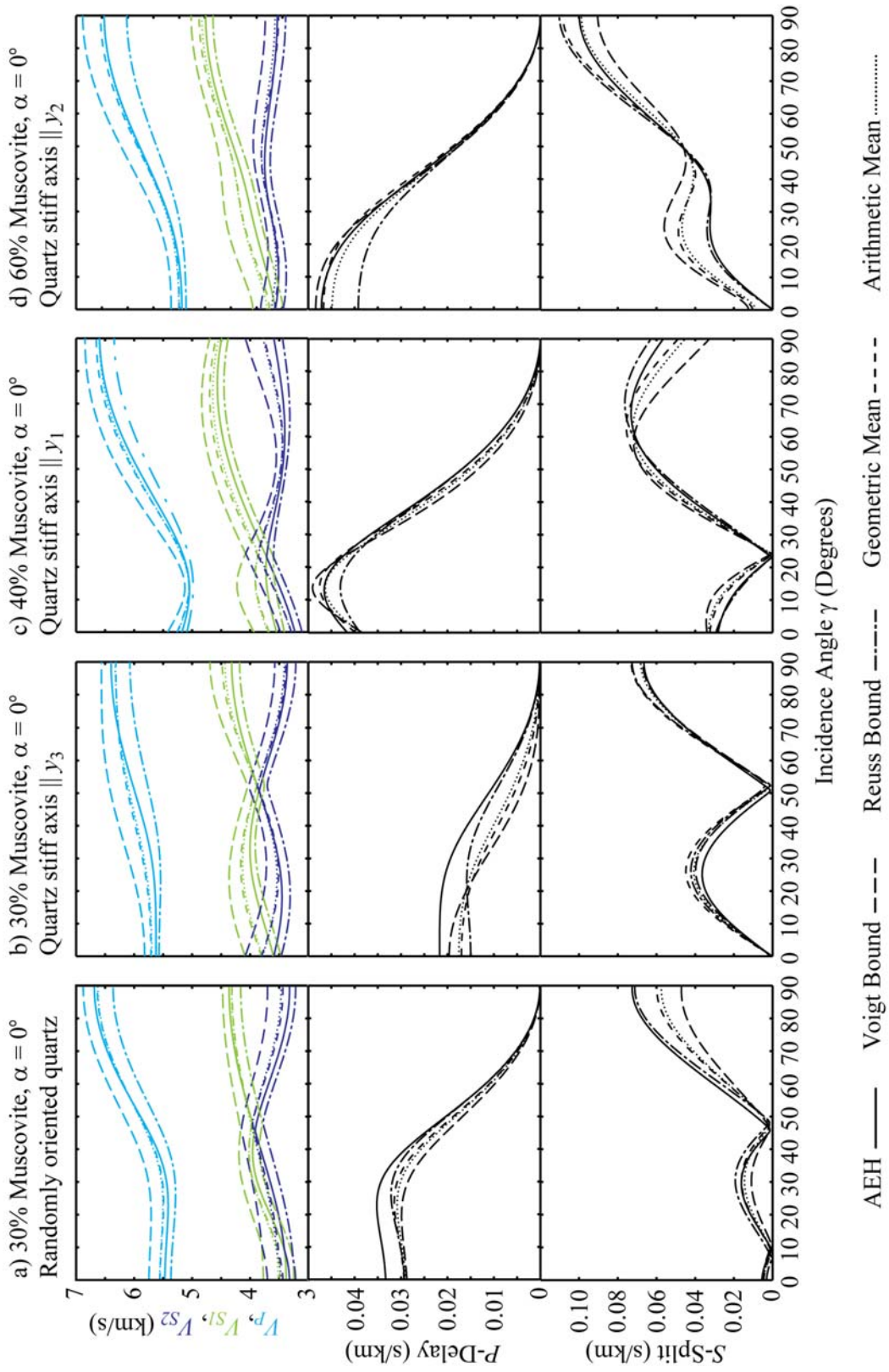
Figure 6.5. V_P, V_{S1}, V_{S2}, P-delay and S-split vs. incidence angle curves calculated using the AEH, Voigt and Reuss bound and geometric and arithmetic means for four specific microstructures.

similar and lie between the wave speeds computed from the bounds, as expected. However, V_P computed from the AEH method is lower than the geometric mean estimate up until $\gamma = 55.17°$ and is greater than the geometric mean thereafter. A similar trend exist between the AEH and arithmetic mean curves. This leads to a larger percent anisotropy of $A_P = 20.99\%$ for the AEH as opposed to $A_P = 18.82\%$ for the geometric mean. In fact, if one uses either of the bounds or the geometric or arithmetic means to compute the homogenized stiffness tensor, they will underestimate the percent anisotropy in the P-wave for this particular microstructure. In addition to underestimating A_P, using any of the analytic estimates or bounds will also underestimate the P-delay, Δt_P, for a large range of incidence angles as shown in Figure 6.5(a). For example, $\Delta t_P (20°) = 0.0350$ s/km using the AEH method, but ranges from $\Delta t_P (20°) = 0.0297$ s/km to $\Delta t_P (20°) = 0.0315$ s/km for the other bounds and estimates. Focusing on the S-wave speeds V_{S1} and V_{S2} in Figure 6.5(a), it is clear that the AEH results do not coincide closely with the geometric or arithmetic mean estimates once again. At $\gamma = 0°$, the AEH results for V_{S1} and V_{S2} both lie approximately halfway between speeds calculated using the geometric mean and Reuss homogenized stiffnesses. At $\gamma = 90°$ the AEH computed V_{S2} still lies between the geometric mean and Reuss lower bound, however, V_{S1} is located between the geometric mean and and Voigt upper bound values. This scenario gives rise to erroneous shear splitting values Δt_S for values of γ of $50°$ and larger if the geometric or arithmetic means are used, as seen in Figure 6.5(a). In fact, the shear splitting values from the AEH results are larger than any of the other predicted values for $\gamma > 46.95°$.

The second synthetic microstructure to be investigated also has a muscovite volume fraction of $V_M = 0.3$ and an $\alpha = 0°$, albeit the quartz crystals all have their stiff axis oriented in the y_3 direction. The wave speeds for the AEH, bounding methods, geometric and arithmetic means as a function of γ are given in Figure 6.5(b). Similar

to the previously discussed synthetic rock fabric, the AEH computed V_P wave speed is closer to the Ruess than Voigt bound at $\gamma = 0°$ and vice versa for $\gamma = 90°$. This, of course, indicates that A_P is actually much higher than would be computed by either of the bounds or geometric mean. Unlike the previous fabric, though, the discrepancy between the AEH and geometric mean for V_P increases appreciably from $\gamma = 0°$ up to an intermediate angle of $\gamma = 35.10°$ where there is a peak error of 2.82% in the geometric mean estimated wave speed. The end result is that the geometric mean, or any of the other estimates or bounds for that matter, do not accurately capture the shape of the $V_P(\gamma)$ curve. This fact also manifests itself in the poorly predicted P-delay curves by the estimates and bounds, as shown in Figure 6.5(b). Referring to the V_{S1} and V_{S2} for this particular rock fabric in Figure 6.5(b), it can be seen that for large ranges of incidence angle γ, the AEH results do not correlate well with either of the bounds or the geometric mean. This can give rise to erroneous S-split values if the AEH wave speeds are not utilized, as shown in Figure 6.5(b). In addition, it is worth noting that the difference between $V_S^{\max}$ and $V_S^{\min}$ for the AEH results is smaller than any of the other methods. This will give rise to overestimated shear wave speed anisotropy A_S if the bounds or geometric mean are employed and is contrary to the first rock fabric studied, where the opposite is true. For the curves shown in Figure 6.5(b), the AEH results give $A_S = 12.45\%$ as opposed to $A_S = 13.03\%$ for the arithmetic mean, the next lowest estimate of A_S.

The next synthetic microstructure for which the wave speeds are computed is for a muscovite volume fraction of $V_M = 0.4$, $\alpha = 20°$ and all quartz crystals oriented such that their stiff axis is in the y_1 direction. The wave speeds for each of the stiffness tensor homogenization methods of interest are shown in Figure 6.5(c). In the previous two cases, the geometric and arithmetic means have been the closest to the AEH results on average. In some instances, these estimates have overestimated some of the wave speeds and at times, underestimated some of the wave speeds. The

case shown in Figure 6.5(c) is unique because the geometric and arithmetic means overestimate all three of the wave speeds V_P, V_{S1} and V_{S2} for the entire range of incidence angles shown. Another distinction between this fabric and the other two is that the minimum error in the geometric mean estimate of V_P occurs at a small incidence angle of $16.65°$ whereas the other two fabrics had geometric mean estimates that were most accurate at higher incidence angles. To be more specific, the fabric of Figure 6.5(a) had coincident geometric mean and AEH computed wave speeds at $\gamma = 55.17°$ and the fabric of Figure 6.5(b) at $\gamma = 69.20°$.

The last synthetic fabric studied possesses parameters of $V_M = 0.6$ and $\alpha = 20°$ with all quartz crystals oriented such that their stiff axis is aligned with the y_2 direction. The wave speeds for this fabric are shown in Figure 6.5(d) for the AEH and other homogenization methods. As can be seen in the figure, the wave speeds for the geometric and arithmetic mean estimates are relatively close to the AEH results with the exception of V_{S1}. For the entire range of γ shown in the figure, the AEH derived V_{S1} is significantly smaller than corresponding geometric mean values. For this fabric, the geometric mean will give good estimates of the true A_P, ν_{P45} and P-delay but will significantly overestimate A_S as well as the S-split Δt_S for most incidence angles presented here as seen in Figure 6.5(d). The arithmetic mean suffers from the same problems with the exception that the predicted S-split is fairly good for high γ and the predicted P-delay is slightly worse than the geometric mean values for low γ.

After reviewing these four fabric cases, one major point is very clear. There is no direct correlation between the wave speeds computed using the homogenized stiffnesses from the geometric mean, arithmetic mean and bounding methods and those obtained using the more accurate AEH method. For example, if one decides to utilize the geometric mean to obtain the homogenized stiffness tensor, the estimated wave speeds could be high or they could be low depending on the incidence angle and grain orientations. And where these variations in the estimates occurs over the range of

127

incidence angles will not be clearly evident. Therefore, it is crucial that an accurate homogenization scheme such as AEH, which accounts for the elastic interplay between polycrystals, be employed in order to subsequently compute accurate wave speed velocities over the entire range of incidence angles.

6.4.2 Sensitivity Analysis of Phase Volume Fractions, Crystal Orientations and Crystal Spatial Distribution

In order to investigate the sensitivity of seismic wave speed velocities on phase volume fractions, crystal orientations and spatial distributions, a parametric studied is performed. The aforementioned variables are systematically changed for the synthetic microstructures of Section 6.3 and the AEH elastic stiffnesses are utilized in determining the wave speed velocities and seismic anisotropy measures.

Figure 6.6 shows the V_P, V_{S1} and V_{S2} velocities, the P-delay and S-split versus the incidence angle for different quartz orientations at different volume fraction of muscovite. The standard deviation for the orientation of the muscovite grains is $\alpha = 0°$ for the plots in Figure 6.6 in order to isolate the effects of muscovite volume fraction and quartz grain orientation. For the fabric consisting of pure quartz, one can see that the material behaves fairly isotropic if the quartz grains are oriented randomly, as expected. The V_P, V_{S1} and V_{S2} velocities remain constant at varying incidence angles and the P-delay and S-split are close to 0 for the entire range of γ investigated. In the fabric that has the stiff axis of the quartz oriented parallel to the y_2 axis, the V_P curve possesses an isotropic behavior as well, due to the trigonal symmetry of the quartz crystals. The velocity profiles become more alike if more muscovite is added to the system and the strong elastic anisotropy of the muscovite starts to play a dominant role. When no muscovite is present, the V_{S1} and V_{S2} curves possess a similar value at varying incidence angles depending on the quartz grain orientations. With increasing amounts of muscovite these locations move closer to one another to

Figure 6.6. V_P, V_{S1}, V_{S2}, P-delay and S-split curves as a function of incidence angle for microstructures with varying volume fractions of muscovite and varying quartz orientations with $\alpha = 0°$.

Random quartz ——   Quartz stiff axis $\| y_1$ – – –   Quartz stiff axis $\| y_2$ ········   Quartz stiff axis $\| y_3$ – · – ·

eventually occur at little under 40° when 90% of the fabric consists of muscovite. As the volume fraction of muscovite increases the P-delay and S-split values also increase due to the greater volume of the highly anisotropic muscovite phase relative to the mildly anisotropic quartz phase.

Figure 6.7 shows the V_P, V_{S1} and V_{S2} velocities, the P-delay and S-split versus the incidence angle for different standard deviations for the muscovite orientations at different volume fractions of muscovite. For these plots a random orientation of quartz is used as it creates a relatively isotropic matrix, making that the influence of the orientation of the muscovite grains the primary factor in seismic anisotropy characteristics. With increasing amounts of muscovite the same behavior occurs as is displayed in Figure 6.6, namely larger variations in the V_P and V_{S1}, V_{S2} curves which give rise to higher peak P-delay and S-split values. As for the effect of muscovite grain standard deviation, it can be seen in Figure 6.7 that increasing α creates a bulk material that becomes less anisotropic which manifests itself in the diminished magnitude of the P-delay and S-split curves for most γ. This is not surprising since greater variation in the muscovite grain orientations contributes to greater bulk stiffness in the y_3 direction and detracts from the bulk stiffness in y_1 direction creating a less anisotropic rock fabric. Another effect of increasing the muscovite grain orientation standard deviation is that the incidence angle at which the V_{S1} and V_{S2} curves possess a similar value decreases. This can be seen clearly in the S-split curves where the intermediate minimum Δt_S occurs at an ever smaller incidence angle as α is increased. For the $V_M = 0.6$ case, the location of the aforementioned point occurs at $\gamma = 41.40°$ for $\alpha = 0°$ and reduces to $\gamma = 30.15°$ for $\alpha = 20°$.

Figure 6.8 shows the percentage anisotropy of the V_P curve, A_P, as a function of muscovite volume fraction for the fabrics with the different quartz orientations and muscovite inclusion distributions. For the fabrics in which the quartz is either oriented randomly or is aligned with its stiff axis in the y_1 or y_2 direction, A_P increases
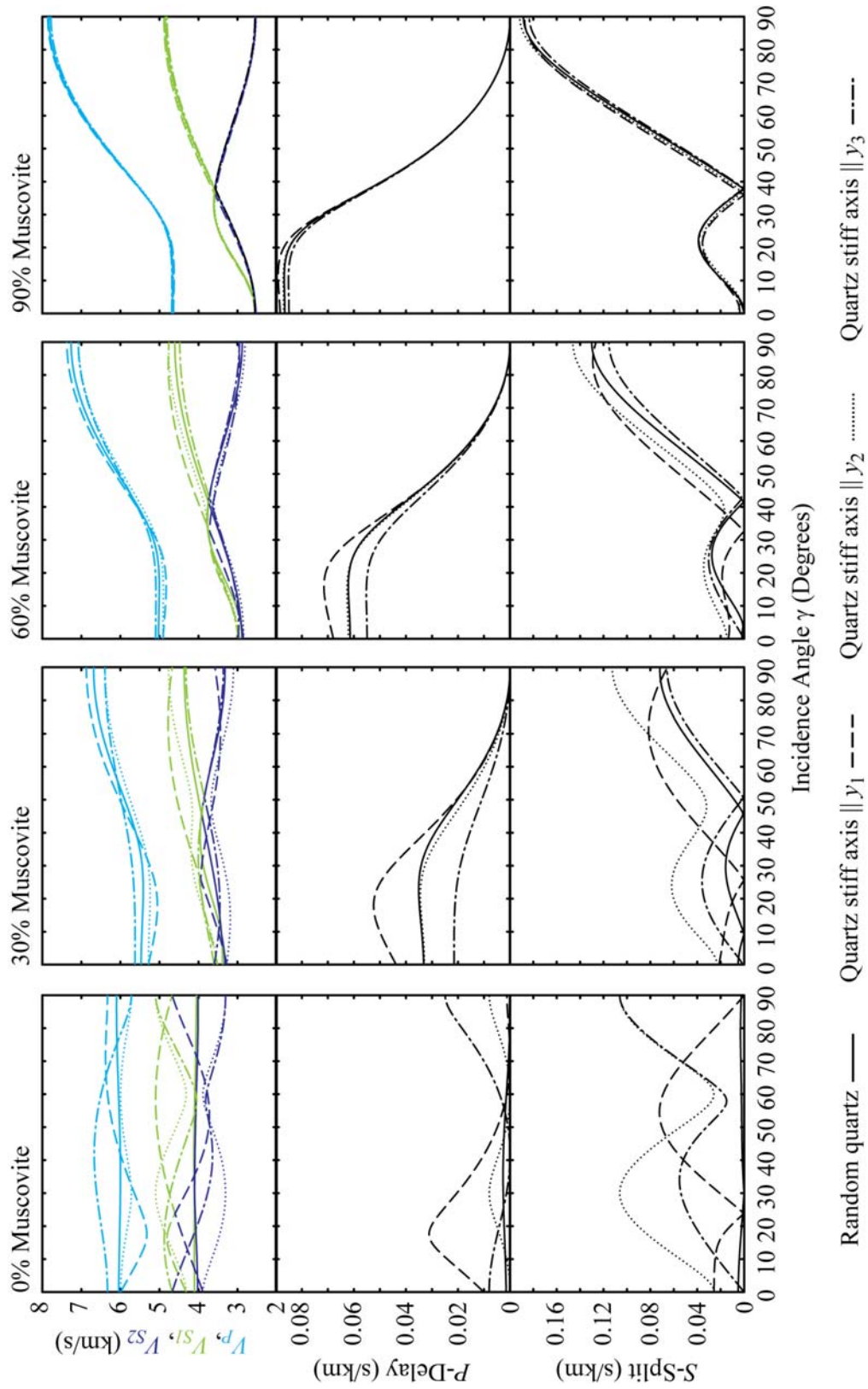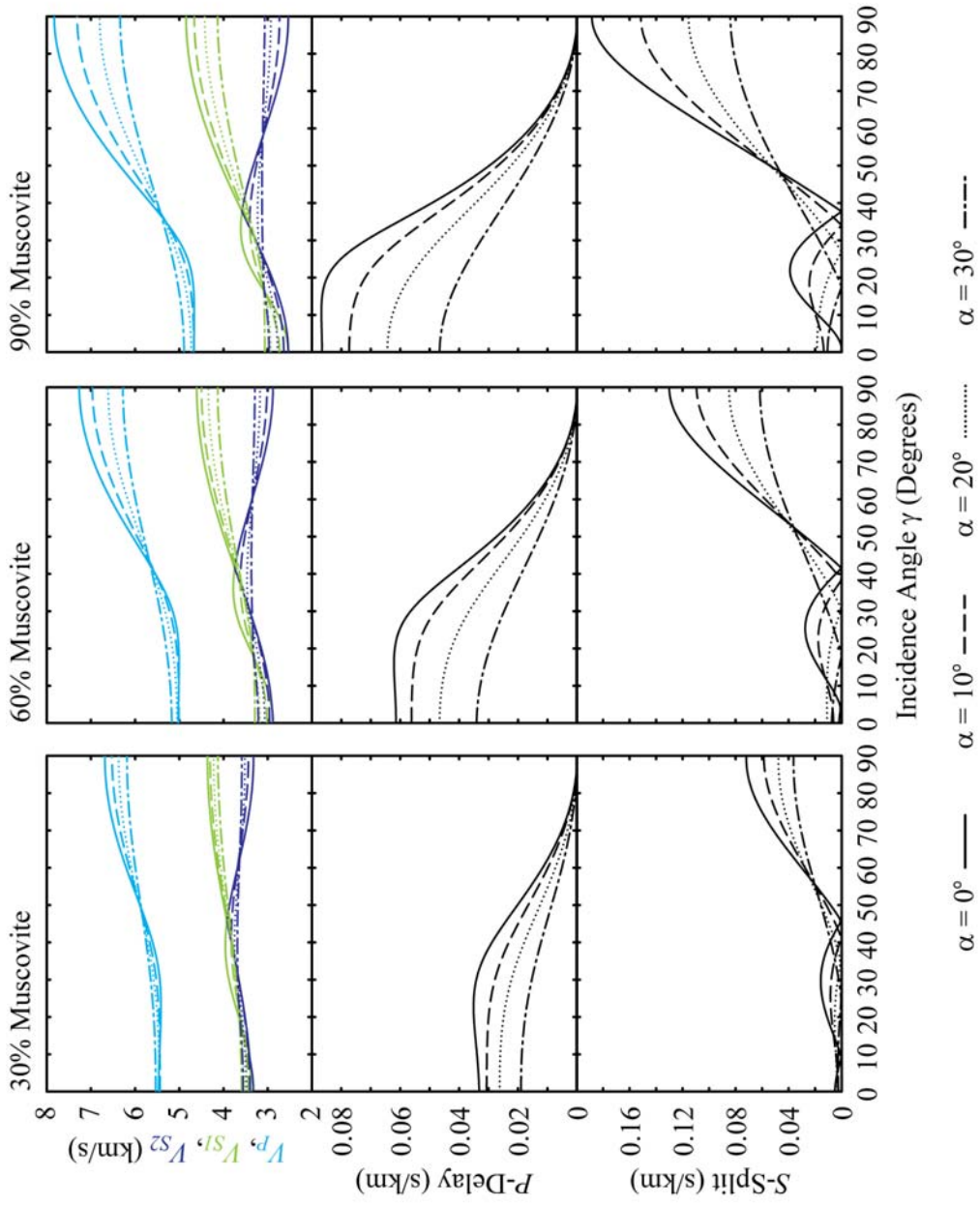
Figure 6.7. V_P, V_{S1}, V_{S2}, P-delay and S-split curves as a function of incidence angle for microstructures with varying volume fractions of muscovite and varying muscovite orientation distributions with randomly oriented quartz.

131

Figure 6.8. A_P for varying muscovite distributions and quartz orientations as a function of muscovite volume fraction.

with increasing muscovite volume fraction. If the quartz is oriented with its stiff axis parallel to the y_3 axis the anisotropy decreases until approximately 15 to 20% muscovite volume fraction, and increases with increasing amounts of muscovite. This dip in percentage anisotropy of the V_P curve is due to the alignment of the stiff axis of the quartz with the compliant axis of the muscovite. This creates a fabric that becomes less anisotropic as muscovite is slowly introduced. Once enough muscovite is present, however, the strong anisotropy of the muscovite becomes the dominant factor in determining the bulk percentage anisotropy. It should also be noted that with more variation in the muscovite orientations, that is a higher inclusion standard deviation, the increase in A_P is with increasing volume muscovite fraction is lower for the same reasons expressed previously that diminish peak P-delay and S-split values. Prior to proceeding, it is worth noting that Figure 6.8 clearly demonstrates the importance of the orientation of the quartz crystal orientations, especially at

132

low muscovite volume fractions. While the quartz orientations studied represent possible extremes, it is evident that fabrics that contain quartz crystals with a strong crystallographic preferred orientation have seismic anisotropy measures that depend greatly on the particular quartz crystal orientation. For example, the fabrics with $\alpha = 0°$ and $V_M = 0.2$ in Figure 6.8 have A_P values that range from 5.82% to 26.46% depending on whether the quartz crystals are randomly oriented or are have their stiff axis aligned with a particular analysis coordinate.

Figure 6.9 shows the percentage anisotropy of the S-waves, A_S, versus the volume fraction of muscovite for the fabrics with the different quartz orientations and muscovite distributions. If the quartz is oriented randomly, the percentage anisotropy of the S-waves increases with an increasing amount of muscovite. When the quartz is oriented with the stiff axis parallel to the y_1 axis, A_S is 31.21% when no muscovite is present. When muscovite is added, A_S first slightly decreases before it increases with increasing amounts of muscovite. When the stiff axis of the quartz is oriented parallel to the y_2 and y_3 axes, the S-wave speed anisotropy of the pure quartz fabrics is 42.59%. For the fabrics with the quartz stiff axis aligned with y_3, the addition of muscovite with $\alpha = 20°$ decreases A_S to 21.18% at $V_M = 0.356$ with A_S increasing thereafter as more muscovite is included. If the muscovite has no variance in orientation, the S-wave speed anisotropy decreases to 24.53% with a $V_M = 0.261$ for the quartz stiff axis parallel to y_3. For the fabric with quartz stiff axis aligned with the y_2 direction and $\alpha = 0°$, A_S diminishes to 40.62% with $V_M = 0.135$. In general, A_S behaves similar to A_P although there are some key differences. The cases where the quartz stiff axis is oriented in either the y_1 and y_2 directions possess A_S curves that dip slightly at first before increasing with increasing muscovite content. The corresponding A_P curves increase monotonically as muscovite volume fraction increases. In addition, A_S for the fabric with the quartz stiff axis aligned with the y_3 axis continues to diminish beyond the muscovite volume fraction point at which
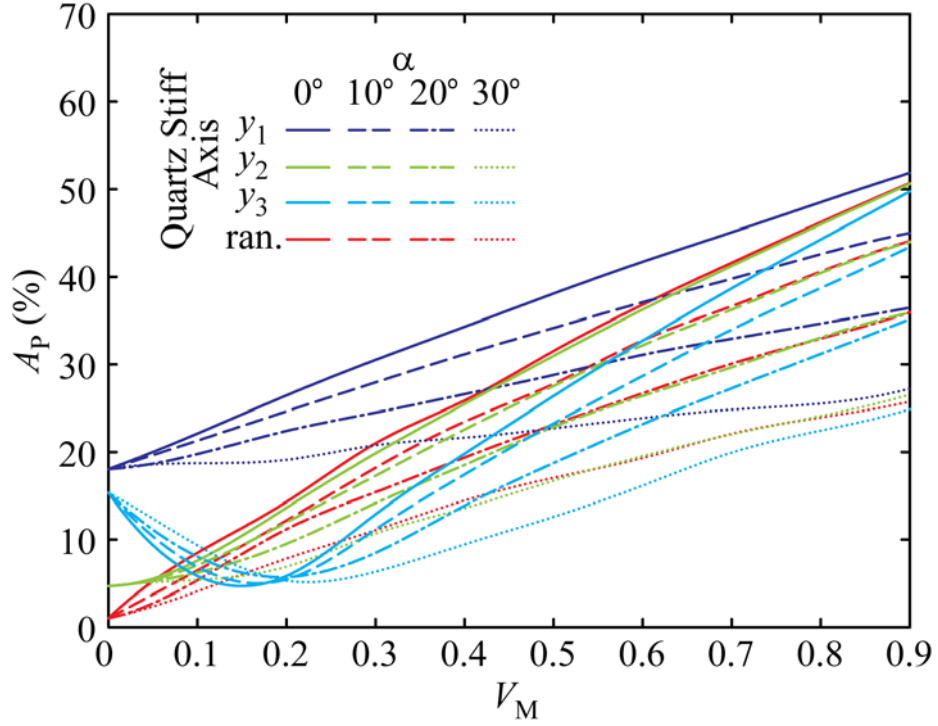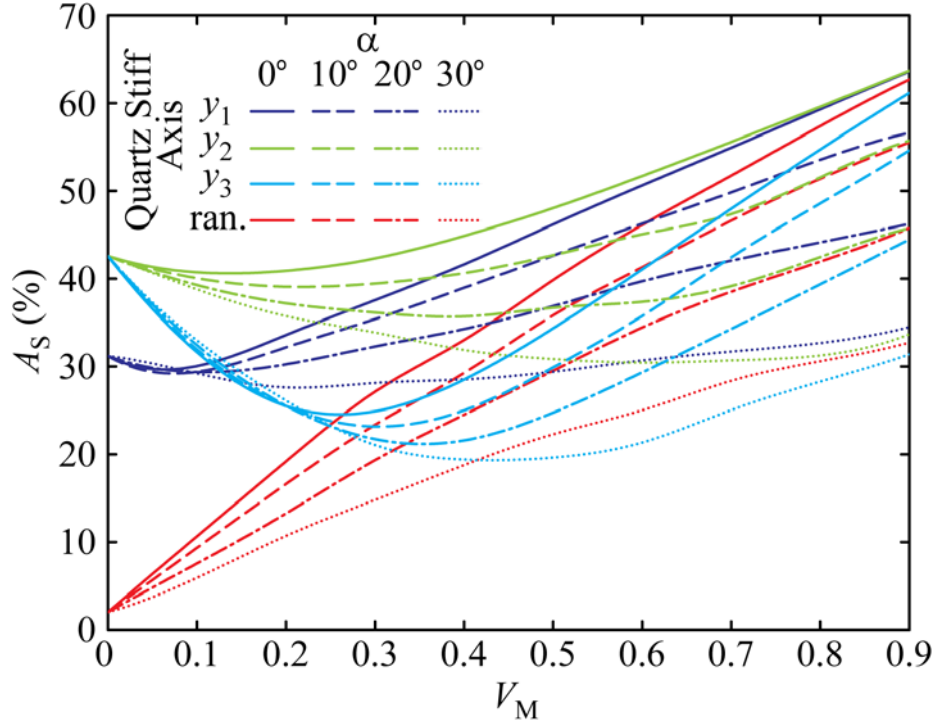
Figure 6.9. A_S for varying muscovite distributions and quartz orientations as a function of muscovite volume fraction.

the corresponding A_P obtains its minimum value and increases more slowly with the introduction of more muscovite once the minimum A_S is achieved. As was noted in the discussion of A_P trends, the importance of the quartz crystal orientation is very significant at lower muscovite volume fractions and the curves of A_S in Figure 6.9 reinforce this notion.

Figure 6.10 shows the ν_{P45} versus the volume fraction of muscovite for the fabrics with the different quartz orientations and muscovite distributions. With less than approximately 50% volume muscovite, the percentage magnitudes are high and are omitted from the plot. This is due to the small difference between $V_P(0°)$ and $V_P(90°)$ for these fabrics, the difference of which constitutes the denominator of the ν_{P45} calculation thus creating very large ν_{P45} values if $V_P(45°)$ is moderately different than $V_P(0°)$. At higher amounts of muscovite volume fraction, the orientation of the

134
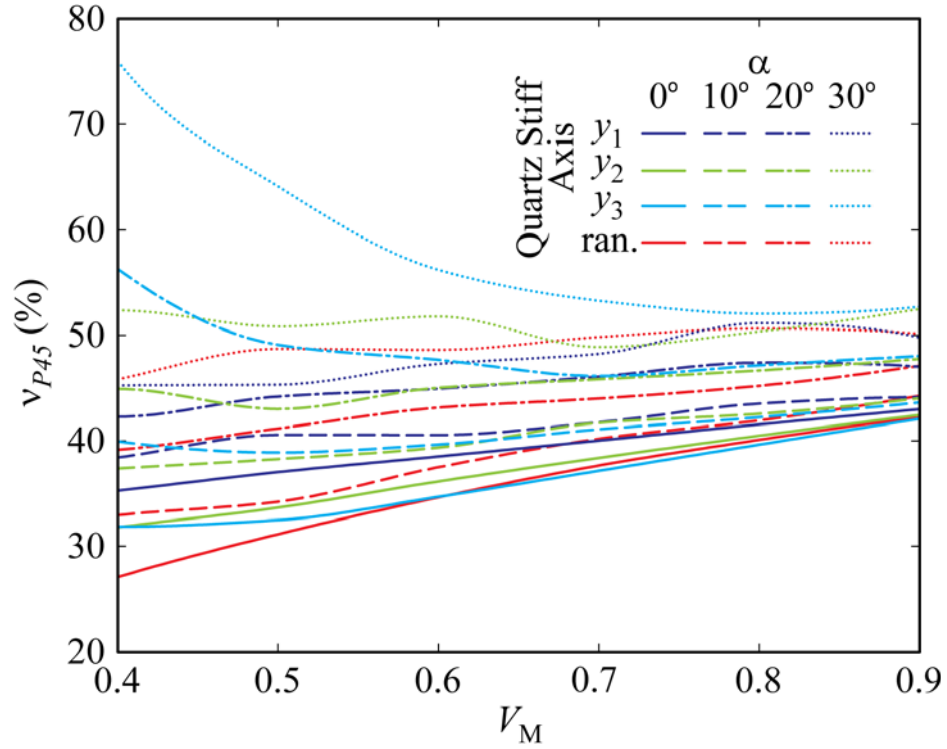
Figure 6.10. ν_{P45} for varying muscovite distributions and quartz orientations as a function of muscovite volume fraction.

quartz appears to have a minor effect on ν_{P45}. At intermediate volume fractions, the role is potentially more significant as seen in the larger spread of possible ν_{P45} for a given α and quartz crystal orientation. As can be seen in Figure 6.10, the particular combination of $V_M = 0.4$, $\alpha = 30°$ and all quartz crystals with stiff axes lying in the y_3 direction gives $v_{P45} = 76.01\%$, a value that is rather large for normalized $V_P(45°)$. The V_P and V_{S1}, V_{S2} curves for this particular rock fabric are shown in Figure 6.11. Unlike the V_P trends for the Haast Schist in Figure 6.3, the P-wave velocity increases more rapidly with increasing incidence angle and remains relatively constant for incidence angles larger than $60°$. This behavior gives rise to the aforementioned large v_{P45}. Referring back to Figure 6.11 it can be seen that the muscovite inclusion distribution, unlike quartz crystal orientation, does appear to play a more significant role at moderate and large muscovite volume fractions as increasing
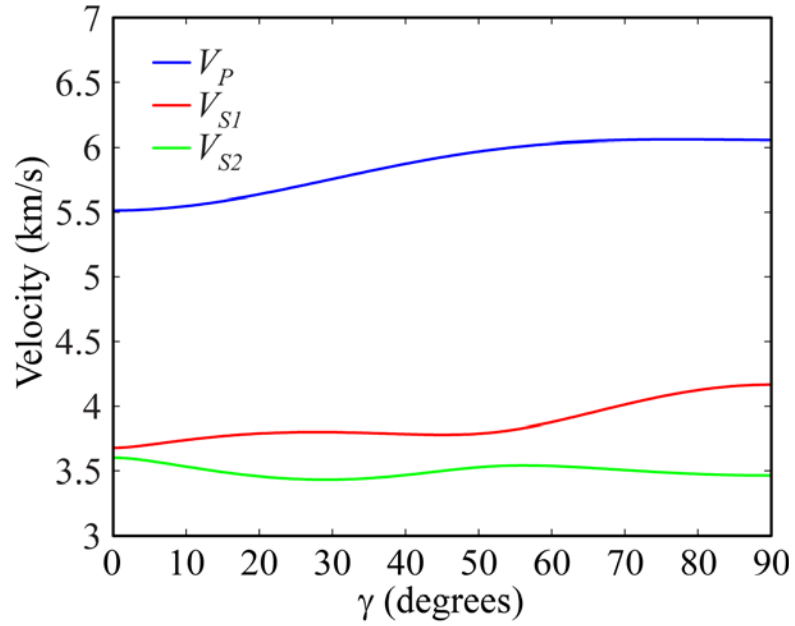
Figure 6.11. Wave speeds as a function of incidence angle for rock fabrics with $V_M = 0.4$, $\alpha = 30°$ and quartz grain stiff axes aligned with the y_3 direction.

α tends to increase ν_{P45}. This fact is supported by the V_P curves for the $V_M = 0.6$ fabric shown in Figure 6.8. As can be seen in the figure, $V_P(45°)$ is approximately the same for all α shown as is also the case for $V_P(90°)$, however, $V_P(90°)$ diminishes significantly with increasing α. This trend maintains the numerator in equation (76) whilst shrinking the denominator with increasing α, thus increasing ν_{P45}.

CHAPTER 7

CONCLUSIONS AND FUTURE WORK

In the first part of this dissertation, a methodology is developed for the creation of simulated random heterogeneous microstructures, the properties of which are characterized using the asymptotic expansion homogenization method. The simulated microstructures, which are generated using a random morphology description function, compare well with actual micrographs of heterogeneous materials. The random microstructures are characterized using statistical tools from the field of random heterogenous media. The microstructures generated by the RMDF method are found to be statistically homogeneous and isotropic. Results indicate that on average percolation occurs when the volume fractions of the individual material phases equal 0.5, although the exact volume fraction at which percolation occurs depends on the specific RMDF microstructure under consideration. The simulated microstructures exhibit an internal characteristic length that depends on the number of Gaussian sources used to construct the RMDF. Thus, it is possible to create random microstructures with a desired characteristic length by simply varying the number of Gaussian sources. Numerical results show that the characteristic length can be halved by quadrupling the number of Gaussian sources.

The homogenized material properties of simulated RMDF microstructures are obtained using the AEH method. The microstructural fields necessary for the determination of the homogenized material properties are obtained by solving an auxiliary problem at the microscale using the finite element method. The homogenized material properties are compared with widely used analytical homogenization schemes and bounding methods. For typical material combinations with moderate disparities in the phase material properties, the homogenized properties obtained using the self-consistent scheme are in good agreement with values obtained using the AEH

method. However, the self-consistent scheme and AEH method results differ for the one high-contrast material combination studied. In the absence of further study no generalizations can be made regarding the accuracy of the self-consistent scheme for high-contrast two-phase composites. Nevertheless, the results of the high-contrast material study stress the importance of using an accurate homogenization method such as AEH when precise estimates of the effective material properties of random heterogeneous materials are required.

In addition to characterizing the statistical and thermomechanical properties of random heterogeneous microstructures, failure of random heterogeneous materials is analyzed using a direct micromechanical failure analysis approach. The microstresses in conjunction with material failure models are used to assess failure at the microstructural level. Initial failure envelopes are presented for metal/ceramic and metal/metal random heterogeneous materials. The failure envelopes, which are conservative since they represent the stresses at which on average initial failure occurs at some point in the microstructure, provide useful insight into the strength of random heterogenous materials. While metal/metal material combinations exhibit equal strength in both biaxial tension and compression, metal/ceramic random materials possess greater strength in biaxial compression than tension due to the large compressive strength and comparatively low tensile strength of the ceramic phase. The effect of temperature and the resulting thermal stresses on the failure envelopes for random heterogeneous materials is also investigated. As the temperatures increases, the strength of the heterogeneous material decreases in biaxial tension and increases in biaxial compression.

To conclude the portion of the work concerning random heterogeneous materials, results for two model problems with random microstructure are presented to illustrate the multiscale failure analysis approach. The first is an Al/Al_2O_3 functionally graded beam with an applied mechanical load. The average stresses are obtained

through a finite element solution of the macroscopic equations. The failure envelopes of Al/Al_2O_3 are used to obtain the factor of safety of the functionally graded beam. The factor of safety obtained from the failure envelopes, which represents the average strength of $1,000$ distinct microstructure realizations, is compared with the values obtained for three separate representative random microstructures at the critical location. While the factors of safety are different for each of the three realizations presented, they compare well with the factor of safety obtained using the failure envelopes. The second model problem concerns the multiscale analysis of a W/Cu functionally graded component subjected to an intense heat flux over a portion of its boundary. It is found that the macroscopic temperature and average stresses computed using the material properties from asymptotic expansion homogenization are nearly identical with values obtained using the self-consistent material properties. This observation lends further proof that the self-consistent scheme is suitable for estimating the effective properties of random heterogeneous materials when the contrast in the material properties of the phases is small to moderate, which is the case for the W/Cu material combination considered here. Next, direct micromechanical failure analysis of random microstructures are performed to obtain the necessary initial failure envelopes to assess the failure of the thermally loaded W/Cu heterogeneous component. As was done in the first model problem, the factor of safety obtained from the failure envelopes is compared with results from three distinct sample RMEs at the critical location. Once again, good agreement between the two is observed. Lastly, it should be noted that analysis of sample microstructures at the critical locations show that only very localized regions in the RMEs experience low factors of safety and a large portion of the microstructure is well within the failure strengths. This reinforces the notion that the direct micromechanical failure analysis presented here yields conservative strengths.

The second major portion of this dissertation presents a methodology for the transient thermoelastic analysis of functionally graded materials. Two-phase microstructures are created using morphology description functions. With the macroscopic geometry, volume fraction distribution and loading as well as knowledge of the microstructural morphologies at all locations within the macroscopic body, a multiscale analysis is carried out using the asymptotic expansion homogenization method coupled with a finite element technique. The developed multiscale code is validated using two problems previously studied in the literature. The first problem is a multiscale analysis of a boron/aluminum plate loaded in tension with a centrally located hole studied by Fish and Wagiman (1992) as well as Ghosh *et al.* (1995). Results for the homogenized elastic constants of the boron fiber/aluminum matrix microstructures compare very well with those provided in previous works. In addition, line plots of microstress component σ_{22}^0 through the microstructure at the critical location generated from the multiscale analysis code compare favorably with published results in (Fish and Wagiman, 1992; Ghosh *et al.*, 1995). In the second problem, the transient thermomechanical response of a functionally graded plate for which an exact solution has been provided by Vel and Batra (2003), is used to validate the transient macroscopic analysis finite element code. Transient and through thickness results for the temperature and stresses in the plate compare well with the exact results.

After validating the multiscale finite element codes, two model problems are studied to demonstrate the potential of the multiscale approach as applied to thermally loaded functionally graded material components. The first transient multiscale FGM problem studied is a bilinearly graded tungsten/copper specimen with fairly simple microstructural morphologies subjected a time-varying heat flux over a portion of its top surface. After performing the multiscale analysis which included a direct micromechanical failure analysis, it is determined that the minimum factor of safety F_s occurs at a location the middle of the specimen at a volume fraction of $V_W = 0.5$

which corresponds to a microstructural morphology which resembles a checkerboard. The low factor of safety can be attributed to the presence of very sharp corners in the phase boundaries within the microstructure for $V_W = 0.5$ which give rise to very large stress concentrations. Other points in the specimen where the macroscopic temperature and stresses are more severe but the volume fraction V_W is not equal to 0.5 do not give rise to lower factors of safety F_s^{macro} lower than the aforementioned critical point since the microstructure morphologies at these volume fractions possess phase boundaries with gentler profiles that do not magnify stresses nearly as severe as the checkerboard pattern. This illustrates that while the factor of safety of a two-phase material depends on the macroscopic condition, the morphology of the microstructure plays a critical role in the failure of the material. Lastly, the results provided by the multiscale analysis for the first model problem also demonstrate that while the specimen, which is in a state of plane stress, has an out-of-plane macroscopic stress component $\bar{\sigma}_{33}$ that is zero throughout the component, this does not imply that the corresponding microstress component σ_{33}^0 need also be zero throughout the microstructure. In fact, the component σ_{33}^0 can be fairly significant even when $\bar{\sigma}_{33} = 0$ and must not be neglected.

The second transient FGM model problem studied is a titanium/zirconia functionally graded turbine blade geometry in a state of plane stress at the macroscopic level. The blade, which has its outer temperature increased rapidly while maintaining interior cooling channels at the reference temperature, possesses random two-phase microstructures which resemble morphologies of a variety of actual composite materials. The multiscale analysis shows that the critical location in the blade begins in the monolithic zirconia outer layer and transitions through successively smaller zirconia volume fractions to a point on the interior of the graded region where $V_{\mathrm{ZrO_2}} = 0.53$ and remains stationary for the remainder of the transient until steady-state conditions are reached. The multiscale results also indicate that the increase in temperature

from the reference state θ^0 can create large internal stresses in the microstructure, and thus, is often the major factor limiting the factor of safety. However, while the temperature increase in the microstructure is important, it is not the only factor of significance as illustrated by the fact that the point of lowest factor of safety F_s occurs at a point in the blade where $V_{ZrO_2} = 0.53$ even though there are many other points of intermediate volume fraction in the blade where θ^0 is higher than at the critical location. This implies the microstructural morphology also plays a significant role in the microstress state, and hence, on determining the limiting factor of safety in the macroscopic body. In other words, θ^0, the microstructural morphology and to a lesser extent the macroscopic stress state all play a role in determining the microstresses, and hence the factor of safety F_s^{macro}, at a point in the macroscopic body. The multiscale procedure presented here can be used to identify the critical combination of conditions that determine the strength of a thermally loaded functionally graded component.

The last major focus of this dissertation involves studying the effects of some key rock fabric characteristics on seismic wave speed anisotropy for quartz/muscovite rich rocks. To determine the effect of these features on seismic wave speed anisotropy, synthetic quartz/muscovite rock fabric microstructures are created with adjustable muscovite volume fraction, muscovite inclusion distribution and quartz crystal material orientation. The homogenized elastic stiffnesses are obtained via the rigorous and accurate asymptotic expansion homogenization method and are subsequently utilized in determining the wave speed velocities via solution of the Christoffel equation. The wave speed velocities obtained using the asymptotic expansion homogenization stiffnesses are compared with those computed using elastic stiffnesses obtained from common estimates and bounds, namely the Voigt and Reuss bounds and the arithmetic and geometric means. Once the comparison of wave speeds is completed, a parametric study is performed by systematically adjusting the synthetic microstructure

characteristics and recording their homogenized elastic stiffnesses from the asymptotic expansion homogenization method. The wave speed velocities are subsequently computed for the resulting homogenized stiffnesses and used to evaluate common seismic anisotropy measures which distill complex wave speed versus propagation trends into more meaningful quantities.

When comparing the wave speed velocities computed from the commonly used analytic estimates and bound elastic stiffnesses with those obtained from the asymptotic expansion homogenization stiffnesses, no clear discernible trends are evident. On average, the geometric and arithmetic mean stiffnesses perform the best for computing the wave speed velocities over the entire range of propagation direction incidence angles explored in this work. However, it is nearly impossible to know if these homogenization estimates lead to overpredicted or underpredicted wave speed velocities let alone the magnitude of the error and how they vary with incidence angle. For the sample rock fabrics investigated, the analytic estimate stiffnesses were found to lead to poor predictions of percent anisotropy in the P and S- wave speed curves, normalized $V_P(45°)$ as well as P-delay and S-split curves. As evidence of this, one fabric possessed an actual A_S that was larger than any of those provided by the analytic bounds or estimate stiffnesses and another exhibited an A_S that was smaller than any of those computed from the bounds and estimates.

In performing the parametric study, a number of useful observations were made with regard to the importance of rock fabric characteristics on seismic wave speed anisotropy. At minimal to low muscovite volume fractions, the orientation of quartz crystals plays a significant role on the shape of the V_P, V_{S1} and V_{S2} trends as a function of incidence angle. When the quartz crystals are oriented randomly, the bulk rock exhibits quasi-isotropic seismic wave speed behavior. If the quartz crystals each have their stiff axes aligned in a particular direction, the wave speed velocities possess a more complicated dependence on the incidence angle, the variation of which is

143

also dependent on the particular preferred crystallographic orientation of the quartz crystals. As more muscovite is introduced into the fabric, the wave speed velocity trends are not influenced as greatly by the particular quartz crystal orientation. The end result is that the highly elastically anisotropic muscovite dominates the elastic, and hence, seismic behavior of the rock fabric which leads to generally higher A_P and A_S. With regard to the orientation distribution of the muscovite inclusions, increasing the standard deviation of the inclusions about the y_1 axis, α, tends to decrease the dependence of V_P, V_{S1} and V_{S2} on incidence angle. This results in smaller A_P and A_S values as well as diminished P-delay and S-split quantities for most γ as α is increased. For fabrics where the stiff axis of the quartz is aligned with the compliant axis of the muscovite, A_P and A_S diminishes as muscovite volume fraction is first increased and only begins to rise after an appreciable amount of muscovite volume is reached. The A_S as a function of muscovite volume fraction trends are similar, albeit far less pronounced, when the quartz stiff axis is aligned with the y_1 and y_2 directions. The last major seismic anisotropy measure studied, the normalized $V_P\left(45°\right)$ quantity, is not strongly affected by quartz orientation for moderate and high muscovite volume fractions. However, increasing α generally increases ν_{P45} for the aforementioned ranges of muscovite volume fractions. In addition, it is observed that certain combinations of muscovite volume fraction, α and quartz orientation can give rise to very high ν_{P45}. For $V_M = 0.4$, $\alpha = 30°$ and quartz grains with stiff axes aligned with the y_3 direction, ν_{P45} is a significant 76.01%.

With regard to future work, there exist a number of avenues related to this research which would prove useful to explore. In the field of random heterogeneous materials, further characterization of homogenized random media properties could be performed by employing altered, or entirely different, random morphology description functions. The effect of varying percolation thresholds, inclusion shapes and other key characteristics could be explored. In addition, further study of high contrast material

144

constituents, or even porous materials, could provide a number of useful insights. These could include assessing the performance of analytic homogenization schemes for high contrast materials as well determining the effect of pore size and shape on the strength of porous materials. Outside of studying different material combinations and RMDFs, an extension of the current methods to the nonlinear regime via multiscale elastoplastic analyses would prove worthwhile. With such a formulation, a better assessment of the failure response of random media beyond the loads predicted by the conservative initial failure envelopes could be made. While it is assumed that random media can support loads much higher than those predicted by the initial failure envelopes, a multiscale elastoplastic analysis would quantify the extent of conservatism in the direct micromechanical failure analysis methodology found in this work.

In the realm of functionally graded materials, many possible extensions of this work exist. While more accurate analyses of FGMs which account for microstructural morphology have been performed in this work, no tailoring of spatial volume fraction or microstructural morphology distribution throughout the FGM part has been performed here. Potential possibilities include optimizing volume fraction distribution for a given relationship between volume fraction and microstructural morphology, or even more alluring, optimizing the microstructural morphology at each point in the macroscopic FGM body to achieve maximum performance for a particular set of design criteria. In addition, the direct micromechanical failure analysis methods could be used to provide a more accurate assessment of component strength in optimization routines. Prior FGM optimization work which attempted to use component factor of safety as a design objective or constraint, such as Cho and Choi (2004) and Goupee and Vel (2007), did not utilize accurate methods of determining the homogenized strength of FGM materials. In addition to incorporating the direct micromechanical failure analysis technique into a FGM component optimization routine, one could also

extend the capabilities of the FGM analysis tool by incorporating the aforementioned multiscale elastoplastic analysis technique to obtain a more accurate FGM analyses, and therefore, more useful FGM designs from the optimization algorithms.

This work represents the first use of the asymptotic expansion homogenization method in the geophysics community, and as such, many other opportunities exist for the AEH method in geology. Within the field of seismology, the multiscale methods employed here could be utilized to extensively to better understand the role rock fabrics and geologic features on seismic wave anisotropy. In addition to the rock fabrics focused on in this work, other, more complicated features could be incorporated into the rock microstructures to better simulate the wide variety of fabrics found in Earth. These could include more mineral types, more realistic crystal shapes and more complex arrangements of crystal distributions throughout the microstructure such as crenulation cleavage. Other opportunities include employing the AEH method to determine the homogenized elastic stiffnesses of actual micrographs from real rock samples obtained by electron back scatter diffraction. This could lead to better development of synthetic microstructures for studying seismic wave speed anisotropy as well as help ascertain the true wave speed velocities in Earth's crust.

REFERENCES

Aldrich DE, Fan Z, 2001, Microstructural characterization of interpenetrating nickel/alumina composites, *Materials Characterization* **47**:67-173.

Aldrich DE, Fan Z, Mummery P, 2000, Processing, microstructure and physical properties of interpenetrating Al_2O_3/Ni composites, *Materials Science and Technology* **16**:747-752.

Auld BA, 1990, *Acoustic Fields and Waves in Solids*, Volume 2, 2nd Edition., Robert E. Krieger Publishing Co., Malabar.

Bass JD, 1995, Elasticity of minerals, glasses and melts, In: *Mineral Physics and Crystallography, A handbook of Physical Constants*, AGU Reference Shelf 2, Ahrens TH (Ed.), American Geophysical Union, Washington, D.C.

Bensoussan A, Lions J-L, Papanicolaou G, 1978, *Asymptotic Analysis for Periodic Structures*, North-Holland Publishing Co., Amsterdam.

Benveniste Y, 1987, A new approach to the application of Mori-Tanaka's theory in composite materials, *Mechanics of Materials* **6**:147-157.

Birch F, 1960, The velocity of compressional waves in rocks to 10 kilobars, part 1, *Journal of Geophysical Research* **65**:1083-1102.

Birch F, 1961, The velocity of compressional waves in rocks to 10 kilobars, part 2, *Journal of Geophysical Research* **66**: 2199-2224.

Bishop JFW, Hill R, 1951, A theory of the plastic distorsion of a polycrystalline aggregate under combined stresses, *Philosophical Magazine* **42**:414-427.

Biswas A, Shapiro V, Tsukanov I, 2004 Heterogeneous material modeling with distance fields, *Computer Aided Geometric Design* **21(3)**:215-242.

Bond WL, 1943, The mathematics of the physical properties of crystals, *Bell System Technical Journal* **22**:1-72.

Brahim-Otsmane S, Francort G, Murat F, 1988, *Homogenization in thermoelasiticy in Random Media and Composites*, Eds. Kohn RV, Milton GW, SIAM Press, Philadelphia, 13-45.

Cahn JW, 1965, Phase separation by spinodal decomposition in isotropic systems, *The Journal of Chemical Physics* **42(1)**:93-99.

Cao XF, Liu ST, 2006, Topology description function based method for material design, *Acta Mechanica Solida Sinica* **19(2)**:95-102.

Casteñeda PP, deBotton G, 1992, On the homogenized yield strength of two-phase composites, *Proceedings of the Royal Society of London A* **438**:419-431.

Cheng ZQ, Batra RC, 2000, Three-dimensional thermoelastic deformations of a functionally graded elliptic plate, *Composites: Part B* **31(2)**:97-106.

Cheng J, Lei C, Xiong E, Jiang Y, Xia Y, 2006, Preparation and characterization of W-Cu nanopowders by a homogeneous precipitation process, *Journal of Alloys and Compounds* **421**:146-150.

Cho JR, Choi JH, 2004, A yield-criteria tailoring of the volume fraction of metal-ceramic functionally graded materials, *European Journal of Mechanics A/Solids* **23**:271-281.

Cho JR, Ha DY, 2001, Averaging and finite-element discretization approaches in the numerical analysis of functionally graded materials, *Materials Science and Engineering* **A302**:187-196.

Cho JR, Ha DY, 2002, Optimal tailoring of 2D volume-fraction distributions for heat-resisting functionally graded materials using FDM, *Computer Methods in Applied Mechanics and Engineering* **191**:3195-3211.

Christensen NI, 1965, Compressional wave velocities in metamorphic rocks at pressures to 10 kilobars, *Journal of Geophysical Research* **70**:6147-6164.

Christensen NI, 1966, Shear wave velocities in metamorphic rocks at pressures to 10 kilobars, *Journal of Geophysical Research* **71**:3549-3556.

Christensen NI, 1985, Measurements of dynamic properties of rock at elevated temperatures and pressures, In: Pincus HJ, Hoskins ER. (Eds.), *Measurements of Rock Properties at Elevated Pressures and Temperatures*, ASTM STP 869. American Society for Testing and Materials, Philadelphia, 93-107.

Christensen NI, Mooney WD, 1995, Seismic velocity structure and composition of the continental crust: A global view, *Journal of Geophysical Research* **100**:9761-9788.

Christoffel EB, 1877, Uber die Fortpflanzung von Stossen durch elastische feste Korper, *Annali di Matematica Pura ed Applicata* **8**:193-243.

Cook RD, Malkus DS, Plesha ME, Witt RJ, 2002, *Concepts and Applications of Finite Element Analysis*, 4th Edition, John Wiley & Sons, Inc., Hoboken.

Cristescu N, 1989, *Mechanics of Elastic and Inelastic Solids. Rock Rheology*, Kluwer Academic Publishers, Dordrecht

del Rio E, Nash JM, Williams JC, Breslin MC, Daehn GS, 2007, Co-continuous composites for high temperature applications, *Materials Science and Engineering A* **463**:115-121.

de Ruiter MJ, van Keulen F, 2004, Topology optimization using a topology description function, *Structural and Multidisciplinary Optimization* **26(6)**:406-416.

Dowling NE, 2006, *Mechanical Behavior of Materials*, 3rd Edition, Prentice-Hall, Englewood Cliffs.

Elishakoff I, Guédé Z, 2004, Analytic polynomial solutions for vibrating axially graded beams, *Mechanics of Advanced Materials and Structures* **11**:517-533.

Feng X-Q, Tian Z, Liu Y-H, Yu S-W, 2004, Effective elastic and plastic properties of interpenetrating multiphase composites, *Applied Composite Materials* **11**:33-55.

Finot M, Suresh S, 1996, Small and large deformation of thick and thin-film multilayers: Effect of layer geometry, plasticity and compositional gradients, *Journal of the Mechanics and Physics of Solids* **44**: 683-721.

Fish J, Wagiman A, 1992, Multiscale finite element method for a periodic and nonperiodic heterogeneous medium, *Adaptive, Multilevel, and Hierarchical Computational Strategies ASME* **157**:95-117.

Fish J, Yu Q, 2001, Multiscale damage modelling for composite materials: theory and computational framework, *International Journal for Numerical Method in Engineering* **52**:161-191.

Francort GA, 1983, Homogenization and linear thermoelasticity, *SIAM Journal of Mathematical Analysis* **14**:696-708.

Ghosh S, Lee K, Moorthy S, 1995, Multiple scale analysis of heterogeneous elastic structures using homogenization theory and Voronoi cell finite element method, *International Journal of Solids and Structures* **32(1)**:27-62.

Ghosh S, Lee K, Moorthy S, 1996, Two scale analysis of heterogeneous elastic-plastic materials with asymptotic homogenization and Voronoi cell finite element model, *Computer Methods in Applied Mechanics and Engineering* **132(1-2)**:63-116.

Godfrey NJ, Christensen NI, Okaya DA, 2000, Anisotropy of schists: Contribution of crustal anisotropy to active source seismic experiments and shear wave splitting observations, *Journal of Geophysical Research* **105**:27991-28007.

González C, Segurado J, LLorca J, 2004, Numerical simulation of elasto-plastic deformation of composites: evolution of stress microfields and implications for homogenization models, *Journal of the Mechanics and Physics of Solids* **52**:1573-1593.

Goupee AJ, Vel SS, 2006, Two-dimensional optimization of material composition of functionally graded materials using meshless analyses and a genetic algorithm, *Computer Methods in Applied Mechanics and Engineering* **195(44-47)**:5926-5948.

Goupee AJ, Vel SS, 2007, Multi-objective optimization of functionally graded materials with temperature-dependent material properties, *Materials & Design* **28(6)**:1861-1879.

Grujicic M, Zhang Y, 1998, Determination of effective elastic properties of functionally graded materials using Voronoi cell finite element method, *Materials Science and Engineering* **A251**:64-76.

Guedes JM, Kikuchi N, 1990, Preprocessing and postprocessing for materials based on the homogenization method with adaptive finite elements, *Computer Methods in Applied Mechanics and Engineering* **83**:143-198.

Gusev AA, Hine PJ, Ward IM, 2000, Fiber packing and elastic properties of a transversely random unidirectional glass/epoxy composite, *Composites Science and Technology* **60**:535-541.

Hashin Z, 1965, On elastic behavior of fiber-reinforced materials of arbitrary transverse phase geometry, *Journal of the Mechanics and Physics of Solids* **13**:119-134.

Hashin Z, 1979, Analysis of properties of fiber composites with anisotropic constituents, *Journal of Applied Mechanics-Transactions of the ASME* **46(3)**:543-550.

Hashin Z, Rosen BW, 1964, The elastic moduli of fiber-reinforced materials, *Journal of Applied Mechanics* **31**:223-232.

Hill R, 1952, The elastic behaviour of a crystalline aggregate, *Proceedings of the Physical Society of London, Section A* **65(389)**:349-355.

Hill R, 1964, Theory of mechanical properties of fiber-strengthened materials. I. Elastic behavior, *Journal of the Mechanics and Physics of Solids* **12**:199-212.

Hill R, 1965, A self-consistent mechanics of composite materials, *Journal of the Mechanics and Physics of Solids* **13**:213-222.

Horn RA, Johnson CR, 1999, *Topics in Matrix Analysis*, Cambridge University Press, Cambridge.

Ji, S, 2004, Generalized means as an approach for predicting Young's moduli of multiphase materials, *Materials Science and Engineering* **A366**:195-201.

Jin G, Takeuchi M, Honda S, Nishikawa T, Awaji H, 2005, Properties of multilayered mullite/Mo functionally graded materials fabricated by powder metallurgy processing, *Materials Chemistry and Physics* **89**:238-243.

Kamiński M, Figiel Ł, 2001, Effective elastoplastic properties of the periodic composites, *Computational Materials Science* **22**:221-239.

Kawasaki A, Watanabe R, 1997, Concept and P/M fabrication of functionally gradient materials, *Ceramics International* **23**:73-83.

Lai WM, Rubin D, Krempl E, 1999, *Introduction to Continuum Mechanics*, 3rd Edition, Butterworth-Heinemann, Burlington.

Langer SA, Fuller E, Carter WC, 2001, OOF: An image-based finite-element analysis of material microstructures, *Computing in Science and Engineering* **3(3)**:15-23.

Lee SB, Torquato S, 1989, Measure of clustering in continuum percolation: Computer-simulation of the two-point cluster function, *Journal of Chemical Physics* **91**:1173-1178.

Leggoe JW, Mammoli AA, Bush MB, Hu XZ, 1998, Finite element modelling of deformation in particulate reinforced metal matrix composites with random local microstructure variation, *Acta Materialia* **46(17)**:6075-6088.

Leßle Q, Dong M, Schmauder S, 1999, Self-consistent matricity model to simulate the mechanical behaviour of interpenetrating microstructures, *Computational Materials Science* **15(4)**:455-465.

Lipton R, 2002, Design of functionally graded composite structures in the presence of stress constraints, *International Journal of Solids and Structures* **39**:2575-2586.

Loy CT, Lam KY, Reddy JN, 1999, Vibration of functionally graded cylindrical shells, *International Journal of Mechanical Sciences* **41**:309-324.

Mainprice D, Humbert M, 1994, Methods of calculating petrophysical properties from lattice preferred orientation data, *Surveys in Geophysics* **15(5)**:575-592.

Matthies S, Humbert M, 1993, The realization of the concept of a geometric mean for calculating physical constants of polycrystalline materials, *Physica Status Solidi B-Basic Research* **177**:K47-K50.

Mainprice D, 1990, A fortran program to calculate seismic anisotropy from the lattice preferred orientation of minerals, *Computers and Geosciences* **16**:385-393.

Mainprice D, Nicolas A, 1989, Development of shape and lattice preferred orientations: application to the seismic anisotropy of the lower crust, *Journal of Structural Geology* **11**:175-189.

Misnaevsky Jr. LL, 2005, Automatic voxel-based generation of 3D microstructural FE models and its application to the damage analysis of composites, *Materials Science and Engineering* **A407**:11-23.

Miyamoto Y, Kaysser WA, Rabin BH, Kawasaki A, Ford RG, 1999, *Functionally Graded Materials: Design, Processing and Applications*, Kluwer Academic Publishers, Boston.

Mooney WD, 2007, Crust and lithospheric structure - global crustal structure, In: Schubert G, Romanowicz B, Dziewonski A (Eds.), *Treatise on Geophysics, Volume 1, Seismology and structure of the Earth*, Elsevier, 361-417.

Mori T, Tanaka T, 1973, Average stresses in matrix and average elastic energy of materials with misfitting inclusions, *Acta Metallurgica* **21**:571-574.

Nowacki W, 1975, *Dynamics Problems of Thermoelasticity*, Kluwer Academic Publishers, Boston.

Nowinski JL, 1978, *Theory of Thermoelasticity with Applications*, Sijthoff & Noordhoff International Publishers, Alphen aan den Rijn.

Okaya DA, Christensen NI, 2002, Anisotropic effects of non-axial seismic wave propagation in foliated crustal rocks, *Geophysical Research Letters* **29(11)**:1507.

Okaya DA, Christensen NI, Stanley D, Stern T, 1995, Crustal anisotropy in the vicinity of the Alpine Fault Zone, South Island. *New Zealand Journal of Geology and Geophysics* **38**:579-583.

Okaya, DA, McEvilly, T, 2003, Elastic wave propagation in anisotropic crustal material possessing arbitrary internal tilt, *Geophysical Journal International* **153**:344-358.

Ostoja-Starzewski M, 1998, Random field models of heterogeneous materials, *International Journal of Solids and Structures* **35(19)**:2429-2455.

Pelletier JL, Vel SS, 2006, An exact solution for the steady-state thermoelastic response of functionally graded orthotropic cylindrical shells, *International Journal of Solids and Structures* **43(5)**:1131-1158.

Prager S, 1961, Viscous flow through porous media, *Physics of Fluids* **4**:1477-1482.

Qian LF, Ching HK, 2004, Static and dynamic analysis of 2-D functionally graded elasticity by using meshless local petrov-galerkin method, *Journal of the Chinese Institute of Engineers* **27**:491-503.

Reddy JN, 1993, *An Introduction to the Finite Element Method*, 2nd Edition, McGraw Hill, Boston.

Reuss A, 1929, Account of the liquid limit of mixed crystals on the basis of the plasticity condition for single crystal, *Zeitschrift fur Angewandte Mathematik und Mechanik* **9**:49-58.

Roberts AP, Knackstedt MA, 1996, Structure-property correlations in model composite materials, *Physical Review E* **54(3)**:2313-2328.

Roberts AP, Teubner M, 1995, Transport properties of heterogeneous materials derived from Gaussian random fields: Bounds and simulation, *Physical Review E* **51(5)**:4141-4154.

Rosen BW, Hashin Z, 1970, Effective thermal expansion coefficients and specific heats of composite materials, *International Journal of Engineering Science* **8(2)**:157-174.

Sanchez-Palencia E, 1981, Nonhomogeneous media and vibration theory, *The Journal of the Acoustical Society of America* **69(3)**:884.

Sanchez-Palencia E, 1983, Homogenization method for the study of composite media, *Asymptotic Analysis II* **985**:192-214.

Savage, M, 1999, Seismic anisotropy and mantle deformation: what have we learned from shear wave splitting?, *Reviews of Geophysics* **37**:65-106.

Segurado J, Llorca J, 2002, A numerical approximation to the elastic properties of sphere-reinforced composites, *Journal of the Mechanics and Physics of Solids* **50**:2107-2121.

Silva ECN, Walters MC, Paulino GH, 2006, Modeling bamboo as a functionally graded material: lessons for the analysis of affordable materials, *Journal of Materials Science* **41**:6991-7004.

Simmons G, 1964, Velocity of shear waves in rocks to 10 kilobars, 1, *Journal of Geophysical Research* **69**:1123-1130.

Smith PA, Torquato S, 1988, Computer simulation results for the two-point probability function of composite media, *Journal of Computational Physics* **76**:176-191.

Soppa E, Schmauder S, Fischer G, Brollo J, Weber U, 2003, Deformation and damage in Al/Al2O3, *Computational Materials Science* **28(3-4)**:574-586.

Takagi K, Li J-F, Yokoyama S, Watanabe R, 2003, Fabrication and evaluation of PZT/Pt piezoelectric composites and functionally graded actuators, *Journal of the European Ceramic Society* **23**:1577-1583.

Takano N, Zako M, Ishizono M, 2000, Multi-scale computational method for elastic bodies with global and local heterogeneity, *Journal of Computer-Aided Materials Design* **7**:111-132.

Taliercio A, 2005, Generalized plane strain finite element model for the analysis of elastoplastic composites, *International Journal of Solids and Structures* **42**:2361-2379.

Tamura I, Tomota Y, Ozawa M, 1973, Strength and ductility of Fe-Ni-C alloys composed of austenite and martensite with various strengths, *Proceedings of the 3rd International Conference on Strength of Metals and Alloys* **1**:611-615.

Terada K, Hori M, Kyoya T, Kikuchi N, 2000, Simulation of the multi-scale convergence in computational homogenization approaches, *International Journal of Solids and Structures* **37**:2285-2311.

Terada K, Kikuchi N, 1995, Nonlinear homogenization method for practical applications, In: *Computational Methods in Micromechanics* (Proceedings of 1995 ASME

International Mechanical Engineering Congress and Exposition), Ghosh S, Ostoja-Starzewski M (Eds.) AMD-212/MD-22, ASME Press, 1-16.

Terada K, Kikuchi N, 2001, A class of general algorithms for multi-scale analyses of heterogeneous media, *Computer Methods in Applied Mechanics and Engineering* **190**:5427-5464.

Torquato S, 2002, *Random Heterogeneous Materials: Microstructure and Macroscopic Properties*, Springer-Verlag, New York.

Torquato S, Stell G, 1982, Microstructure of two-phase random media. I. The n-point probability functions, *Journal of Chemical Physics* **77**:2071-2077.

Torquato S, Stell G, 1983, Microstructure of two-phase random media. III. The n-point probability functions for fully penetrable spheres, *Journal of Chemical Physics* **79(3)**:1505-1510.

Ueda S, Gasik M, 2000, Thermal-elasto-plastic analysis of W-Cu functionally graded materials subjected to a uniform heat flow by micromechanical model, *Journal of Thermal Stresses* **23**:395-409.

van der Sluis O, Schreurs PJG, Brekelmans WAM, Meijer HEH, 2000, Overall behavior of heterogeneous elastoviscoplastic materials: effect of microstructural modelling, *Mechanics of Materials* **32**:449-462.

Vel SS, Batra RC, 2002, Exact solution for the thermoelastic deformations of functionally graded thick rectangular plates, *AIAA Journal* **40(7)**:1421-1433.

Vel SS, Batra RC, 2003, Three-dimensional analysis of transient thermal stresses in functionally graded plates, *International Journal of Solids and Structures* **40**:7181-7196.

Vel SS, Pelletier JL, 2007, Multi-objective optimization of functionally graded thick shells for thermal loading, *Composite Structures* **81(3)**:386-400.

Voigt W, 1889, Über die beziehung zwischen den beiden elasticitäts-constanten isotroper körper, *Annalen der Physik and Chemie* **38**:573-587.

Voigt W, 1928, *Lehrbuch Kristallphy.*

Wegner LD, Gibson LJ, 2000, The mechanical behaviour of interpenetrating phase composites - I: modelling, *International Journal of Mechanical Sciences* **42(5)**:925-942.

Wegner LD, Gibson LJ, 2001, The mechanical behaviour of interpenetrating phase composites - III: resin-impregnated porous stainless steel, *International Journal of Mechanical Sciences* **43(4)**:1061-1072.

Yin HM, Sun LZ, Paulino GH, 2005, A multiscale framework for elastic deformation of functionally graded composites, *Functionally Graded Materials VIII, Materials Science Forum* **492-493**:391-396.

BIOGRAPHY

Andrew J. Goupee was born in Bangor, Maine on January 29, 1981. He was raised in Orrington, Maine and graduated from Brewer High School in June of 1999. He then attended The University of Maine beginning in the fall of 1999. He graduated as Valedictorian of his graduating class of 2003, and received a Bachelor of Science degree in Mechanical Engineering. He entered the Mechanical Engineering graduate program at the University of Maine in the summer of 2003 and subsequently earned his Master of Science degree in Mechanical Engineering in 2005. At the completion of his Master of Science degree, Andrew entered the doctoral program in the Department of Mechanical Engineering at the University of Maine. Andrew is a candidate for the Doctor of Philosophy degree in Mechanical Engineering from The University of Maine in May, 2010.